Gauging the Universe: the Effect of the Metallicity on the Cepheid Period-Luminosity Relation

Dissertation der Fakultät für Physik
der
Ludwig-Maximilians-Universität München

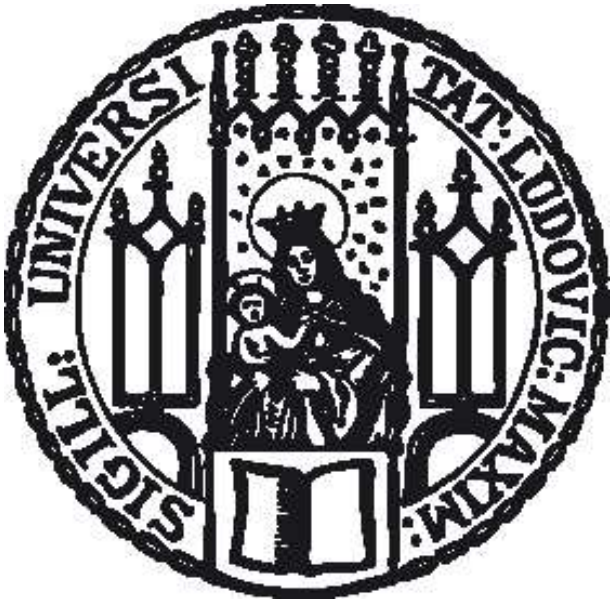

vorgelegt von Marta Mottini
aus Magenta, Italien
München, den 19-06-2006

Datum der mündlichen Prüfung: 19. Juni 2006

1. Gutachter: Priv. Doz. Dr. Achim Weiss
2. Gutachter: Prof. Dr. Adalbert W.A. Pauldrach

Summary

The aim of this thesis is to assess the effect of the metallicity on the Cepheid Period-Luminosity (PL) relation. The novelty of the approach adopted in this project consists in the homogeneous analysis of a large sample of Cepheids (72) observed in three galaxies (the Milky Way, the Large Magellanic Cloud and the Small Magellanic Cloud), spanning a factor of ten in metallicity. This allows us to explore the effect of the metallicity on the PL relation in a wide range and to study the gas enrichment histories of three different galaxies. To fulfil this goal, firstly, we have selected a sample of Cepheids for which distances and accurate photometry are available in the literature and we have collected high-resolution, high signal-to-noise spectra of these stars, using the highly advanced facilities of the European Southern Observatory in Chile. Secondly, we have directly measured iron and α-elements (O, Na, Mg, Al, Si, Ca, Ti) abundances of our sample from these spectra. We have compared our iron abundances with studies on Galactic and Magellanic Cepheids and found a good agreement for the average values and for the individual stars in common. We have then made a broader comparison with results for the Magellanic Clouds from the analysis of F and K non-variable supergiants (they have ages and temperatures similar to Cepheid stars) and of B stars, which are progenitors of Cepheids, and found a good agreement. Cepheids do not show any peculiar differences with these two other population of stars, this indicate that, during this evolutionary stage, there are no changes of the original iron content of the gas from which they were formed. We have then studied the trends of the individual α elements abundance ratios relative to iron as a function of the iron content of our programme star. We can draw some preliminary conclusion considering oxygen, silicon and calcium as the most reliable indicators among the α elements we have analysed. The trends of the abundance ratios of O, Si and Ca are in fairly good agreement with observational studies on Cepheids and on different kinds of stellar populations in the Galaxy and the Magellanic Clouds. The elemental abundances we have determined were used to investigate the effect of metallicity on the PL relation in the V and K bands, in order to check if there is a change of the effect as wavelength increases. We note different behaviours in the two bands. The metallicity has an effect in the V band in the sense that metal-rich Cepheids are fainter than metal-poor ones, while it does not have any effects in the K band. Thus, to safely measure the distances of galaxies, one can use the PL relation in the infrared bands (namely K), so as to minimise the effect of the metallicity. Using the K band has the additional advantage of reducing the effects of the interstellar extinction to the level of other systematic and random errors.

Contents

Contents

Chapter 1

Introduction

Cepheids variables have played an important role in astronomy since it was recognised that they could be used to determine distances through their Period-Luminosity relation. Most derived characteristics of a star or any other astrophysical object, such as mass, age, energy output and size, depend significantly on how well one is able to determine its distance. Therefore measuring distances is a capital element at the core of astrophysical research.

For over eighty years Cepheids have served as an effective tool for studying the universe. Cepheids provide one of the best means of determining the distances to nearby galaxies and they are used to calibrate secondary distance indicators, thus they play a crucial role to establish the extragalactic distance scale, being the first rung of the distance ladder. Furthermore the measurement of the Hubble constant (H_0), which sets the scale of the Universe in space and time, depends heavily on accurate extragalactic distance measurements.

Cepheids are also useful objects for investigating the structure of our Galaxy, the plausibility of physical assumptions adopted to compute evolutionary models of the late evolutionary stages of massive stars and the gas enrichment history that led to the formation of young stellar population.

1.1 Cepheids: a brief history

The first two Cepheids were discovered by two pioneers in the systematic observation of variable stars, E. Pigott and J. Goodricke, in 1784. These were η Aquilae and δ Cephei, the latter supplied the name now used for this class of stars.

In 1894 A.A. Belopol'skii detected periodic variations in the radial velocities[a] of Cepheids and, in 1899, K. Schwarzschild found the amplitude of a Cepheid's luminosity variation to be considerably higher in photographic light than in visual light. This pointed to a variability of the temperature, as well as of the luminosity. These facts found their natural explanation in the hypothesis of Cepheid pulsations, first proposed by Ritter in 1879 and later by Umov, Plummer and Shapley (see H.

[a]The radial velocity of a star is the velocity in the direction of the line of sight. This can be measured from a star's spectrum using the Doppler effect.

Shapley 1914).

The case for the pulsation hypothesis grew to be accepted due to new measurements which confirmed that the surface temperature of Cepheids changed over the pulsational cycle. In addition, theoretical work of Sir Arthur Eddington put this hypothesis on a firmer basis (A. Eddington 1927, 1941, 1942). He showed that Cepheids are single stars that undergo radial pulsations, because they can be shown to have characteristics which can be described like those of a heat engine. Later work by S. A. Zhevakin (1963), R. F. Christy (1966), J. P. Cox (1980) and others provided a deeper understanding of the mechanism behind Cepheid pulsations. The driving mechanism, known as k-mechanism, behind "self-excited" oscillations is a special region of the stellar interior where atoms of either hydrogen or helium make a transition from partly to completely ionized. If the star is compressed, the ionisation fraction of these regions increases, raising the opacity of the material and blocking the luminous energy trying to escape from the interior. The increased heat and pressure built up in this layer push the outer layers of the star outward. As these outer layers fall back inward again under the force of gravity, the ionization region gets compressed again, restarting the cycle. The variation in brightness is caused by changes in temperature and radius caused by these motions. Cepheid pulsations are therefore restricted to stars in a limited temperature range, due to the requirement that the partial ionisation zone lies close to the transition from the nearly adiabatic interior to the non-adiabatic exterior of the stellar envelope.

Henrietta Leavitt revealed the first indication of a period-luminosity relation in variable stars. Following the examination of hundreds of photographic plates obtained between 1893 and 1906 at the Harvard College's observatory in Peru, she produced a catalogue of 1777 variable stars in the Magellanic Clouds[a]. Among these stars, 16 appeared in a sufficient number of plates for their periods to be determined. When tabulated in order of increasing luminosity a pattern emerged. In 1912 Leavitt produced more data on the period-luminosity (PL) relation (Leavitt 1912). She had managed to obtain the magnitudes[b] and periods for 25 variables in the Small Magellanic Cloud (SMC). In her paper, she had also described the characteristics of the light-curves of her variables, and noted their similarities to variables in the globular clusters[c]. Their similarities with the well-documented Galactic variable δ Cephei were particularly strong.

In 1913 Danish astronomer Ejnar Hertzsprung realised that if the PL relation could be calibrated, then the absolute magnitudes of members of this group of variable stars might be determined directly from their periods. It should then be a straightforward matter to obtain their distance moduli[d] and hence their distances and the distance of the stellar system they belong to. This was, and remains, the prime motivation behind the Cepheid Period-Luminosity calibration.

Shapley's calibration (1918) followed Hertzsprung's early attempt and was widely regarded as a significant improvement upon it. However, it was eventually realised that, due mainly to

[a] Two small irregular galaxies, satellites of the Milky Way.

[b] The logarithmic measure of the brightness of an object, measured in a specific wavelength or passband.

[c] Globular clusters are gravitationally bound concentrations of approximately hundred thousand to more than one million of old stars (Population II).

[d] The distance modulus $\mu = m - M$ is the difference between the apparent magnitude m and the absolute magnitude M of an astronomical object, or the flux ratio.

systematic errors and a failure to take into account extinction[a], his zero point was approximately 1.5 magnitudes too dim. Nevertheless, an extraordinary coincidence led to this not being realised for over 30 years.

Shapley's particular interest at that time laid in globular clusters, to study the structure of our Galaxy and the position of the Sun in it. Leavitt herself had remarked upon the similarity of the bright globular cluster variables to those in the SMC. Shapley examined the PL curve for the "longer - period" variables in the globular clusters and found that its slope was very similar to that for the SMC, accordingly he incorporated these stars in his PL relation as "Cepheids". In his 1918 paper, variables from no fewer than 7 stellar systems were combined into the single relation shown in Fig. Figure 1.1.

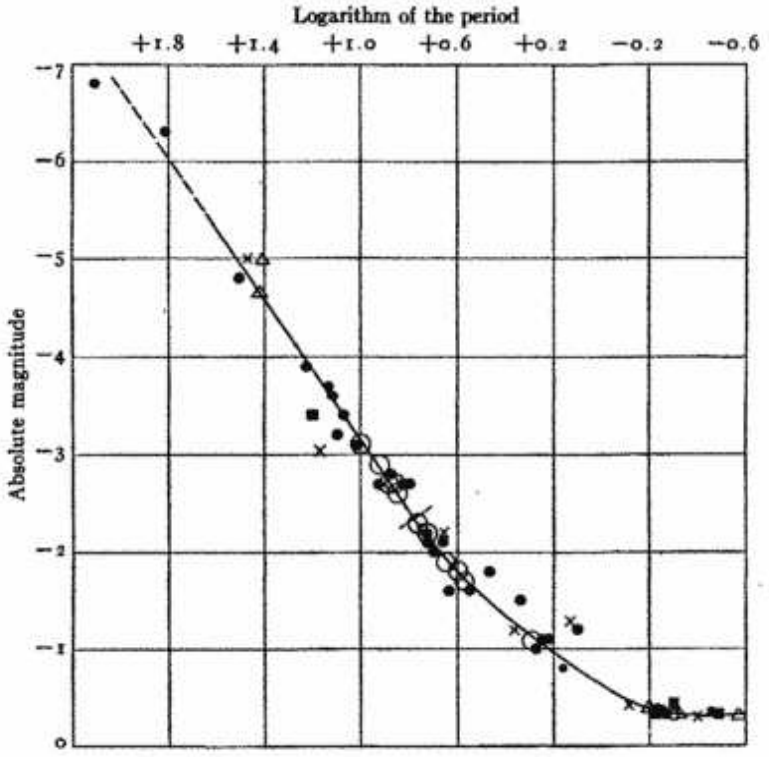

Figure 1.1: *The Period-Luminosity relation found by Shapley (1918). Figure from his original article.*

Inspection of Fig. 1.1 illustrates that Shapley had gone even further than this: the linear relationship breaks down at bottom right due to his inclusion of faint, short period variables. He called these stars "cluster-type Cepheids"; now known as RR Lyrae variables, which are central He-burning low-mass stars but characterised by the same pulsating mechanism.

[a]Absorption of light from astronomical objects by matter between them and the observer.

We now know that the variables identified by the early calibrators actually consisted of stellar populations with different characteristics, but this did not come to light until Baade's observations in the 1940s and 50s.

In the 1920's the discovery of Cepheids in the Andromeda galaxy and in other nebulae enabled E. Hubble to apply the PL relation to determine the distances of these objects and to establish once and for all their extragalactic nature.

The works of Shapley and Hubble changed completely the current conception of the universe: the Sun was not in the centre of a unique gigantic stellar system, the Milky Way, but rather at the edge of one of the countless number of such systems.

In the next three decades several studies of the Cepheid PL relation had been carried out, in particular revisions of Shapley's zero point for this relation. As we have already mentioned, Baade's works (from 1944 to 1952) revealed the existence of two kind of Cepheids with distinct PL relations, the first, known as Classical Cepheids, associated with the disc component of our Galaxy (young stellar population) and the second with the spherical component (old stellar population). These results and the studies of Cepheids in open stellar clusters[a] (e.g. Sandage, 1958; Kraft 1961) led to the correction of the zero point of the PL relation of a value of -1.5 magnitudes and to new estimates of galactic and extragalactic distances (nearly doubled respect to the previous estimates).

With the advent of new technologies, in particular highly sensitive, multi-wavelength observations, and increased use of infrared (IR) wavelengths, the approach of modern studies to the Cepheid calibration shifted towards the empirical rather than the speculative. Multi-wavelength observation of Cepheid magnitudes, better estimates of reddening effects (i.e. extinction, Freedman 1988), of individual distances of Galactic Cepheids (Feast & Catchpole 1997) and of the Magellanic Clouds distances (see Benedict 2002 for a review on methods and results) greatly improved the determination of the zero point and the slope of the PL relation. In particular the calibration of the PL relation in the LMC is essential because this galaxy is the first rung of the extragalactic ladder, since it is the closest external system to our Galaxy, it has a low extinction and little depth on the line of sight (all its Cepheids are, roughly, at the same distance).

With the launch of the Hubble Space Telescope (HST) into orbit in 1990, it has also been possible to extend the Cepheid distance scale out to the Virgo and Fornax galaxies clusters (HST key project, Freedman et al 2001). The result of this work has seen Cepheids play a significant role in the distance determination of galaxies and the resulting cosmological implications.

1.2 Cepheids: characteristics

As already mentioned in the previous section, Cepheids are variable stars and they can be divided in two categories: Type I or Classical Cepheids and Type II Cepheids. The first type of variables are young stars (Population I stars) and we will discuss their characteristics in more details afterwards. Type II Cepheids (W Virginis) instead are old stars (Population II), intrinsically less luminous, at a given period, and less massive than the Classical Cepheids. Both types of Cepheids exhibit

[a]Open clusters are physically related groups of young stars (Population I) held together by mutual gravitational attraction.

distinct period-luminosity relations. Since the goal of this thesis project is the study of a sample of Classical Cepheids we will not discuss Type II Cepheids. For this reason the adjective "classical" will be omitted in the following.

Cepheids are supergiant stars with luminosities 500-30,000 times greater than that of the Sun ($L_\odot = 3.9 \cdot 10^{33}$ erg s^{-1}) and their surface temperatures are similar to the Sun's temperature (∼6000 K). The ages of Cepheids are between few million years up to 600 million years and their masses are between 3 and 15 solar masses ($M_\odot = 1.99 \cdot 10^{33}$ g). They undergo regular radial pulsation (i.e. the star expands and contracts) with periods ranging from about 1 to about 200 days. The periods of Cepheids in our Galaxy range from 1 to 90 days, and in the Magellanic Clouds they have been observed to have periods ranging up to 200 days. More than 400 Cepheids are known in the Milky Way, 1300 and 2000, respectively, have been found in the Large and Small Magellanic Cloud (thanks to the large survey of the Optical Gravitational Lensing Experiment), as well as substantial numbers in other nearby galaxies.

Cepheids are easily recognised by their distinctive light curves[a], which are characterised by a rapid rise to maximum brightness, followed by a slow decline to their minimum (see Fig 1.2).

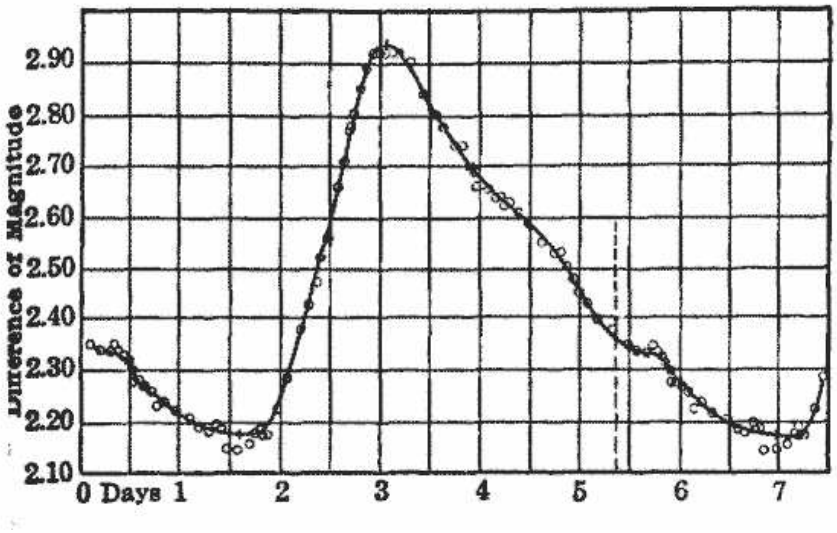

Figure 1.2: *The light curve for δ Cephei, the prototype of this class of stars (from Hoskin 1999)*

This pattern of changing brightness is repeated in a very regular cycle. The light curve of a Cepheid is matched by its radial velocity curve, which is almost a mirror image of the light curve with minimum radial velocity at the light maximum. The positive (redshifted) half of the velocity curve corresponds to the contraction of the star from its maximum to minimum radius, which is the later part of the decline of the light curve to minimum brightness and the beginning of the ascent to maximum brightness. The negative (blueshifted) half of the velocity curve corresponds to the

[a]The variation of the luminosity of the star as a function of time.

expansion of the star and the brightest part of the light curve. During the same period the surface temperature reaches its highest effective temperature and gradually cools as the star completes its expansion. The light amplitude is typically between 0.5 and 2 magnitudes in blue light and the velocity amplitude usually lies in the range 30-60 km s^{-1}

Because of their characteristic light curve and intrinsic brightness, these stars can be distinguished at great distances and make excellent markers for determining distances through their period-luminosity relationship.

The first study of Cepheid light curves which gave useful results were those of E. Hertzsprung (1926). He selected 37 of the most reliable curves and described the main features of their variations with an increase in period. The principal result of this and other studies of the time can be summarised as follows:

- up to a period of 6 days the light curves are usually smooth, with a rapid rise in luminosity and a more gradual drop;
- at about 6 days a hump appears on the descending branch of the light curve, and then the hump grows and approaches the principle maximum (see Fig 1.2);
- close to a period of 9 or 10 days the hump is so large that the curve sometimes has two nearly identical peaks;
- with a further increase in the period, the secondary oscillation which originated at a period of 6 days becomes the maximum and the formal principle oscillation becomes a hump on the ascending branch.

The changes in the shape of the light curve with the period is now known as the Hertzsprung progression.

Applying Fourier analysis to the light curves the existence of Cepheids that do not pulsate in the fundamental mode (as, in general, a Cepheid does) has been discovered. Cepheids can pulsate in the first overtone mode (Pel & Lub, 1978; Böhm-Vitense, 1994), the second overtone mode (Udalsky et al 1999b; Bono et al, 2001)and also in two modes simultaneously (Fitch, 1970, King et al, 1975; Pardo & Poretti, 1997). Theoretical predictions and observations suggest that first overtone periods range from logP$\sim$0.6 to 0.9 for the Milky Way, from logP$\sim$0.7 to 0.8 for the LMC and from logP$\sim$0.6 to 0.8 for the SMC (Bono et al, 2002). The double-mode Cepheids usually pulsate in the fundamental and first overtone modes and the longer of the two periods is between 2 and 4 days.

Photometric observations of Cepheids have shown a number of other interesting characteristics. The amplitude of variation is observed to decrease with increasing wavelength (see Fig. 1.3). B and V band photometric variations are due primarily to changes in the surface temperature, while in the infrared, the observed luminosity changes are primarily due to the variation in the radius of the star. From B band to K band a typical Cepheid amplitude drops from 1.0 mag to 0.2 mag. Because the variation of the amplitude in the infrared is relatively small, a single observation in the infrared can be enough to estimate the average luminosity and give a useful distance determination as opposed

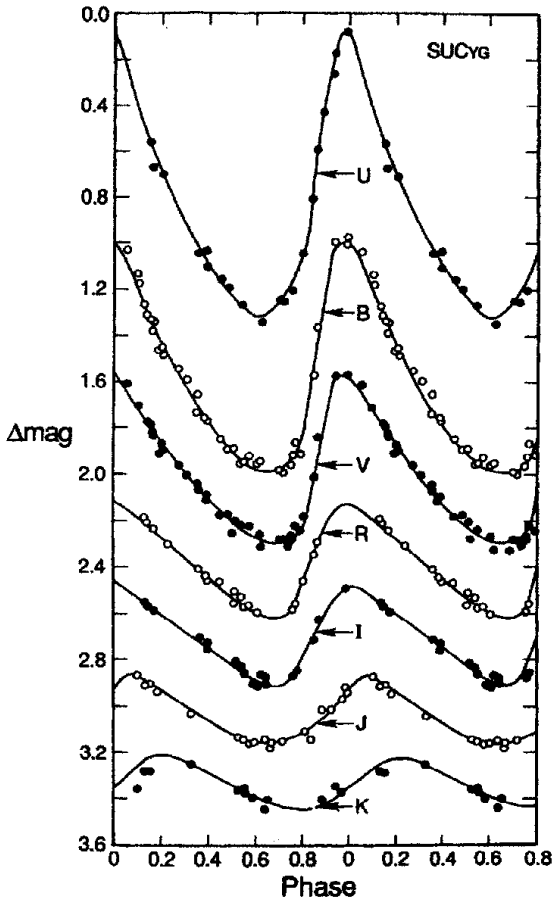

Figure 1.3: *Light curves in different colours for a Galactic Cepheid, showing the change in amplitude and phase with the waveband selected (from Madore & Freedman 1991)*

to the several dozen observations that would be required at bluer wavelengths to determine an average luminosity (see Fig. 1.3).

Another important characteristic of Cepheids has emerged from radial velocity measurements: the incidence of binaries (mainly spectroscopic[a]) among these variables exceeds 50% (Szabados 1995). The orbital periods of these binary systems are generally long (1-5 yr) and a typical companion is a much hotter B or A star (with temperature between 20,000 K and 10,000 K). The light of the Cepheid is dominant at visible wavelengths while the main contribution of the companion is in the ultraviolet band (Evans 1991).

[a]Two stars that are gravitationally bound to each other and that cannot be visually resolved. Their components are distinguished spectroscopically.

1.3 Cepheids: evolution

Cepheids arise as a result of post-main sequence evolution of population I stars of intermediate to high stellar masses. Intermediate mass stars are those which ignite He combustion under non-degenerate conditions, but following core He exhaustion they develop electron degenerate carbon-oxygen cores. To become a Cepheid, the star must be in a post core hydrogen-burning phase so as to pass through the instability strip[a] on the Hertzsprung-Russell (HR) diagram[b] (see Fig. 1.4). Iben & Tuggle (1975), using non-adiabatic models, have been able to predict the position of the blue edges (fundamental and first overtone) of the instability strip. However they have not been able to predict the red edges, which are ruled by the efficiency of convection. More recent models which include this mechanism (e.g. Chiosi et al 1993) do predict the red edges. These boundaries extend to include both the realms of the massive and low-mass stars (see Fig. 1.5).

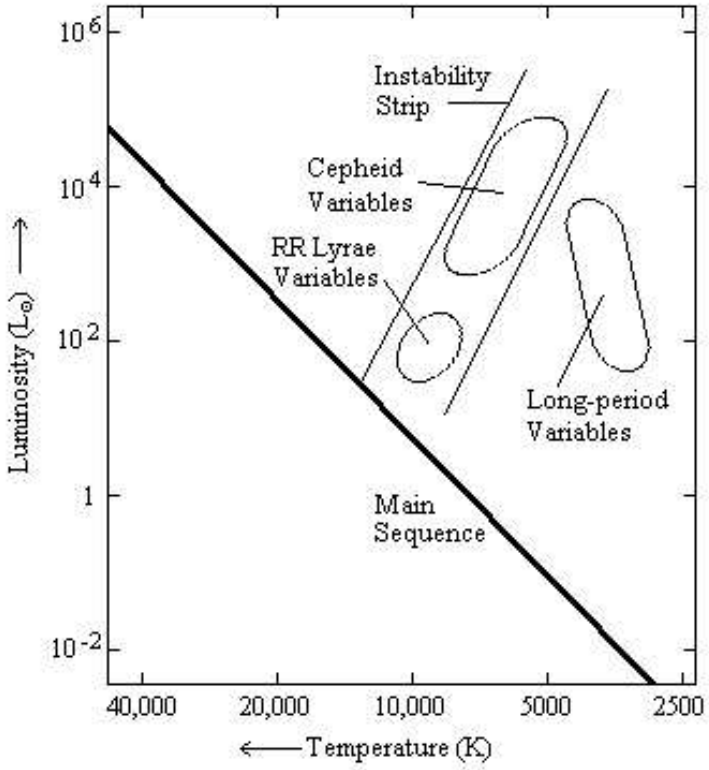

Figure 1.4: *Schematic representation of the instability strip in the HR diagram.*

[a]The Cepheid instability strip defines a range of luminosities and effective temperatures over which pulsation is a stable mode for a star and is therefore an observable

[b]The Hertzsprung-Russell diagram is a plot of luminosity vs temperature, except that the temperature is decreasing to the right of the horizontal axis. It is used to classify star according to their luminosity, spectral type, colour, temperature and evolutionary stage.

1 Introduction

An evolving star may cross the Cepheid instability strip on the HR diagram more than once during its lifetime. The first crossing of the instability strip for all but the most massive stars, occurs during the hydrogen-shell burning phase as the star evolves to cooler temperatures in the HR diagram on its way to become a red giant[a]. This first passage, during envelope expansion, is rapid, and occurs on a Kelvin-Helmholtz timescale[b], ranging from a few times 10^3 yr to about 10^4 yr, with the lifetime of this crossing increasing with increasing mass.

The second crossing of the instability strip occurs once core helium burning has occurred. During this helium-burning phase, the star evolves to higher temperatures and the star may loop through the instability strip again producing two more crossings. The occurrence of a blue loop can result in the second and third crossings of the instability strip, which is due to the complicated interplay between the hydrogen abundance profile left by the former hydrogen burning core, the hydrogen burning shell, the maximum depth reached by the convective envelope during the star's first ascent of the red giant branch, and the nature of the stellar envelope model solutions used (see Schlesinger 1977 for review). The lifetime of these subsequent crossings can last several million years, as is the case when the tip of a blue loop is tangential to the blue edge of the instability strip and is driven on a nuclear time scale. The lifetimes of these loops decrease to thermal timescales as the mass of the stars increase.

The second crossing of the instability strip is almost always the longest lived[c] and indeed appears to be supported by the apparent evolutionary state of most Cepheids. The occurrence of the first blue loop also provides an effective lower mass limit to the distribution of Cepheids, since stars of lower mass will fail to produce blue loops which will intercept the instability strip. These stars will only be observed to be Cepheids on their first and only passage through the instability strip and due to the short lifetime of the crossing, will probably only make up at most 10% of the observed Cepheid population.

The third crossing of the instability strip can occur under two different conditions. The most common condition occurs on the first blue loop near the end of the core helium-burning phase as the star once again evolves back to the red giant branch. The lifetime of this crossing is shorter than the second crossing, but can last as long as 10^6 yr in the most extreme case. The other cause for a third crossing of the instability strip is once core helium-burning has ceased and has been replaced by shell helium-burning as the primary energy source for the star. In this case, there will be one final crossing as the star traverses rapidly through the instability strip over to the red giant branch on a thermal timescale on the order of 10^3 yr. If conditions allow, a rare second blue loop can occur which produces two additional crossings of the instability strip. Hoppner et al (1978) and Becker (1981) show that this additional loop was due to the complicated interaction between the contracting helium exhausted core, the helium-burning shell, and the nature of the stellar envelope solutions. The lifetimes of these fourth and fifth crossings were roughly the same

[a]Stars of solar mass or higher which have exhausted the hydrogen in their cores and started burning hydrogen in a shell outside the core. Since the source of energy is closer to the surface, the star begins to expand. As a result, the star becomes larger in size and cooler (i.e. redder)

[b]The time that an object takes to radiate away its stored energy.

[c]It is only in the case of the more massive blue-looping models where all crossings are driven on a thermal timescale that this rule is no longer valid (Becker 1985).

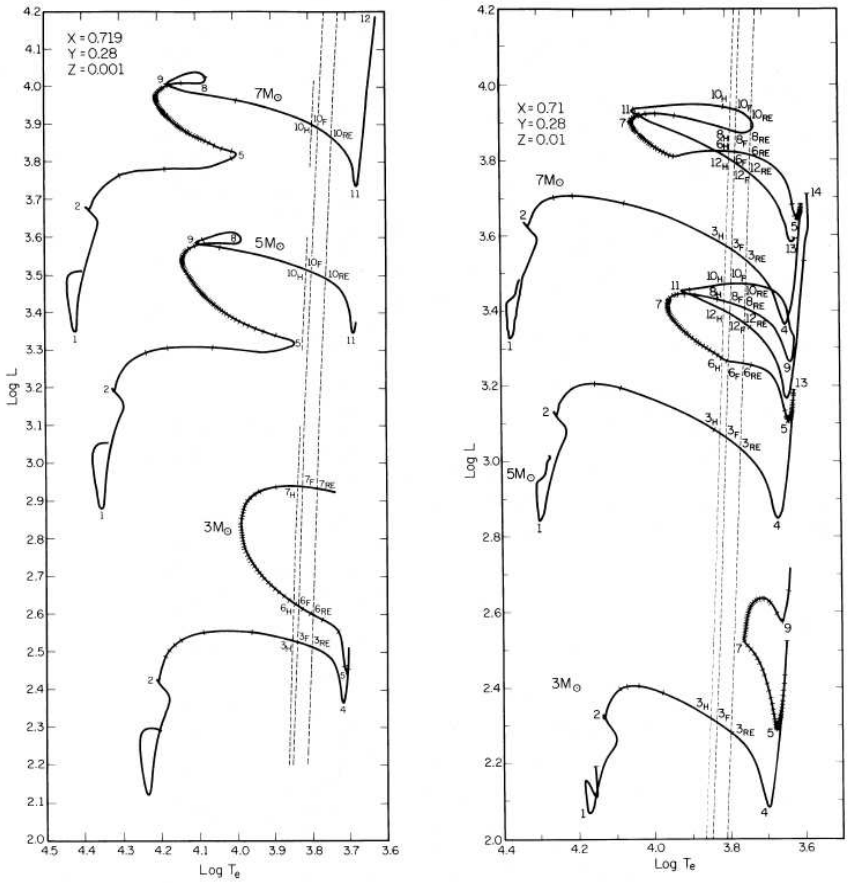

Figure 1.5: *Evolutionary tracks for Cepheids taken from Becker 1977. Note the almost vertical dashed lines representing, on the right, the red edge of the instability strip, and on the left, the blue edges for fundamental and first overtone pulsation. As can be seen above the metallicity of a star influences the subsequent evolution and the occurrence of the critical blue loops which must pass through the instability strip in order for a Cepheid to be observed. The increase in the metallicity causes the loops to occur further to the red side of the HR diagram.*

and could potentially be as long as a few times 10^5 yr. The crossing times decreased rapidly with increasing mass, until for the most massive models, the second blue loop takes place to the left of the instability strip. This second blue loop could only occur in the most massive progenitor and few Cepheids were expected to be observed in this particular phase. It should be noted that the evolutionary behaviour of a stellar model of a given mass can vary greatly depending on the initial chemical composition. This has been noted and extensively discussed in Becker et al (1977) and Becker (1981) (See Fig. 1.5). Recently, new opacities have been calculated which have revised many of the models that have been used. The two main groups are the Geneva models of Schzerer et al (1993) and the Padova models of Fagotto et al (1994). Finally, the progeny of Cepheids will later be

seen as red giants and red supergiants. The intermediate-mass stars will evolve on the asymptotic giant branch and undergo helium-shell flashes during the double hydrogen-burning and helium-burning shell phase. The majority of these stars will then lose their massive envelopes through mass loss and evolve into white dwarfs[a]. A small fraction of the most massive intermediate-mass stars may experience degenerate ignition of the central carbon core and become supernovae[b]. The remaining massive stars will evolve into red supergiants that undergo all the remaining phases of nuclear burning before possibly becoming type II supernovae (Becker 1985).

1.3.1 Binary evolution

The incidence of binaries among Cepheids exceeds 50% (Szabados 1995). This is also comfirmed by the rate of binary formation for early B-stars, which are the progenitors of Cepheids. Madore (1977) found that about 27% of the Cepheids in binary systems have companions of similar mass. Sandage & Tammann (1969) pointed out that one binary system, CE Cas, provided a rare example of a system consisting of two Cepheids. In order for a binary system to evolve to the point where one star, or both stars, could become a Cepheid, the distance between them must be large. If the separation of the stars was sufficiently large[c] then they will continue to evolve through their post-main sequence phases as if they were single stars. If, however the separation was such that one star fills its Roche lobe[d] during its evolution, mass transfer will occur and the subsequent evolutionary behaviour of the two stars will no longer be accurately described by single star evolutionary models. Should such a system be found, the originally more massive of the two stars will have suffered significant mass loss, such as to possibly prevent it ever crossing the instability strip again. The companion star will most likely accrete mass from the more massive star and evolve in a different manner compared to single star. Any subsequent crossing of the instability strip by this star will result in a Cepheid with a luminosity that would be inconsistent with single star evolutionary models.

1.4 Period-Luminosity and Period-Luminosity-Color relations

1.4.1 PL relation

As we have already mentioned before Cepheids are good distance indicator through their Period-Luminosity relation. Its general form is:

[a] A white dwarf is an astronomical object which is produced when a low or medium mass star dies. The white dwarf is supported only by electron degeneracy pressure.

[b] Supernovae refer to several types of stellar explosions that produce extremely bright objects made of plasma, their luminosity decline over a period of weeks or months.

[c] On the order of a few hundred solar radii: $R_{\odot} = 6.96 \cdot 10^{10}$ cm

[d] The volume around a star in a binary system inside which material is bound to that star.

$$\langle M \rangle = \alpha + \beta \log P \tag{1.1}$$

where $\langle M \rangle$ is the mean absolute magnitude of the Cepheid at a given wavelength, P is the period of the variable, α is the zero point and β is the slope of the relation. The PL relation presents an intrinsic scatter in luminosity at a given period. This scatter is correlated to the finite width of the instability strip (see Fig 1.4). At constant period, the B-magnitude total width of the PL relation is about 1.2 mag while the V-magnitude width is measured to be about 0.9 mag. The intrinsically bluest[a] Cepheids are expected to have the brightest absolute magnitudes for a given period. The PL relation is, then, a statistical relation, which provides the average of the Cepheid absolute magnitudes. In estimating distances, any individual Cepheid could deviate from the statistical ridge line by up to ±0.6 mag in B band; such an error (if applied to one Cepheid) would translate into an equivalent error of about ±30% in distance. Large samples can decrease the error on the magnitude inversely with the square root of the number of stars, a formal error of only 10% being possible with a sample containing as few as a dozen Cepheids. However this is true only if the sample of Cepheids well-populated the whole PL relation, i.e. covers a wide range in period.

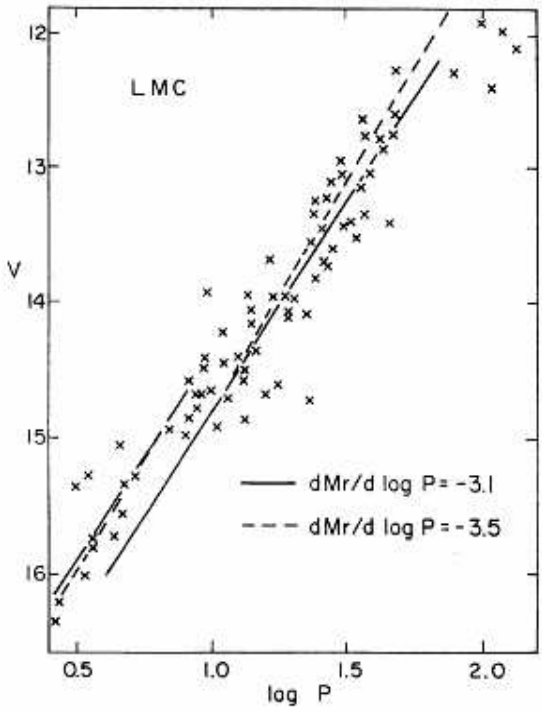

Figure 1.6: *The observed visual magnitudes for Cepheids in the LMC are plotted as a function of log P. The data are divided in two sequences: fundamental (long sequence) and first overtone (short sequence) pulsators (from Böhm-Vitense 1994).*

[a] i.e. hottest, near the left edge of the instability strip.

Different works (e.g. Böhm-Vitense, 1994; Bono et al 2002) pointed out the existence of two distinct PL relations for Cepheids that pulsate in the fundamental (F) mode and in the first overtone (FO) mode (see Fig. 1.6). The range of periods for the FO PL relation is smaller (as we have already mentioned in section 1.2) and also the width of their instability region is significantly smaller than for the fundamental one. Current predictions (Bono et al, 2002) suggest that, at log P=0.3, the width of the FO instability strip is 400 K, while for F Cepheids it is 900 K at log P=1. Therefore, distances based on FO PL relation are less affected by intrinsic spread when compared with F one. Regrettably complete and accurate samples of FO variables are available only for Magellanic Cepheids and the detection of this type of stars in external galaxies is more difficult than for the F Cepheids, since they are fainter and the luminosity amplitudes are smaller. Regarding double-mode Cepheids, theoretical models and observations support the evidence that F and FO modes of double-mode Cepheids follow very well the PL relations of pure F and pure FO pulsators.

As we have already mentioned in section 1.2, the amplitudes of individual Cepheids (see Fig. 1.3) decrease with the wavelength of the observation, this is due to a much decreased sensitivity of the infrared surface brightness to the temperature. For exactly the same reason, the observed width of the PL relation decreases dramatically with the wavelength (see Fig 1.7). In the infrared bands the PL relation shows a remarkably small scatter ($\pm$0.2 mag). Thus, Cepheids observed at long wavelengths and at random points in their cycle are closer to their time-averaged mean magnitudes than the equivalent observation at shorter wavelengths.

From B band to K band the width of the PL relation decreases from 1.2 mag to 0.5 mag. As a result, for distance determinations even single, random-phase observations of known Cepheids, when made in the near-infrared, are comparable in accuracy to complete time-averaged magnitudes (derived from a dozen or more observations) in the blue.

1.4.2 PL-Color relation

The attempts to understand the scatter of the PL relation led to the empirical formulation of a PL-Color (PLC) relation (Sandage 1958). The PLC relation is simply a restatement of Stefan's law and it is therefore applicable to stars on an individual basis, at variance with the PL relation that is a statistical relation for ensembles of stars. Stefan-Boltzmann's law states:

$$L = 4\pi R^2 \sigma T_{\rm eff}^4 \tag{1.2}$$

where L is the luminosity of the star, the radius R of the star is a geometric term that parametrises the total emitting surface area $4\pi R^2$ and the effective temperature $T_{\rm eff}$ is a thermal term used to parametrise the areal surface brightness $\sigma T_{\rm eff}^4$. Expressed in magnitudes, Stefan-Boltzmann's law becomes:

$$M_{\rm BOL} = -2.5 \log \frac{L}{L_\odot} + 4.70 = -5 \log R - 10 \log T_{\rm eff} + C \tag{1.3}$$

where M_{BOL} is the bolometric magnitude[a] and C is a constant . The radius and the temperature

[a]The brightness of an object integrated over all the wavelengths.

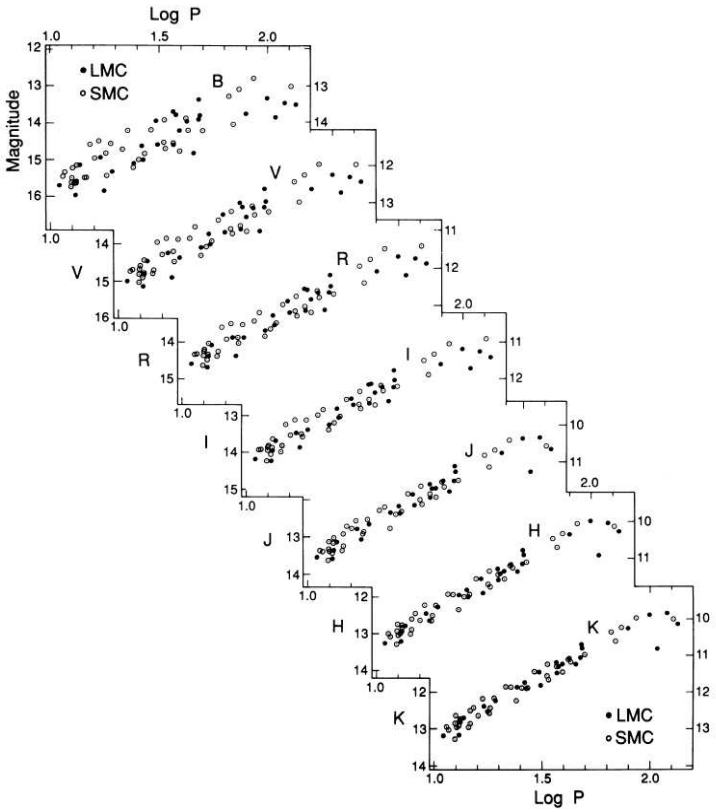

Figure 1.7: *Magellanic Clouds Cepheid PL relation at seven wavelengths, from the blue to the near-infrared. The LMC Cepheids are shown as filled circles; the SMC data, shifted to the LMC distance, are shown as open circles (from Madore & Freedman 1991). Note the decreased width of the relations as longer and longer wavelengths are considered.*

can be related to two observable characteristics of a Cepheid: its period and an intrinsic colour[a]. Considering the period-density relation:

$$P\sqrt{\rho} = Q \tag{1.4}$$

where ρ is the mean density of the star and Q is the pulsational constant[b], and the definition of the total mass $\mathcal{M}$ of the star:

$$\mathcal{M} = \frac{4}{3}\pi R^3 \rho \tag{1.5}$$

we can then correlate the radius with the pulsational period and use the latter as observable

[a] More correctly colour index, that is the difference of magnitude between two different wavebands.
[b] Its value for Cepheids is determined theoretically and it varies from 0.042 to 0.043 (Christy 1966)

parameter instead of requiring a direct measurement of R. The effective temperature can be linearly mapped into an observable intrinsic colour index.

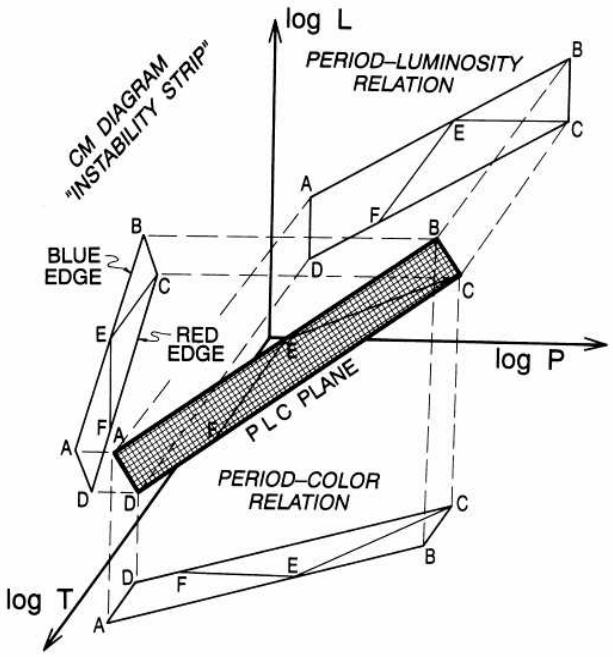

Figure 1.8: *The Cepheid Manifold: projections of the PLC plane (shown shaded) onto three principal coordinate systems (luminosity [*log *L] increasing up, period [*log *P] increasing to the right and color [*log *T] becoming bluer/hotter to the lower left). The backward projection onto the (*log *L,* log *P) plane gives the period-luminosity relation. Projecting to the left gives the position of the instability strip within the color-magnitude (i.e. HR) diagram. Projecting down gives the period-color relation. EC is a line of constant luminosity. EF is a line of constant color. AD and BC are lines of constant period. (from Madore & Freedman 1991).*

We thereby predict a two-parameters description of the luminosity of pulsating stars. This is the physical basis for the PLC relation for Cepheids, which takes the following form in the visual band:

$$M_V = \alpha + \beta \log P + \gamma (B-V)_0 \tag{1.6}$$

where $(B-V)_0$ is the intrinsic colour index (i.e. without the effect of the interstellar extinction), α is the zero point, β and γ are the coefficients of the period and colour terms. Analogous expressions can be written for other photometric bands. To use the PLC formalisation one must observe a colour index, correct it to an intrinsic colour index, and then independently determine a pulsational period in order to calculate an absolute luminosity.

Figure 1.8 shows the projections of the PLC plane onto three principal coordinate systems. Its projections on the Luminosity-Period plane and the Period-Temperature plane correspond to the

PL and Period-Colour (PC) relations, while the projection on the Luminosity-Temperature plane (or HR diagram) is the instability strip. As mentioned before the instability strip defines a range of luminosities and colours over which pulsation is a stable mode for a star and is, therefore, an observable. But this constraint does not control the detailed correlations between period, temperature and luminosity, nor does it control the interdependence of the observed parameters for individual stars. The Cepheid constraint, in the form of an instability strip, controls the statistical properties of the ensemble of Cepheid stars. These statistical trends of the period-luminosity and period-colour relations are incomplete, and even sometimes misleading, descriptors of the individual stars. The properties of individual Cepheids can never be accurately defined by the constraints on the PLC relation but only by the PLC relation itself. The use of this relation, once calibrated, allows to determine the luminosity, i.e. the distance, of an individual Cepheid.

1.4.3 Uncertainties

At first sight calibration of the PL(C) relation might seem a straightforward task. All that is required are accurate values for α and β (and γ). However, some difficulties lie in the technicalities of obtaining these quantities. The main issues are the determination of independent distances and independent photometry and reddenings for the Galactic and Magellanic populations of Cepheids. The Magellanic Clouds, along with our Galaxy, have long been the testbed for the calibrations of the PL and PLC relations because they are nearby and because of the large numbers of Cepheids cataloged in them (OGLE project, Udalski et al 1999a, 1999b).

Different methods are adopted to determine individual distances of Galactic Cepheids. The massive and homogeneous astrometric[a] survey carried out by the Hipparcos mission (Perryman et al 1999) produced data for a significant sample of Cepheids with a good estimates of standard errors of the individual parallaxes[b]. Although trigonometrical parallaxes available for Cepheids are affected by large percentage errors and they cannot be used to derive a trustworthy zero point of the PL relation. Using a significant sample of Cepheids is possible to determine the zero point applying the method of statistical parallaxes. This method combines proper motions and radial velocities and it assumes that the relative distances of the stars are known and only a scale value is to be derived. It also requires a kinematic model based on differential galactic rotation, because both the proper motions and the radial velocities show clearly and independently the dominant effect of differential galactic rotation on Cepheid motions in the Galaxy (Pont et al 1994; Feast & Whitelock 1997).

For Cepheids belonging to open clusters a second method can be utilised: the main-sequence fitting procedure. There are 30 open clusters in our Galaxy which have been listed as containing Cepheids (Feast 1999). The main-sequence fitting technique derives a relative distance from the comparison of the main-sequence[c] of the cluster under scrutiny to a suitable "template". The

[a] Astrometry is the science of measurements of stellar position and motion.

[b] Parallax is the angle subtended at a star by the mean radius of the Earth's orbit around the Sun. The distance of the star, in parsec, is the reciprocal of the parallax.

[c] The curve where the majority of stars are located in HR diagram. Main-sequence stars or dwarf stars are burning hydrogen in their core (see Fig 1.4).

absolute distance of the cluster then, is derived by adding the distance of the cluster used as template. Usually the template adopted is the main-sequence of the Pleiades or the Hyades, these two clusters are well studied and their distances are well known through the Hipparcos measurements of parallaxes. However there are some problems associated to this method: uncertainties of cluster membership, in some cases cluster membership of Cepheids appears doubtful (e.g. Orsatti et al 2001); uncertainties in the photometry or in the adopted reddenings; errors on the distance of the template cluster and effects of the metallicity on the position of the main sequence in the HR diagram. It is generally assumed that all the clusters containing Cepheids are of solar metallicity or at least of solar metallicity on the mean. The latter seems more likely but it has not been proved and further work on the metallicities of open clusters and their Cepheids would be desiderable. The main-sequence fitting technique can be applied also to open clusters in the Magellanic Clouds to determine distances of Cepheids but, then, the correction to the main sequence position due to metallicity effects is crucial (Walker et al 2001), since these galaxies have sub-solar metallicities (1/3 and 1/5 of the solar value for the LMC and the SMC, respectively), while the templates have mostly a solar metallicity. For an in-depth discussion of these methods and their uncertainties see Feast (2003).

The Baade-Wesselink (BW) method can also be applied to determine distances of Galactic and Magellanic Cepheids and it combines stellar radii with surface brightness measurements. It will be discussed extensively in Chapter 2.

The errors on the calibration of the Galactic PL relation, i.e. determination of the zero point, using these methods are between 0.05 and 0.15 mag and the unweighted mean value for the zero point is -1.40 mag (Feast 2003). However, while both trigonometrical and statistical parallax methods are rather robust, the cluster and BW methods both have small internal errors (~ 0.05) but their real (external) uncertainties are difficult to quantify. It can be concluded that the zero point of the Galactic PL relation can be estimated with an uncertainty of $\sim$0.1 mag, at least for Cepheids with near solar abundances.

When it is not possible to determine individual distances (e.g. with the BW method) of Cepheids in the Magellanic Clouds, it is a fair approximation to assume they are equal to the distance of their parent galaxies with a corrections for depth and projection effects. Regrettably, while the relative distance between the Large and the Small Magellanic Cloud has been assessed with a good precision, we can find in the current literature values of the distance of the LMC ranging from 18.1 to 18.8 mag (i.e. between 41 and 57 Kpc), not always obtained with different techniques (for a review on the results and methods see Benedict et al 2002; Gibson 2000). However it seems that the most recent determinations of the LMC distance are converging towards a common value around 18.5 mag, i.e. 50 Kpc, (e.g. Romaniello et al 2000; Walker 2003; Borissova et al 2004) and this is the value commonly adopted to calibrate the PL relation of this galaxy. The errors on the distances of the Magellanic Clouds are of the order of $\sim$0.1.

The second crucial issue related to the calibration of the PL(C) relation is the photometry and reddening measurements. It is fundamental to obtain high-precision measurements of the apparent magnitude and colours to derive a time-averaged magnitude and the reddenings of Cepheids. These quantities depend on correct period phasing and proper light curve fitting is necessary. A large number of data points to build an accurate light curve in order to yield a high precision average

magnitude. This makes colours and mean magnitudes based on short-wavelength observations more costly in observing time than their longer-wavelength counterparts, because more data points are needed to determine the time-average magnitudes with the same accuracy of the infrared bands. Current high-precision measurements of the apparent magnitudes and colour indexes in the visual and infrared bands have errors around 0.01 mag (e.g. Laney & Stobie 1994, Berdinkov & Turner 2001). Multi-wavelengths observations allow to calculate the reddening from colour-colour plots and from the period-colour relation (see Dean at al 1978; Laney & Stobie 1993). The errors on the extinction coefficients are around $\sim$0.05 mag.

Another important source of uncertainty is the effect of the metallicity on the PL and PLC relations, the study of which is the main goal of this thesis project. We will discuss about it in more details in section 1.6.

1.5 The distance scale

Cepheids are the best known primary distance indicators, they are used to provide the step from our Galaxy to the nearby universe and to calibrate secondary distance indicators, such as supernovae type Ia (SNeIa) and the Tully-Fisher relation[a]. Among the "desirable properties" of Cepheids are that they:

- are bright compared to most other stellar distance indicators;
- are easy to recognise by their variability;
- have been studied for a long time and are physically well understood;
- are long-lived and stable, hence can be re-observed;
- individually are precise distance indicators (using the PLC relation) which do not rely on the integrated properties of a whole population;
- are common enough in the spiral galaxies that large samples can be accumulated to beat down statistical noise.

On the other side of the coin, Cepheids:

- cannot be observed far enough, with current technology, to measure directly the Hubble constant H_0, i.e. they can only be observed in galaxies among which the gravitational interactions are more important (local universe) than the relative motion of non-interacting galaxies due to the expansion of the universe.

[a]The Tully-Fisher relation measures the distance to rotating spiral galaxies by the width of the galaxy's spectral lines. This empirically-derived relation states that the luminosity of a galaxy is directly proportional to the fourth power of its rotational velocity, which can be calculated from the width of the spectral line, especially the 21-cm hydrogen line.

- are Population I objects so they are not found in the elliptical galaxies, composed by old stars;
- in the Milky Way are barely within the reach of geometrical distance determination and tend to suffer high extinction due to dust in the disk;
- are still difficult to model in some respects, particularly concerning the location of the red edge of the instability strip in the HR diagram.

Even with these drawbacks much has been accomplished using these stars as first step of the extragalactic distance scale and to calibrate several secondary distance indicators.

The PL relations are calibrated locally in the Milky way and in the Magellanic Clouds. In recent years, extragalactic studies have mostly used PL relations derived in the LMC. Prior to HST, Cepheids had only been well studied in the Local Group and other galaxies within about 4 Mpc (Cepheids had been detected in more distant galaxies but only in very small numbers). At that time very few of these galaxies were useful for checking and calibrating secondary distance indicators. With HST the situation has changed dramatically so that 30 new galaxies have been observed for Cepheids reaching to 30 Mpc and more. Furthermore, these were mostly chosen specifically to be useful from the point of view of secondary indicators (Freedman et al 2001).

Establishing accurate distances over cosmologically significant scales is crucial to pin down the value of the Hubble constant (see Jensen et al 2003 for a review on the extragalactic distance scale). This constant sets the correlation between the recession velocity v of a galaxy and its distance d, i.e. the Hubble law: $v = H_0 d$, that provides the evidence for the expansion of the universe. H_0 enters in a practical way into numerous cosmological and astrophysical calculations. Its inverse sets the age of the universe, t_0, and the size of the observable universe, $R_{obs} = ct_0$, given a knowledge of the total energy density of the universe. The square of the Hubble constant relates the total energy density of the universe to its geometry (Peacock 1999).

The current value of H_0 is now known with an accuracy of 10% and this is largely due to the tremendous increase in the number of galaxies in which Cepheids have been discovered that we have mentioned above (HST Key Project, Freedman et al 2001). Incresingly accurate secondary distance indicators, many calibrated using Cepheids, now provide largely concordant measurements of H_0. The result reported by Freedman et al is H_0=72$\pm$8 km^{-1} Mpc^{-1}. The largest sources of errors result from photometric calibration of the HST Wide Field and Planetary Camera 2, uncertainties in the distance to the LMC and the effects of the metallicity on the Cepheid PL relation.

1.6 The metallicity problem

The debate on the role played by the chemical composition on the pulsational properties of Cepheids is still open, with different theoretical models and observational results leading to markedly different conclusions.

From the theoretical point of view pulsational models by different groups lead to substantially different results. Linear models (e.g. Chiosi et al 1992; Sandage et al 1999; Baraffe & Alibert 2001), based on nonadiabatic pulsational models, suggest a moderate dependence of the PL relation on the

metallicity. The predicted change is less than 0.1 mag over the metallicity[a] interval from Z=0.004 to Z=0.02 at log(P) = 1, independent of wavelengths. Non-linear convective models (e.g. Bono et al 1999; Caputo et al 2000) instead predict a larger dependence on the same interval of metallicity: the change is 0.4 mag in V, 0.3 mag in I and 0.2 mag in K, again at log(P) = 1. Moreover, the predicted change in these latter models is such that metal-rich Cepheids are *fainter* than metal-poor ones, at variance with the results of the linear models. Fiorentino et al (2002) and, more recently, Marconi et al (2005) investigations, also based on non-linear models, suggested that there may be also a dependence on the helium abundance.

On the observational side, the majority of the constraints comes from indirect measurements of the metallicity, mostly in external galaxies, such as oxygen nebular abundances derived from spectra of H II regions at the same galactocentric distance of the Cepheid field (e.g. Sasselov et al 1997; Kennicutt et al 1998; Sakai et al 2004). These analyses indicate that metal-rich Cepheids are *brighter* than metal-poor ones (hence at variance with the predictions of non-linear convective models), but it is important to note that the results span a disappointingly large range of values (see Table 1.1 and Fig. 1.9).

In order to better constrain a possible dependence of the Cepheid PL relation on the metallicity, a better approach is to measure directly the metal content of Cepheid stars, which, so far, has been attempted only by few studies, primarily focused on stars of our own Galaxy (cf Fry & Carney 1997; Andrievsky et al 2002a, 2002b, 2002c and 2004; Luck et al 2003).

Fry & Carney (1997, hereafter FC97), for instance, have derived iron and α element[b] abundances for 23 Galactic Cepheids from high resolution and high signal-to-noise spectra. They found a spread in [Fe/H] of about 0.4 dex, which they claim it is real. With approximately half of their sample (stars belonging to clusters or associations) they have made a preliminary evaluation of metallicity effects on the zero point of the PL relation, finding that metal-rich Cepheids are brighter than metal-poor ones at the same period. Thus, finding a result similar to the studies based on indirect measurements of the metallicity.

The impressive observational effort carried out by Andrievsky and collaborators (Andrievsky et al 2002a, 2002b, 2002c; Luck et al 2003; Andrievsky et al 2004) has instead taken advantage of high resolution spectra of 130 Galactic Cepheids (collected with different instruments at different telescopes) in order to determine their chemical composition and study the Galactic abundance gradient. In relation to our work, it is important to note that Andrievsky and collaborators did not investigate the effects of the chemical composition on the Cepheid PL relation: on the contrary, they used the PL relation to determine the distances of their stars.

Outside our Galaxy, Luck & Lambert (1992, hereafter LL92) have studied 10 Cepheids in the Magellanic Clouds (5 in the Large and 5 in the Small MC). For the Large Magellanic Cloud (LMC), they found a mean [Fe/H] of -0.36 dex with a dispersion of 0.3 dex, while for the Small Magellanic Cloud (SMC) the mean [Fe/H] is -0.6 dex with a rather small dispersion (less than 0.15 dex). A more recent study by Luck et al (1998, hereafter L98) on 10 LMC Cepheids and 6 SMC Cepheids, 4 of which in common with LL92, confirmed the mean [Fe/H] value in the LMC (-0.30 dex),

[a]The metallicity of an object is the proportion in mass of its matter made up of chemical elements other than hydrogen and helium. It is indicated with Z.

[b]Light elements with an even atomic number: C, O, Mg, Si, S, Ar, Ca, Ti

Table 1.1: *Overview of recent observational results for the metallicity sensitivity of Cepheid distances. In the first column is listed the variation of the distance modulus μ per dex of metallicity, the negative sign indicates that the true distance is longer than the one obtained not taking in account the effect of the metallicity. In the second column is listed the elemental abundance used as reference for the metallicity. The third and fourth columns report the method and the reference of the different studies. See Fig. 1.9.*

$\delta\mu/\delta[M/H]$ (mag/dex)		Method	Reference
-0.32 ± 0.21	[Fe/H]	Analysis of Cepheids in 3 fields of M31 (BVRI bands)	Freedman & Madore (1990)
-0.88 ± 0.16	[Fe/H]	Comparison of Cepheids from 3 fields of M31 and LMC (BVRI bands)	Gould (1994)
-0.40 ± 0.20	[O/H]	Simultaneous solution for distances to 17 galaxies (UBVRIJHK bands)	Kochanek (1997)
$-0.44^{+0.10}_{-0.20}$	[O/H]	Comparison of EROS observation of SMC and LMC Cepheids (VR bands)	Sasselov et al (1997)
-0.24 ± 0.16	[O/H]	Comparison of HST observation of inner and outer fields of M101	Kennicutt et al (1998)
-0.12 ± 0.08	[O/H]	Comparison of 10 Cepheid galaxies with Tip of the Red Giant Branch distances	Kennicutt et al (1998)
-0.20 ± 0.20	[O/H]	Value adopted for the HST Key Project final result	Freedman et al (2001)
0	[Fe/H]	OGLE result comparing Cephieds in IC1613 and MC (VI bands)	Udalski et al (2001)
0	[O/H]	Comparison of Planetary Nebula luminosity function distance scale and Surface Brightness fluctuation distance scale	Ciardullo et al (2002)
-0.24 ± 0.05	[O/H]	Comparison of 17 Cepheid galaxies with Tip of the Red Giant Branch distances	Sakai et al (2004)
-0.21 ± 0.19	[Fe/H]	Baade-Wesselink analysis of Galactic and SMC Cepheids (VK bands)	Storm et al (2004)
-0.23 ± 0.19	[Fe/H]	Baade-Wesselink analysis of Galactic and SMC Cepheids (I band)	Storm et al (2004)
-0.29 ± 0.19	[Fe/H]	Baade-Wesselink analysis of Galactic and SMC Cepheids (W index)	Storm et al (2004)
-0.27 ± 0.08	[Fe/H]	Compilation from the literature of distances and metallicities of 53 Galactic and MC Cepheids (VIWK bands)	Groenewegen et al (2004)

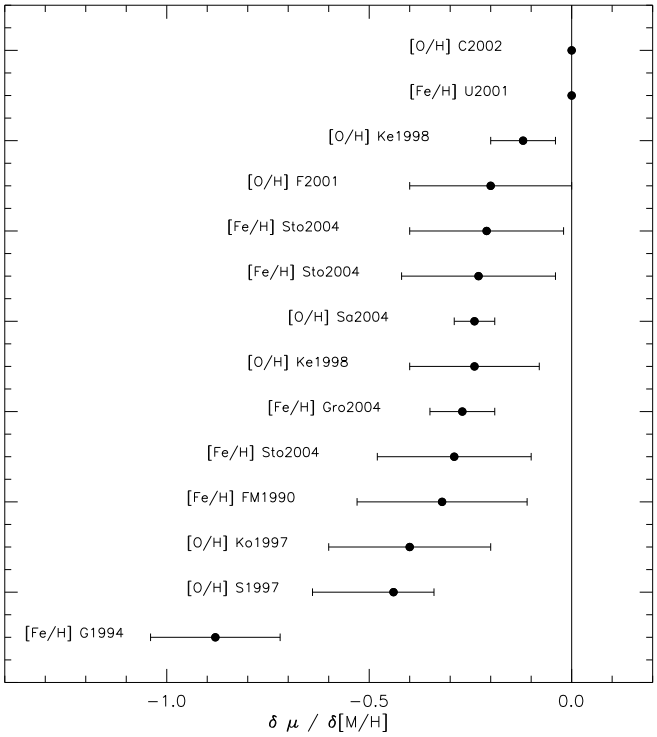

Figure 1.9: *Comparison of recent results for the metallicity sensitivity of Cepheid distances. FM1990: Freedman & Madore (1990); G1994: Gould (1994); Ko1997: Kochanek (1997); S1997: Sasselov et al (1997); Ke1998: Kennicutt et al (1998); F2001: Freedman et al (2001); U2001: Udalski et al (2001); C2002: Ciardullo et al (2002); Sa2004: Sakai et al (2004); Sto2004: Storm et al (2004); Gro2004: Groenewegen et al (2004). See Table 1.1.*

found very little evidence of a significant metallicity dispersion in the LMC (contrary to LL92, but similarly to the SMC), and slightly revised downwards the mean [Fe/H] of the SMC (-0.74 vs -0.60 from LL92).

Finally, we mention two recent works that have followed slightly different approaches. Groenewegen et al (2004) have selected from the literature a sample of 37 Galactic, 10 LMC and 6 SMC Cepheids for which individual metallicity estimates and BVIK photometry were known. Their work aimed at investigating the metallicity dependence of the PL relation using individual metallicity determinations as well as good individual distance estimates for Galactic Cepheids. They inferred a metallicity effect of about $-0.27\pm$ 0.08 mag/dex in the zero point in the V, I, K bands and the Wesenheit index W[a], in the sense that metal-rich Cepheids are brighter than the metal-poor ones (see Table 1.1 and Fig. 1.9, for a comparison with other studies). Also Storm et al (2004) discussed the effect of the metallicity on the PL relation using 34 Galactic and 5 SMC Cepheids, for which

[a]Reddening-free index defined as: W=V-2.42(V-I), where 2.42 is the coefficient of extiction.

they determined accurate individual distances with the Baade-Wesselink method. Using an average abundance for the SMC Cepheids of [Fe/H]= −0.7 and solar metallicity for the Galactic ones, they determined, in a purely differential way, the following corrections: −0.21± 0.19 for the V and K bands, −0.23± 0.19 for the I band and −0.29± 0.19 for the Wesenheit index W. These are in quite good agreement with Groenewegen et al (2004).

Despite all these efforts, it is important to underline that none of the observational studies undertaken so far has directly determined several elemental abundances of Cepheids in order to explicitly infer the effect of the metallicity on the PL relation, taking advantage of a large sample that has been homogeneously analysed. Therefore, this kind of analysis is the necessary step to improve our knowlegde about the metallicity effect and put tight constraints to the theoretical models.

1.7 This thesis project

The aim of this thesis is to assess the effect of the metallicity on the Cepheid Period-Luminosity relation

The novelty of the approach adopted in this project consists exactly in what we have just mentioned in the previous section: the homogenous analysis of a large sample of Cepheids (72) observed in three galaxies (the Milky Way, the Large Magellanic Cloud and the Small Magellanic Cloud), spanning a factor of ten in metallicity. This allows us to explore the effect of metallicity on the PL relation in a wide range and to study the gas enrichment histories of three different galaxies.

To fulfil these goals, firstly, we have selected a sample of Cepheids for which distances and accurate photometry are available in the literature and we have collected high-resolution, high signal-to-noise spectra of these stars, using the highly advanced facilities of the European Southern Observatory in Chile. Secondly, we have directly measured iron and α-elements (O, Na, Mg, Al, Si, Ca, Ti) abundances of our sample from these spectra.

With these results at hand:

- we make a comparison with previous works on the chemical composition of Cepheids and of different stellar populations;
- we explore the behaviour of the abundance ratios relative to iron of the α-elements to verify the theoretical predictions for the star formation histories of the Galactic disc and the Magellanic Clouds;
- we investigate the effect of the metallicity on the PL relation in the V and K bands, studying the behaviour of the residuals in two luminosity bands determined from the photometry for our sample and the standard PL relations from the literature as a function of the measured metallicity.

Chapter 2 discusses the observational aspect of this thesis. The selection criteria of the data set are described along with telescopes and instruments used to collect the stellar spectra. We

illustrate the data reduction process and the photometry and the stellar distances we have selected from the literature for our project.

In Chapter 3 a general overview of the analysis of the spectra is outlined, followed by a detailed description of the methodology used to calculate the elemental abundances: assembling the line list, determining the equivalent widths and the atmospheric parameters and computing the abundances with the adopted model atmospheres. An alternative method to determine elemental abundances, the spectrum synthesis technique, is also explained.

The results of the determination of the iron abundances of our data set are illustrated in Chapter 4. We discuss the sources of uncertainties on the abundances and the comparison with results from other observational studies on Cepheids and on different stellar populations.

In Chapter 5 the abundances of the α-element are presented along with a discussion of the behaviour of their abundance ratios relative to iron as a function of the iron content of the stars of our sample. The determination of the oxygen abundances is detailed, since it is the only element for which we have used the spectrum synthesis method.

The investigation of the effect of the iron content and of the total metallicity on the PL relation in the visual and infrared bands, namely V and K bands, is presented in Chapter 6. We examine the effects on the slope and zero point of the relation and the net effect on the luminosity and compare our outcomes with two different hypothesis currently reported in the literature.

As last part we summarise the work done and results obtained. We also briefly outline the future work that could be undertaken to gain further understanding on the effect of the chemical composition on the properties of Cepheids.

Chapter 2

Observations

Significant progress has been made in the past few years towards the understanding and the characterisation of the Cepheid Period-Luminosity (PL) relation, both on the observational and theoretical sides (see section 1.6), but the debate on the role played by the chemical composition is far from being settled. In particular, from an observational standpoint, the subject has been approached in essentially two ways: either by direct measurements of the elemental abundances in nearby Cepheids, or by measuring a secondary metallicity indicator in external galaxies known to contain Cepheids, under the assumption that they would have the same chemical composition. Regrettably, the direct determination of chemical abundances has been attempted, up to now, only by few studies, mainly focused on stars of our own Galaxy (see section 1.6). This approach require high quality spectra of the stars under scrutiny and these are easier to obtain, from ground-base telescopes, for Cepheids that are close to the Sun, limitating the range in metallicity that can be explored. Therefore, to further tackle this problem, we decided to undertake a detailed chemical analysis (focusing on iron and α-elements) of a large sample of Cepheids in the Galaxy and the Magellanic Clouds, adopting the first of the two approaches described above: the direct determination of abundances. In order to do this we have obtained high quality spectra, i.e. with high resolution and high signal-to-noise, that have been collected using the highly advanced facilities of the European Southern Observatory (ESO) in Chile. We will use the elemental abundances, directly determined from the spectra of this sample, to assess the effect of the metallicity on the PL relation.

2.1 Selection criteria and characteristics of the data-set

The data-set has been assembled according to the following selection criteria:

- a large coverage of metallicity, hence, we selected stars from three different galaxies: the Milky Way, the LMC and the SMC. They have average metallicities, respectively, around the solar value, a third of the solar value and a fifth of the solar value;

- the availability of well-determined intensity mean magnitudes in the B, V and K bands, to study the effect of the metallicity on the PL relation in the visual and infrared bands;
- a wide range of periods in order to cover the entire PL relation, hence, we chose stars from 2 to 99 days in period.

Our sample includes a total of 72 Cepheid stars: 36 Galactic, 22 LMC and 14 SMC Cepheids. The observing runs were conducted at two different sites (La Silla Observatory and Paranal Observatory) and observing time was allocated in October 2000 and in January-February 2001. For each star we have a single epoch observation.

The spectra of the 36 Galactic stars were collected at the ESO 1.5 m telescope on Cerro La Silla with the Fibre-fed Extended Range Optical Spectrograph (FEROS, Pritchard 2004, see also Section A.2), in two different runs by Drs Martin Groenewegen and Emanuela Pompei.

The spectra of the 22 Cepheids in the LMC and the 14 Cepheids in the SMC were obtained at the VLT-Kueyen telescope on Cerro Paranal with the UV-Visual Echelle Spectrograph (UVES, Dekker et al 2000; Kaufer et al 2004, see also Section A.3) in Service Mode (observations are carried out by the staff of Paranal Observatory).

2.2 Data reduction

The reduction process converts raw 2-D information obtained by observation into the high quality 1-D spectra used for subsequent analysis. This process is crucial and great care must be taken to avoid adding systematic errors or failure to remove artifacts in the data which may lead to misleading or incorrect results.

The reduction process must address several issues, such as contamination of the raw data by external sources not associated with the observation, converting the raw information into a more readily usable form, appropriately dealing with physical phenomena associated with the instruments used and the calibration of the data.

Contamination of the raw data can take many forms, which include noise, or spurious features introduced by natural phenomena, such as cosmic-rays, background radiation and systematic errors introduced by the instrumentation used. The reduction process therefore must be able to recognise these effects and either remove them or take them into account when performing other steps.

In converting the raw information to a form more readily usable for further analysis, it is necessary to convert the charge collected by the pixels of the detector to the corresponding amounts of flux being emitted from the star. Among the steps to be taken are the removal of the CCD background and the location of the spectral orders. This flux then has to be calibrated for wavelength using calibration spectra obtained before and after the object observation (in our case from an Thorium-Argon lamp), correcting for the effects produced by the spectrograph and the removal of the spurious effects mentioned above. Finally the output data should be of a standardised form.

The data obtained were run through the respective instrument Data Reduction Softwares (DRS). Both the FEROS and UVES DRS are particular contexts of the ESO-MIDAS software (Munich Image Data Analysis System). This is essentially a set of general purpose programs for

the reduction and the analysis of astronomical data, developed at ESO. The FEROS and UVES DRS are automatic procedures that go through the different steps of the reduction we have mentioned above, using as inputs the raw 2-D data, the bias, the flat-fields, the calibration spectra from the lamp.

The calibrated 1-D spectra obtained from the DRS need few additional corrections before being used for the scientific analysis:

- the normalization of the continuum: obtained interactively with the IRAF [a] task *continuum*, for each spectrum has been selected reference points of its continuum, in order to interpolate and subtract it from the spectrum;
- the correction for heliocentric velocity[b] using the *rvcorr* and *dopcor* IRAF tasks;
- the correction for the radial velocity using the *dopcor* IRAF task, the radial velocity was derived measuring the wavelengths of 20 unblended narrow lines well spread over the spectrum, selected among the species FeI, FeII and MgI, and comparing them to the corresponding rest-frame values.

Considering the final spectra we have determined that the signal-to-noise ratios vary between 70 and 100 for the FEROS spectra and between 50 and 70 for the UVES spectra. In Fig. 2.1 an example of the quality of our spectra is showed.

2.3 The Galactic sample

For the Galactic Cepheids we have adopted periods and photometry from Laney & Stobie (1994), Tammann et al (2003), Storm et al (2004) and Groenewegen et al (2004). Three stars have photometric data from Tammann et al (2003) that are not dereddened and for two stars we did not find photometric data. Despite these last five stars cannot be used to assess the effect of the metallicity on the PL relation, they can be included in the analysis of the chemical composition of this sample of Cepheid. Phases (ϕ) at which our stars were observed, periods (logP), individual distances (μ) and BVK magnitudes are listed in Table 2.1.

All of our programme stars are classified in the literature as fundamental pulsators, except EU Tau and SZ Tau which are listed as first overtones and AX Vel as one of the few double-mode pulsators in the Galaxy (Fernie et al 1995).

In Figure 2.2 we plot all of our stars with a known M_V in a log P vs M_V plane, comparing our data with observational PL relations for fundamental and first overtone pulsators taken from Böhm-Vitense (1994), derived for Galactic Classical Cepheids. In this way we can confirm the classification found in the literature of EU Tau and SZ Tau as first overtones. As can be seen in Fig 2.2 both stars are lying on the first overtone PL relation. Their observed periods have been

[a] The Image Reduction and Analysis Facility, IRAF, is, like MIDAS, a general purpose software for the reduction and analysis of astronomical data, developed at the National Optical Astronomy Observatories.

[b] The velocity of the earth relative to the sun.

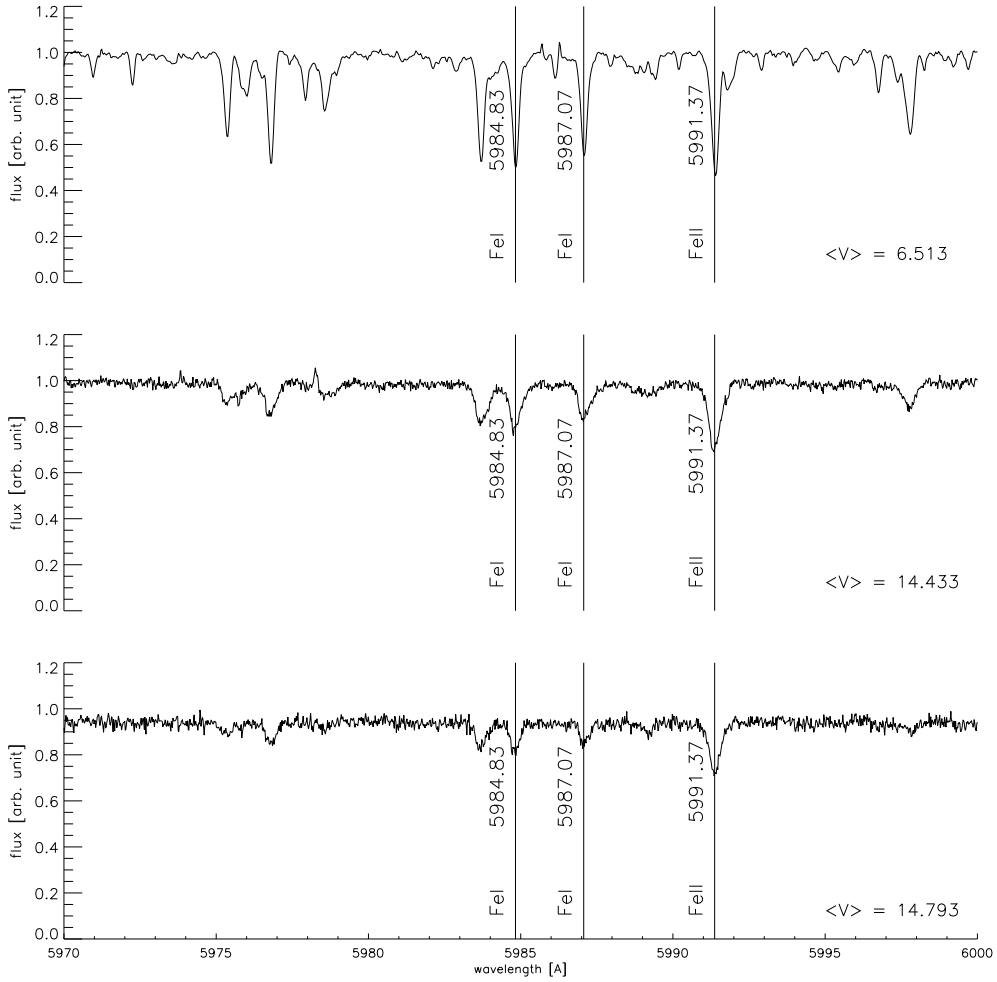

Figure 2.1: *The same spectral range as observed in three different Cepheids characterised by similar periods (top: Galaxy, middle: LMC, bottom: SMC, all three have P = 12 days).*

"fundamentalised" using $P_0 = P_1/(0.716 - 0.027 \log P_1)$ (Feast & Catchpole 1997). We note that most of the data points follow well the PL relation and that there is an intrisic scatter due to the position in the instability strip of the different stars. We can exclude that the two points above the 2-σ confidence region of the fundamental PL relation are first overtone pulsators because theoretical predictions and observations suggest that first overtone Galactic Cepheids have logP$\leq$0.8.

In Figure 2.2 the double-mode AX Vel has been plotted with its fundamental-mode period, however its position corresponds to the first overtone PL relation. This can be due either to the intrinsic scatter of the fundamental PL relation or to an error on its distance estimation that follows from errors on the estimation of its radius (particularly difficult in the case of double-mode cepheids), which in turn means an error on the absolute magnitude we used (see afterwards for a discussion on the errors on the distance estimation). It is better to exclude AX Vel from the analysis of the

PL relation.

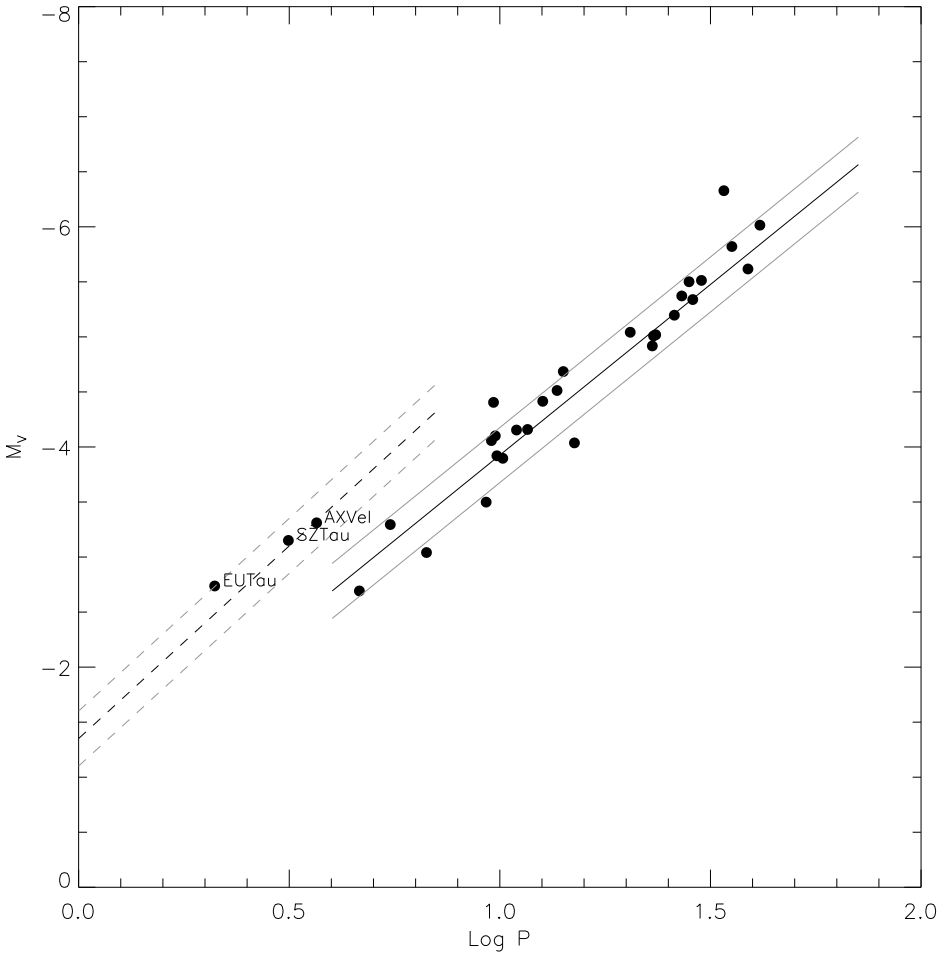

Figure 2.2: *PL relation in the V band for the Galactic Cepheids of our sample. The solid and dashed black lines are empirical PL relations for fundamental and first overtone pulsators from Böhm-Vitense (1994), respectively. Also plotted are the 2-σ confidence regions.*

From the database of the binaries among the Galactic Classical Cepheids (Szabados 2003) we found that 15 stars are spectroscopic binaries and one star (ζ Gem) is a visual binary (see last column of Table 2.1). The companions are B and A-type main sequence stars. To determine the contribution of the companion to the observed spectra we procede as follow:

- we calculate the ages of the Cepheids in the binary systems using the Period-Age-Colour relation at solar chemical composition from Bono et al (2005):

$$t = 8.25\,[\pm 0.08] - 0.76\,[\pm 0.03] \cdot \log P + 0.16\,[\pm 0.06] \cdot (B - V) \tag{2.1}$$

- using isochrones for the calculated ages (between 20 and 50 Myr) from the BASTI database (Pietrinferni et al., 2004), we determined the differences in luminosity between the Cepheids and their dwarf companions.

We observe a large difference in luminosity (> 3 mag) in most of the cases. Thus the dwarf companion does not affect the observed spectrum, which corresponds to the spectrum of the variable star. This is not the case for the two most luminous B dwarfs, companions of KN Cen and S Mus, that give a small contribution to the continuum level of the observed spectra. The effect of these contributions on the final abundances are discussed in Chapter 4.

In order to obtain the absolute magnitudes of our Cepheids, which allow us to investigate the effects of the chemical composition on the PL relation, it is crucial to know the distances to the individual stars. Regarding the individual distances of the 36 Galactic Cepheids, for 25 stars we have adopted the distance moduli (μ) listed in Table 3 of Storm et al (2004) and Table 3 of Groenewegen et al (2004). These individual distances have been obtained using the Baade-Wesselink (BW) method (also known as surface brightness, SB, method). We note that the distance scale based on the calibrations used by Storm et al (2004) and Groenewegen et al (2004) provides, within the errors, the same distances.

The surface brightness method is based on the classical ideas of Baade and Wesselink (Baade 1926; Wesselink 1969) and it was first implemented by Barnes & Evans (1976). The BW method utilises radial changes of the stellar surface thus it can be applied to all stellar objects with radial changing envelopes (for an in-depth review see Gautschy 1987). It has its greatest impact on pulsating variables, due to their role as standard candles. The basic principles of this method are the following:

- the distance D of a star is the ratio between its linear (R) and angular radii (θ):

$$D = \frac{R}{\theta} \tag{2.2}$$

- the angular radius θ is determined from measurements of dereddened magnitudes and colour index (i.e. corrected for the interstellar absorption);
- the linear radius R from the integration of radial velocity curve and dereddened magnitude measurements.

The stellar angular radius can be determined from a SB relation, generally defined as:

$$s = m_1 + 5 \log \theta \tag{2.3}$$

where s is the surface brightness, m_1 the dereddened magnitude and θ the angular diameter. As first pointed out (and determined) by Wesselink (1969), there is a linear correlation between surface brightness and a dereddened colour index that can generally be defined as:

$$s = a + b\,(m_2 - m_3) \tag{2.4}$$

where $(m_2 - m_3)$ is a colour index and a and b are constants, which need to be determined either theoretically or empirically. Combining Eq. 2.2 and Eq. 2.3 is then possible to calculate the angular radius from measurements of the magnitude and colour index in a chosen band for a pulsating star:

$$\theta = 10^{0.2[a+b(m_2-m_3)-m_1]} \tag{2.5}$$

The surface brightness relations written above hold also for the mean linear stellar radius R_0, related to the linear radius as follow: $R(t) = R_0 + r(t)$, where $r(t)$ is the displacement from the mean. The latter can be determined from the integration of the radial velocity curve $v_r(t)$:

$$r(t) = -p \int (v_r(t) - v_\gamma) dt \tag{2.6}$$

where p is the transformation factor from the radial to the pulsational velocity of the star (the latter defined over the pulsational cycle) and v_γ is the centre-of-mass radial velocity of the star. Combining Eq 2.2 and Eq. 2.5 lead to a solution for the radius, R, of the Cepheid.

In the past few decades a whole body of work has been devoted to the determination and calibration of accurate surface brightness relations of dwarf, giant and supergiant stars (e.g. Barnes et al 1978; Di Benedetto 1993; Groenewegen 2004). More recent studies have applied the BW method directly to Cepheids: Fouqué & Gieren (1997), Nordgren et al (2002), Groenewegen (2004) and Kervella et al (2004). These studies indicate that Cepheids and stable giants and supergiants follow identical SB-colour relations and that there is a significant gain in accuracy using infrared colour indices. In conclusion it is possible to determine angular radii of Cepheids from accurate measurements of magnitudes and colour indices using surface brightness relations. Recently it has also been possible to directly measure the angular diameters of some Cepheids using infrared long-baseline interferometry (Kervella et al 2003). This is a significant improvement for the BW method because the determination of the angular radius does not depend anymore on the calibration of a SB relation but it is a geometric measurement.

The uncertainties of the BW method are mainly due to the errors on the linear radius determination. These errors mostly come from errors on the measurements of the radial velocity, the correct evaluation of the p-factor and the phase-match of the magnitudes (from photometry) and radial velocity curve (from spectroscopical observations). The uncertainties on the BW method due to colour indices can be minimised using infrared photometry (for further details see Gautschy 1987, Laney & Stobie 1995).

For the remaining 15 stars of our sample it was not possible to find any determination of their individual distances in the literature. However, in the case of 6 Cepheids (AX Vel, V Car, GH Lup, SX Vel, S Mus and X Pup) it was possible to calculate their distances using the BW method. We have taken the linear diameters from Laney & Stobie (1995) and combined them with the angular diameters determined from the V and K dereddened magnitudes from Laney & Stobie (1994), using two surface brightness-colour calibrations:

- from Groenewegen (2004): we have combined Eq. 1 and Eq. 2 with Table 3 coefficients marked with the filled circle (the V vs. V-K relation)
- from Fouqué & Gieren (1997): we have combined Eq. 1 with Eq. 27 (the V vs. V-K relation)

Since the distance moduli derived with the two calibrations agree very well (within 1%), we have adopted the distances determined with Groenewegen's calibration (these are the values listed in Table 2.1).

Regarding AX Vel, the radius that we have adopted for this star has been determined by Laney & Stobie (1995) using the maximum likelihood method[a]. They have concluded that the quality of the solution for AX Vel is very poor and they have excluded this star from their determination of the Cepheid period-radius relation. Thus we judge the distance obtained for AX Vel (i.e. its absolute magnitude) unreliable and decide to exclude this star from our analysis.

2.4 The Magellanic sample

For the Magellanic Cepheids we have taken periods and photometry from Laney & Stobie (1994). Phases (ϕ) at which our stars were observed, periods (logP) and BVK magnitudes are listed in Table 2.2.

As we already mentioned in the previous section, the good estimates of the distance of a star is crucial to know its absolute magnitude, which is essential for our analysis of the PL relation. For the Magellanic Cepheids, we adopted the distances of their parent galaxies, corrected for projection effects. This assumption is necessary due to the lack of individual determination of distance for our programme Cepheids in the Magellanic Clouds. Considering the values reported in the most recent literature (e.g. Benedict et al 2002; Walker 2003; Borissova et al 2004), we adopted as distance modulus of the barycentre of the LMC the value of 18.50±0.10 mag (i.e. 50±2.3 Kpc). The SMC is taken to be 0.44±0.10 mag (e.g. Cioni et al 2000) more distant than the LMC (i.e a total distance of 61±2.9 Kpc). This value of the relative distance between the two galaxies has confirmed the results of previous studies (Westerlund 1997 and reference therein). Depth and projection effects in the Magellanic Clouds were corrected for using the position angle and the inclination of each galaxy as determined by van der Marel & Cioni (2001, LMC) and Calwell & Laney (1991, SMC).

2.5 Telescopes and instruments

As briefly mentioned in section 2.1, we collected our data sample partly from the La Silla and partly from the Paranal Observatories. The Galactic Cepheids are bright stars and a small telescope is sufficient to collect their spectra, then they have been observed at the La Silla observatory, while the Magellanic Cepheids are fainter and needed a larger telescope such as the VLT at Paranal Observatory.

In the text below will be mentioned many terms that refers to basic principle of spectroscopy that are review in Appendix A.

[a]The maximum likelihood method is the procedure of finding the value of one or more parameters for a given statistics which makes the known likelihood distribution a maximum. The likelihood of a set of data is the probability of obtaining that particular set of data given the chosen probability model.

Table 2.1: *Phases (ϕ) and characteristics of the Galactic Cepheids of the sample.*

ID	$\log P$	ϕ	μ	M_B	M_V	M_K	$E(B-V)$	Duplicity
EU Tau	0.473	0.414	10.27	-2.26	-2.74	-	0.17	Bc
AX Vel	0.565	0.872	10.76	-2.86	-3.31	-4.45	0.24	-
SZ Tau	0.651	0.744	8.73	-2.62	-3.15	-4.50	0.29	B
T Vel	0.666501	0.233	9.80	-2.05	-2.69	-4.26	0.28	B
V Cen	0.739882	0.155	9.18	-2.71	-3.30	-4.77	0.29	-
V Car	0.8259	0.375	9.84	-2.35	-3.04	-4.61	0.18	B
GH Lup	0.9675	0.031	10.05	-2.61	-3.50	-5.34	0.33	B
SX Vel	0.980	0.497	11.44	-3.45	-4.06	-5.52	0.28	-
S Mus	0.985	0.266	9.81	-3.80	-4.41	-5.86	0.22	O
S Nor	0.989194	0.343	9.91	-3.35	-4.10	-5.82	0.19	B
β Dor	0.993	0.529	7.52	-3.16	-3.92	-5.57	0.04	-
ζ Gem	1.007	0.460	7.78	-3.11	-3.90	-	0.01	V
XX Cen	1.039548	0.338	11.11	-3.43	-4.15	-5.80	0.26	B
UU Mus	1.065819	0.865	12.59	-3.43	-4.16	-5.91	0.41	-
U Nor	1.101875	0.422	10.72	-3.71	-4.42	-6.02	0.89	-
BN Pup	1.135867	0.397	12.95	-3.77	-4.51	-6.18	0.44	-
LS Pup	1.150646	0.012	13.55	-3.93	-4.69	-6.36	0.48	B
VW Cen	1.177138	0.967	12.80	-3.15	-4.04	-6.14	0.45	B
RZ Vel	1.309564	0.793	11.02	-4.25	-5.04	-6.83	0.34	-
WZ Car	1.361977	0.745	12.92	-4.14	-4.92	-6.75	0.38	-
VZ Pup	1.364945	0.816	13.08	-4.32	-5.01	-6.55	0.47	-
SW Vel	1.370016	0.792	11.99	-4.21	-5.02	-6.89	0.35	-
X Pup	1.4143	0.232	12.36	-4.40	-5.20	-7.05	0.41	-
T Mon	1.431915	0.574	10.82	-4.40	-5.37	-7.38	0.21	O
RY Vel	1.449158	0.704	12.02	-4.69	-5.50	-7.28	0.56	-
KQ Sco	1.458	0.446	12.36	-4.24	-5.34	-7.67	0.84	-
AQ Pup	1.478624	0.436	12.52	-4.65	-5.51	-7.40	0.51	B
KN Cen	1.531857	0.867	13.12	-5.64	-6.33	-7.94	0.93	B
l Car	1.550855	0.580	8.99	-4.71	-5.82	-7.97	0.17	-
U Car	1.589083	0.489	10.97	-4.73	-5.62	-7.56	0.28	B
RS Pup	1.617420	0.944	11.56	-5.05	-6.02	-8.08	0.45	-
				m_B	m_V			
ST Tau	0.6058	0.5715	-	-	-	-	-	-
RZ CMa	0.6289	0.0313	-	10.703	9.699	-	0.571	-
AP Pup	0.7062	0.1089	-	8.003	7.381	-	0.241	B
RS Ori	0.8789	0.9954	-	9.025	8.413	-	0.335	B
W Gem	0.8984	0.3364	-	-	-	-	-	-

Table 2.2: *Phases (ϕ) and characteristics of the Magellanic Cepheids of the sample.*

ID	$\log P$	ϕ	B_0	V_0	K_0	$E(B-V)$
			LMC			
HV 6093	0.680	0.024	15.74	15.16	13.71	0.06
HV 2337	0.837	0.861	-	-	13.27	0.07
HV 2405	0.840	0.037	-	-	13.45	0.07
HV 12700	0.911	0.342	15.62	14.87	13.14	-0.01
HV 12452	0.941	0.860	15.25	14.60	12.86	0.06
HV 2733	0.941	0.411	14.85	14.34	13.03	0.11
HV 971	0.968	0.237	14.86	14.24	12.70	0.06
HV 2864	1.041	0.055	15.16	14.42	12.79	0.07
HV 2260	1.112	0.144	15.19	14.43	12.69	0.13
HV 997	1.119	0.130	14.94	14.19	12.39	0.10
HV 2352	1.134	0.201	14.49	13.84	12.25	0.10
HV 2580	1.228	0.119	14.33	13.67	11.93	0.09
HV 2836	1.244	0.059	14.85	14.02	12.06	0.18
HV 2793	1.283	0.917	14.49	13.58	11.77	0.10
HV 1013	1.382	0.710	14.39	13.46	11.43	0.11
HV 1023	1.425	0.144	14.48	13.51	11.47	0.07
HV 2294	1.563	0.605	13.19	12.45	10.75	0.07
HV 879	1.566	0.256	14.12	13.15	11.06	0.06
HV 877	1.654	0.682	14.06	12.98	10.79	0.12
HV 2369	1.684	0.136	13.15	12.29	10.40	0.10
HV 2827	1.897	0.880	13.19	12.03	9.82	0.08
HV 5497	1.997	0.321	12.73	11.63	9.45	0.10
			SMC			
HV 1365	1.094	0.184	15.39	14.79	13.22	0.07
HV 1954	1.223	0.847	14.13	13.62	12.15	0.07
HV 817	1.277	0.298	14.13	13.59	12.13	0.08
HV 11211	1.330	0.516	14.36	13.64	11.85	0.06
HV 2209	1.355	0.822	13.99	13.42	11.85	0.04
HV 847	1.433	0.500	14.40	13.66	11.85	0.08
HV 823	1.504	0.873	14.46	13.60	11.59	0.05
HV 865	1.523	0.108	13.55	12.93	11.23	0.06
HV 2064	1.527	0.279	14.28	13.50	11.63	0.07
HV 2195	1.621	0.135	13.85	13.07	11.11	-0.02
HV 837	1.631	0.822	13.95	13.10	11.14	0.04
HV 824	1.818	0.315	13.06	12.27	10.35	0.03
HV 834	1.866	0.557	12.95	12.14	10.21	0.02
HV 829	1.945	0.348	12.61	11.81	9.93	0.03

2.5.1 The ESO-1.5 m telescope and FEROS

The ESO-1.5 m telescope is one of the several telescopes of the La Silla Observatory, which is located at the southern extremity of the Atacama desert in Chile at an altitude of 2400 meters. This telescope is a Cassegrain reflector and is mounted in an English cradle. It has a Cassegrain focus with a focal ratio of f/14.9.

The Fibre-fed, Extended Range, Echelle Spectrograph (FEROS, Pritchard 2004) is a bench-mounted, thermally controlled, prism-cross dispersed echelle spectrograph. It has been mounted at the ESO-1.52m telescope (we collected our data sample in 2001) till October of 2002 then it was transferred to the MPG/ESO-2.20m telescope, where is now permanently mounted.

It is a high resolution (R ∼48,000), high efficiency (20%), versatile spectrograph providing in a single spectrogram almost the complete spectral coverage from 350 nm to 920 nm(see below) . The mechanical and thermal stability of FEROS allow for a precise wavelength calibration based on daytime calibrations and for most purposes additional calibrations during the night are not necessary, thus ensuring a high productivity in terms of scientific data produced. It is possible radial velocity work with accuracies of 25 m/s or better.

FEROS is fed by two fibres providing simultaneous spectra of object plus either sky or one of the two calibration lamps (wavelength calibration and flat-field). The fibres are illuminated via 2.0 arcsec apertures on the sky separated by 2.9 arcmins. A small amount of rotation of the telescope adapter is possible in the rare case that a field star by chance falls on the sky fibre. The resolving power of 48,000 is achieved with a two-slice image slicer (a device that reshapes the circular image of each fibre into a narrow and long segment that behaves like a slit, but with minimum rejection of light) over the spectral range of 350 nm to 920 nm spread over 39 echelle orders (with a typical order value of 40). The detector is an EEV 2048 x 4096 CCD.

Calibration lamp light is delivered to the science fibres in the FEROS Fibre Head via the calibration fibres from the FEROS Calibration Unit.

FEROS provides almost complete spectral coverage from 350 nm to 920 nm. Only the two spectral ranges 853.4 nm to 854.1 nm and 886.2 nm to 887.5 nm are lost due to non overlap of the spectral orders. The main capabilities of FEROS are summarized in Table 2.3 and a schematic overview of the spectrograph can be see in Fig 2.3.

2.5.2 The VLT and UVES

The ESO Very Large Telescope (VLT) is located on Cerro Paranal in the Atacama desert in the northern part of Chile (600 km from La Silla), at an altitude of 2600 meters. The VLT consists of an array of four 8-meter telescopes (Antu, Kueyen, Melipal and Yepun) which can work independently or in combined mode. The telescopes may be used in interferometric mode providing extrimely high spectral resolution corresponding to baselines of several hundred meters. Each unit telescope has an alt-azimuth mount and a Ritchey-Chretien optical system. The VLT can operate in either Cassegrain or Nasmyth focus. The VLT uses active optics: the optical quality of the image is continually monitored by an image analyser using a reference star and the contributions of the various optical aberrations are computed and corrected for.

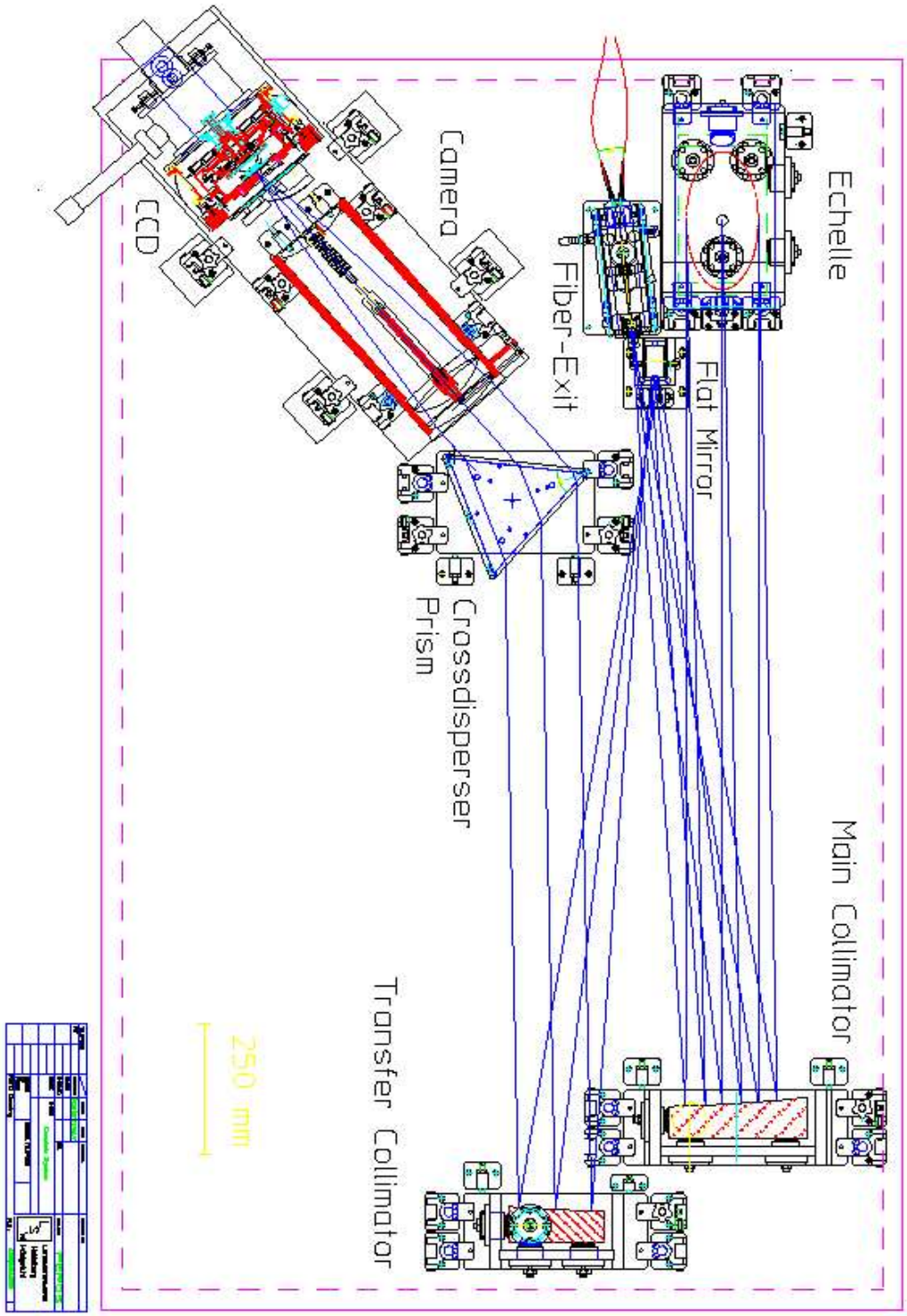

Figure 2.3: *The FEROS complete system as seen from the top.*

Table 2.3: *Main parameters of FEROS.*

Wavelength range in one exposure (object + sky)	3700 - 8600 Å (40 orders, 2 fibers)
Resolving Power (with 2-slice image slicer)	$\lambda/\Delta\lambda = 48{,}000$
Entrance Aperture	2.7 arcsec
Fiber Input/Output Focal Ratio	F/4.6
Spectrograph Beam Size	136 mm diameter
Off-axis Collimators	F/11, cut from one parent paraboloid
Echelle	R2, 79 lines/mm, 154 mm by 306 mm
Crossdisperser Prism	LF5 glass, 55deg: apex angle
Wavelength Range	350 - 900 nm
F/#	F/3.0
Focal Length	410 nm
Field Diameter	69 mm
Image Quality (E_{80})	< 25 μm
Camera Efficiency	$> 85\%$
CCD	2048 x 4096, 15 μm, thinned
Detection Efficiency (without telescope)	7% (3,700 Å), 27% (5,000 Å), 8% (9,000 Å)
Limiting Magnitudes at the ESO 1.52	16 mag in V (S/N = 15, 2 h)
	12.5 mag in V (S/N = 100, 2 h)
Radial-Velocity Accuracy	< 25 m/s, < 5 m/s with iodine cell (contract: < 50 m/s)

2 Observations

UVES (Dekker et al 2000; Kaufer et al 2004), the Ultraviolet and Visual Echelle Spectrograph located at Nasmyth platform B of the second Unit Telescope (Kueyen) of the VLT, is a cross-dispersed echelle spectrograph designed to operate with high efficiency from the atmospheric cut-off at 300 nm to the long-wavelength limit of the CCD detectors of 1100 nm. To this purpose, the light beam coming from the telescope is split into two arms (UV-Blue and Visual-Red) within the instrument. The two arms can be operated separately or in parallel with a dichroic beam splitter. The resolving power is 40,000 when a 1 arcsec slit is used. The maximum resolution (to be obtained with a narrower slit or with the use of an image slicer) is 80,000 or 110,000 in the Blue and the Red Arm, respectively. The instrument is built for maximum mechanical stability and for accurate calibration of the wavelength scale down to an accuracy of at least 50 m/s. An iodine cell can be inserted in the light beam for observations requiring higher accuracy.

The main capabilities of the two UVES arms are summarized in Table 2.4 and Fig 2.4 shows a scheme of the spectrograph.

In 2003, a new mode of operation involving multi-object spectroscopy was implemented. Eight fibers (input diameter 1 arcsec) coming from the fibre positioner of FLAMES, the instrument mounted at the opposite Nasmyth platform, can feed the red arm of the UVES spectrograph.

UVES consists of two main parts: the first part is mounted on the rotator (which remains stationary while the telescope adapter rotates to follow the field rotation). It includes the calibration system, a removable iodine cell, a slide with image slicers and an optical derotator which is permanently installed in the beam. The second part, the two arms cross-dispersed echelle spectrograph, is mounted on a steel table fixed to the floor of the Nasmyth platform and is covered by a light-tight enclosure which also provides thermal insulation and protection from dust. The light beam from the telescope is focused on the red arm entrance slit or is directed to the blue arm slit by a mirror. On the fixed table in the pre-slit area, additional optical components are available for insertion in the optical beam: filters, a depolarizer, an Atmospheric Dispersion Compensator (ADC) and two pupil stops of different size. Two dichroics are available to work in parallel with the two arms. The blue arm (300-500 nm) and the red arm (420-1100 nm) have an identical layout. They are folded and cross each other to minimize the size of the table on the platform. The two-arm solution gives high efficiency because it permits to optimize the spectral response of coatings, gratings and detectors in each arm. With a beam of 200 mm, the off-axis parabolic collimators illuminate the echelle gratings of 214 x 840 x 125 mm with a large blaze angle (76°). The echelle R4 gratings are the largest ever made of this type. They are operated in quasi-Littrow mode, that is with the angle of incidence and diffraction equal but in a different plane, to maximize efficiency. The grating cross-dispersers provide an order separation larger than 10 arcsec at any wavelength in the spectral range 300 - 1100 nm. This separation allows to perform semi-long-slit spectroscopy of compact objects, the use of image slicers, a good sampling of sky emission at red wavelengths and the possibility of accurate inter-order background estimates. The cameras are dioptric (no central obstruction) and provide an external focal plane for easy detector interfacing and upgrading during the lifetime of the instrument, together with a large field, good image quality and high optical transmission.

The blue CCD detector format is 2048 x 4096 pixels, windowed to 2048 x 3000. In the red, a mosaic of two 4096 x 2048 pixels CCDs is offered, separated by about 1 mm (loss of one order in

the gap). The direction of the spectral dispersion (= echelle orders) is along the larger dimension of the CCDs.

Table 2.4: *UVES characteristics and observing capabilities.*

	Blue Arm	**Red Arm**
Wavelength range	300-500 nm	420-1100 nm
Resolving power-slit product	41,400	38,700
nm/pixel	0.0019 nm at 450 nm	0.0025 nm at 600 nm
Max. Resolving power	80,000	110,000
(2-pixel sampling)		
Throughput at blaze	12% at 400 nm	14% at 600 nm
(TEL+UVES, no slit, no atm.)		
Limiting magnitude	18	19.5
(90m exp. time, S/N =10,	R=58,000	R=62,000
0.7 arcsec slit,seeing 0.7)	at 360 nm	at 600 nm
CCDs	2048 4096	two 2048 4096
	(windowed to 2048 3000)	(mosaic of different types)
Pixel (15μm) scale		
disp. dir. (varying along order)	0.215 $\pm$ 20%	0.155 $\pm$ 20%
along slit (dep. on cross-disp.)	0.25"(CD1 and CD2)	0.18"(CD3),0.17 (CD4)
Echelle	41.59 g/mm	31.6 g/mm
(R4 mosaic)		
Cross dispersers	CD1: 1000 g/mm	CD3: 600 g/mm
Blaze wavelength	430 nm	560 nm
	CD2: 660 g/mm	CD4: 312 g/mm
Blaze wavelength	460 nm	770 nm
Typ. wavel. cov. CD1 and CD3	85 (126) nm	200 (403) nm
(CD2 and CD4 in parenthesis)	in 33 (31) orders	in 37 (33) orders
Min. order separation	10 arcsec	9 arcsec
(standard setup)	(40 pixels)	(51 pixels)

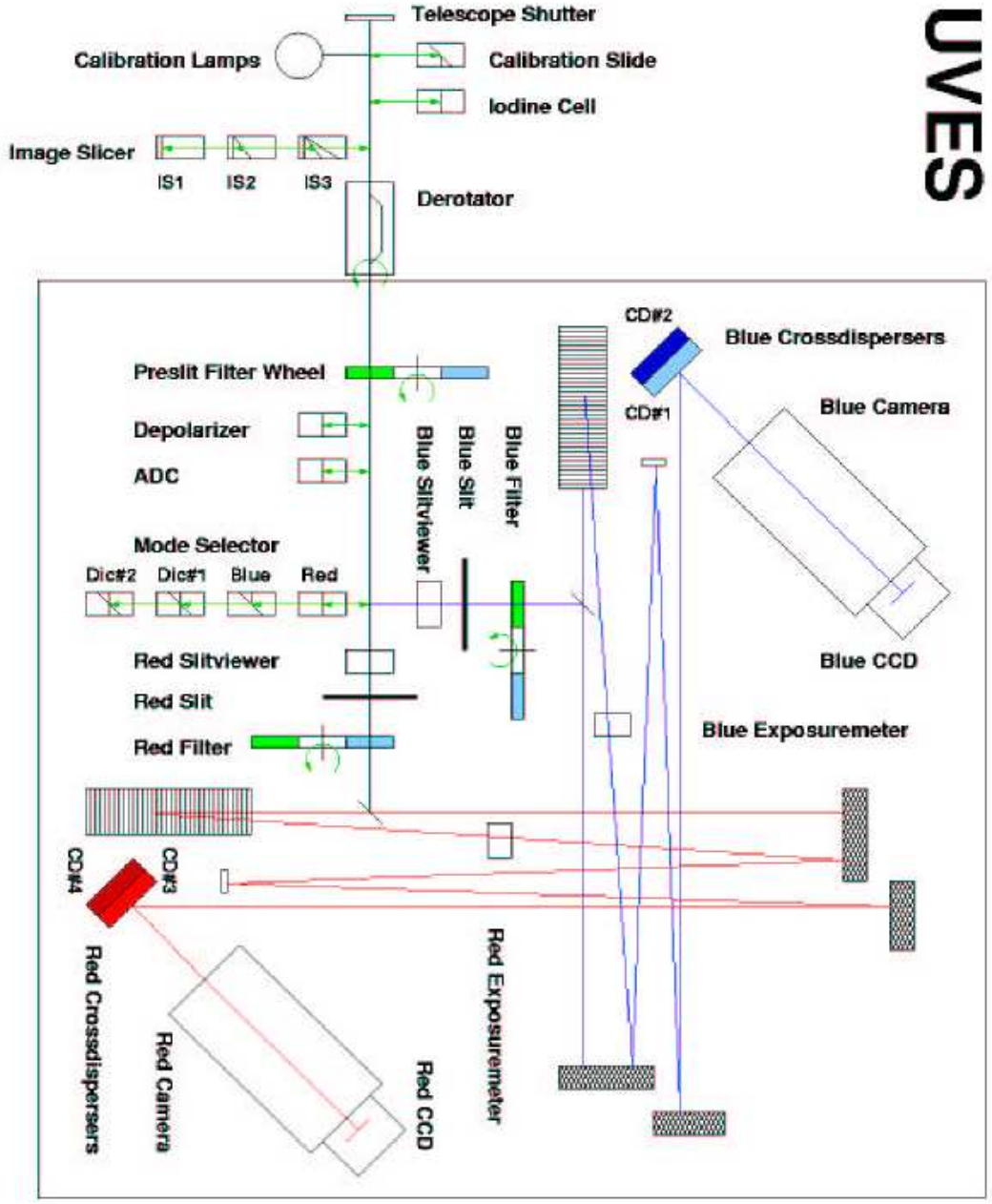

Figure 2.4: *Schematic overview of the UVES spectrograph.*

Chapter 3

Methodology

3.1 Overview of the analysis of stellar spectra

Following Alloin (in "Astrophysical & laboratory spectroscopy", 1988), Kaler ("Stars and their spectra", 1989), Gray ("The observation and analysis of stellar photospheres", 1992), Jaschek & Jaschek ("The behaviour of chemical elements in stars", 1995) and Emerson ("Interpreting astronomical spectra", 1996), we will give a brief general overview about stellar spectra and their analysis.

The stellar spectra are typically absorption spectra. A star can be described as a layered body, characterised by different physical conditions (pressure, temperature, density) in the different layers, and its resulting spectrum is the combination of the radiation emerging from its different parts. The deep layers are gases under high pressure and they produce a continuum spectrum, going outwards through the external layers (called atmosphere) the pressure and the density drop and the radiation is absorbed by the atoms of the atmosphere gas. However this picture is a rough simplification, in reality, the pressure drops slowly in the outward direction and the layers overlap, gradually merging one into another.

Each line actually is formed at a somewhat different depth in the stellar atmosphere. For example, lines of ions must be produced in layers that are deeper than those that generate neutral features, as higher temperatures are required to strip electrons from atoms through collisions.

The interpretation of a stellar spectrum consists of deriving from the observed quantities (shape of the continuum, intensity and profile of the lines) the physical parameters which describe the stellar atmosphere: its dynamical and thermodynamical state and its chemical composition. Historically, the first studies and classifications of stellar spectra have been done from an observational point of view, starting from the spectrum of the Sun in the early 1800s. The rapidly improving instrumentation and the increasing number of studied stars changed the classification of stellar spectra through the decades. At the beginning, it was based only on the colour of the stars and the presence of particular lines (the Harvard classes: OBAFGKM), then it became a two-dimensional classification adopting also luminosity classes (from luminous supergiants Ia to white dwarfs VII). In Fig 3.1 are shown examples of spectra of well-studied stars with their spectral class. The changes

through the spectral sequence from hot stars (B) to cool stars (M) are quite evident. Figure 3.2 displays the average locations of stars of the various luminosity classes in the Hertzsprung-Russell diagram, obtained using the absolute visual magnitude vs the spectral type.

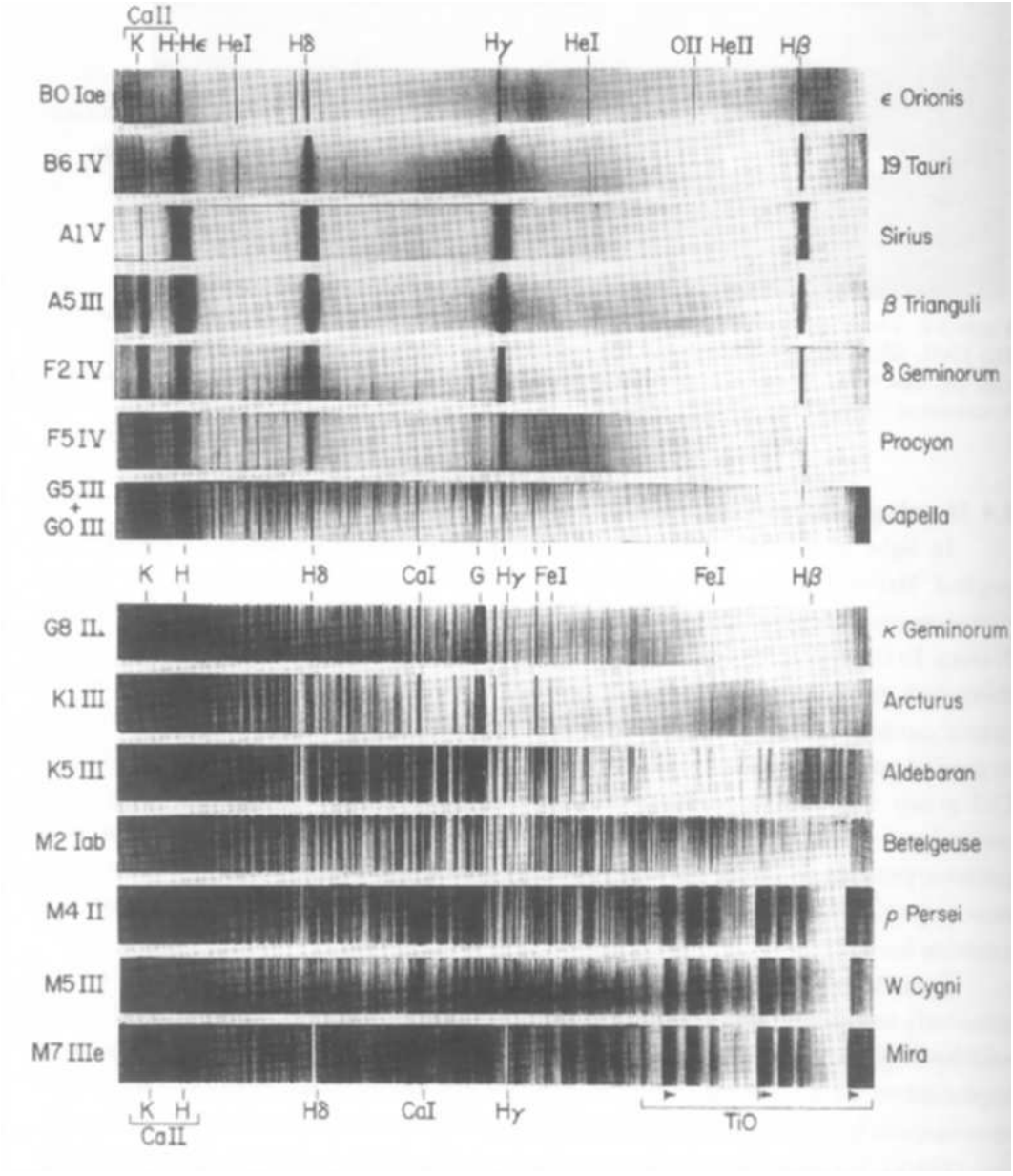

Figure 3.1: *The spectral sequence is illustrated with representative stellar spectra in the blue and violet region. Hydrogen, calcium, iron and oxygen lines are indicated. The cool M stars spectra show also the violet edges of molecular TiO bands (from Kaler 1989).*

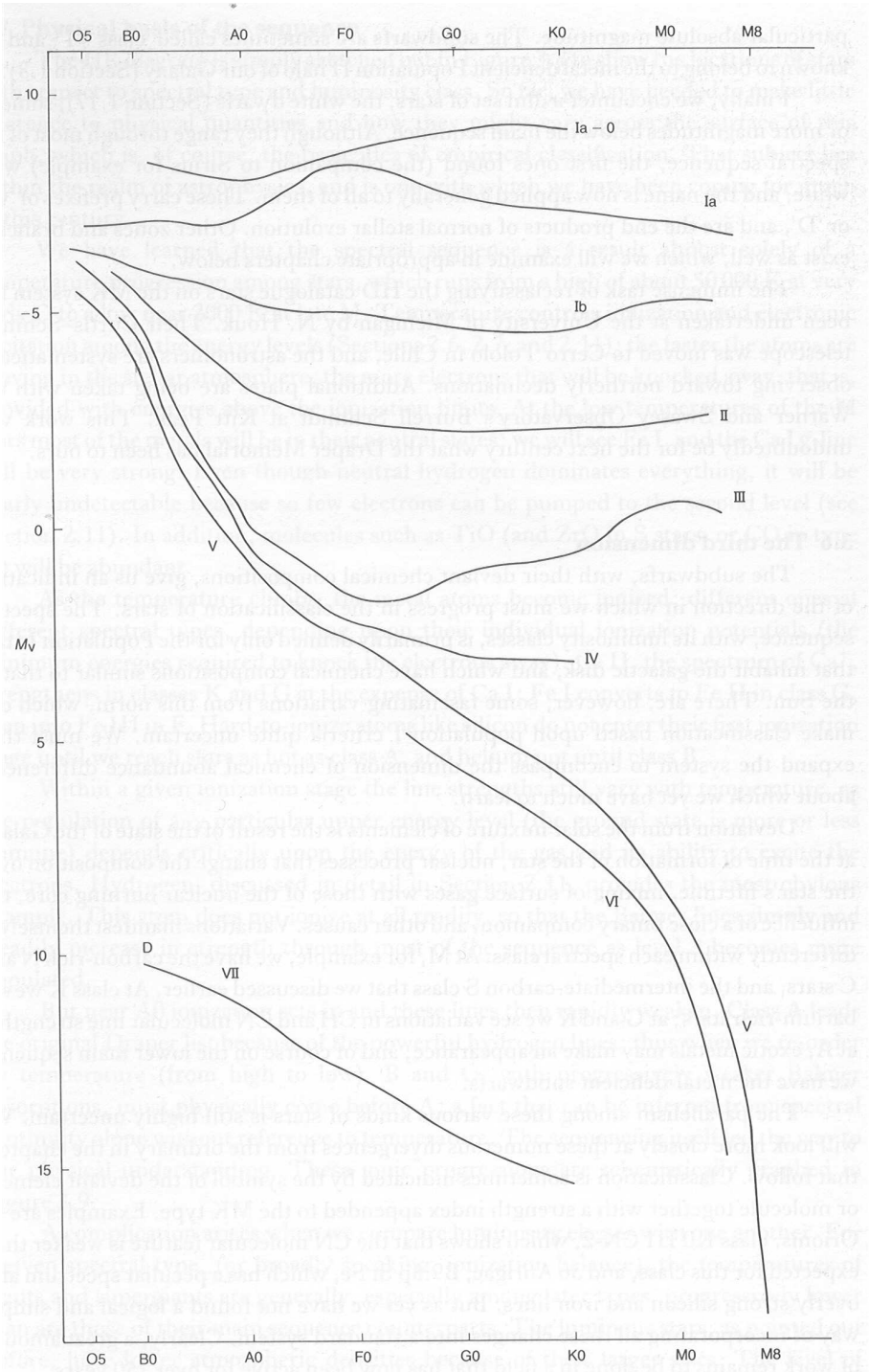

Figure 3.8.

Figure 3.2: *The Hertzsprung-Russell diagram with the average locations of the stars of the various luminosity classes. The y-axis is the absolute visual magnitude while the x-axis is the spectral type. The stars actually occupy broad bands centered on the solid lines. The supergiant (Ia-Ib) and giant (II-III) zones are especially broad (Figure 3.8 from Kaler 1989). Cepheids belong to a range of spectral classes from F to K*

Cepheids belong to a range of spectral classes from F to K. Being variable stars their colour (i.e. temperature) varies with the phase, so their spectral type will be different depending on when the stars are observed. Their luminosity class is between Ia (luminous supergiants) and II (bright giants). Figure 3.3 shows three Galactic Cepheids of our sample characterised by different temperatures (4705 K, 5555 K and 6130 K) but with a similar metallicity. It can be seen the decrease of the intensity of the lines as the temperature increases. The luminosity and the temperature of a Cepheid vary along the pulsational cycle so the intensity of its spectral lines change with the phase. Number and intensity of the spectral lines depend also on the chemical composition of the variable.

The physical origin of a stellar spectrum has been unravelled in the first part of the twentieth century, when the equations relating ionisation and excitation to temperature and density have been derived and solved. From that time on a whole body of work has been done to describe and reveal the nature of a stellar spectrum from a theoretical point of view, with the development of models of the stellar atmospheres. The modern analysis of a stellar spectrum uses a reverse approach compared to the empirical classification mentioned above. First it is necessary to build a stellar atmosphere model and predict values for the observable quantities and, secondly, to compare these values with real observations and readjust the physical parameters of the model to match the observations.

The intensity or strength of a line can be characterised by the so-called equivalent width (see Fig 3.4). The equivalent width of a line (W) is defined as the surface enclosed in the line profile:

$$W \equiv \int_{\lambda_1}^{\lambda_2} \frac{I_c - I_l}{I_c} d\lambda \tag{3.1}$$

where I_c is the continuum intensity and I_l is the line intensity at every λ between λ_1 and λ_2 (the limits of the line). In other words the equivalent width is the measure of the flux of the line in units of the density of the flux of the continuum. If we assume the continuum background as unity, it is the width of a rectangle with height 1. The abscissa in Fig 3.4 can be expressed either in terms of wavelength or on a frequency scale. The equivalent width is given in the same units as the abscissa and can thus be expressed in Å or cm^{-1}. The difficulties in measuring equivalent widths usually come from the tracing of the continuum, because of line crowding (typical of late type stars) or of superpositioning of neighbouring lines (rapid rotating or pulsating stars). Also, it can be problematic to recover the true continuum measuring lines in the vicinity of a strong line with broad wings.

As we shall see, the W of a line is linked to the abundance of that element and this is one of the way to determine the elemental abundance of a star from its spectrum. An alternative technique is the spectral synthesis (discussed in more details in section 3.6), particularly useful in case of severe line blending.

The strength or equivalent width of a line in a stellar spectrum depends on the chemical abundance, the temperature, the absorption coefficient, the number of absorbers and atomic constants. The change in the line profile and equivalent width is not a simple proportionality, but depends on the optical depth of the line. In Fig 3.5 we see an example of the theoretical behaviour of the

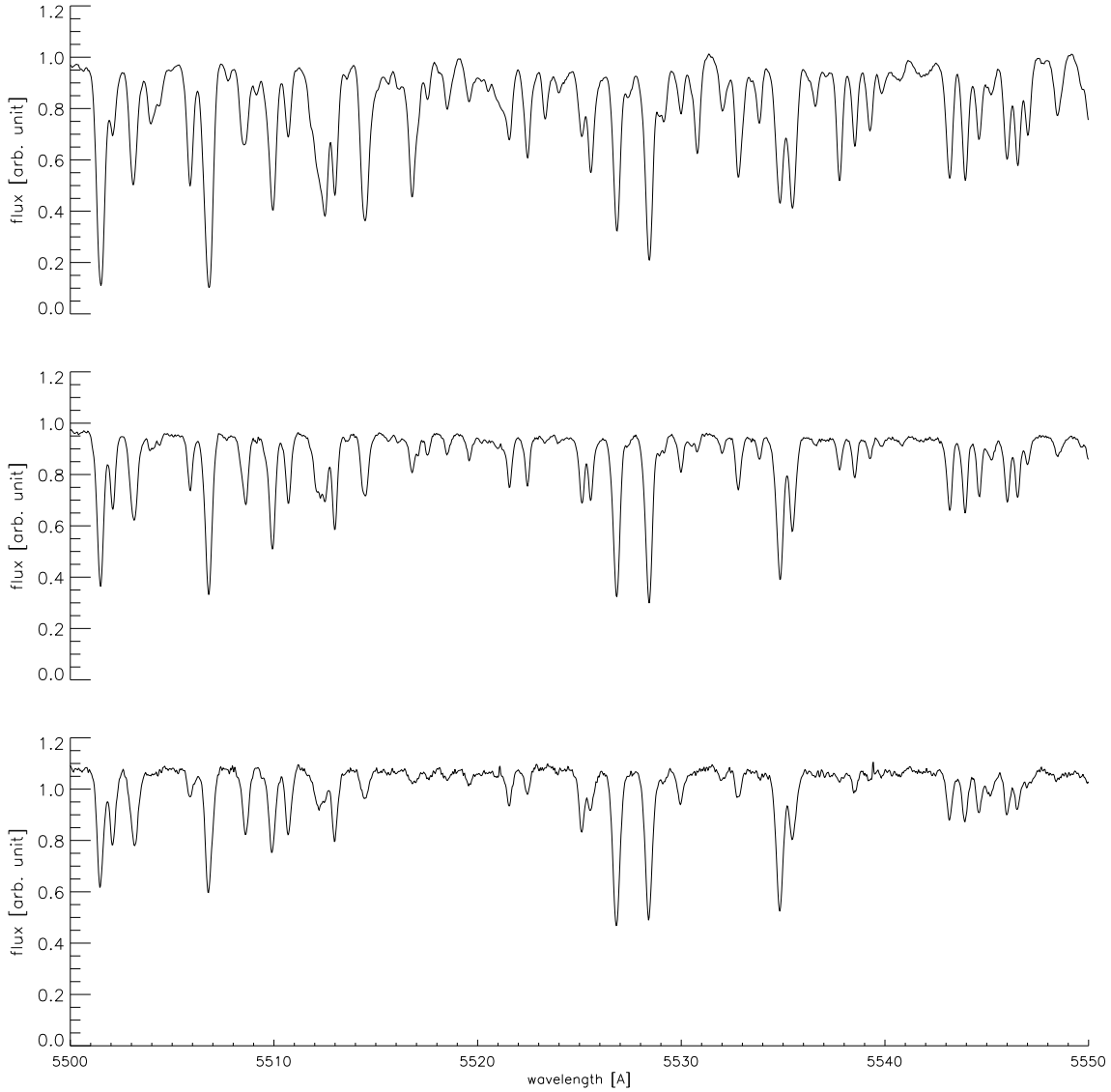

Figure 3.3: *The same spectral range as observed in three Galactic Cepheids (with a solar metallicity) of our sample characterised by different temperatures top: 4705 K, middle: 5555 K, bottom: 6130 K. The intensity of the lines decreases as the temperature increases.*

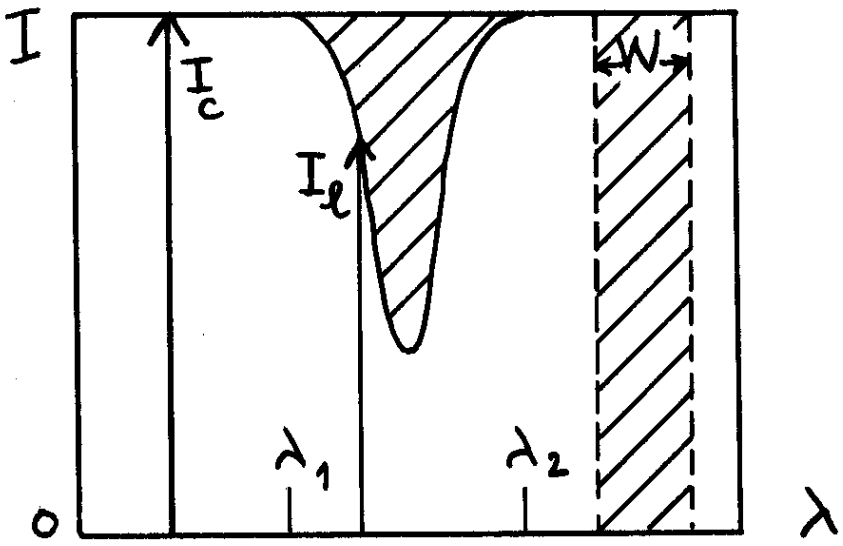

Figure 3.4: *Definition of the equivalent width W. I_c is the continuum intensity and I_l is the line intensity at every λ between λ_1 and λ_2 (from Alloin 1988).*

profile and equivalent width of an iron I line, the top panel shows the so-called curve of growth, which, typically, is a log-log plot of equivalent width (W) versus abundance (A). The line strength increases with an increase in the chemical abundance and we can distinguish three different phases of the line growth. For weak lines, the depth and the equivalent width of the line is proportional to A. The second phase is entered as the central depth approaches the maximum value and the line saturates. The saturation grows asymptotically towards a constant value. The third stage of the behaviour starts as the optical depth in the line wings becomes significant compared to ratio of the line absorbers to the continuum opacity. At this stage the equivalent width will grow approximately proportional to $A^{1/2}$. Thus, to determine the elemental abundance is crucial to accurately measure equivalent widths of weak lines, in order to remain in the first phase of the line growth, where there is a direct proportionality between W and A.

The behaviour of this part of the curve of growth is described by the following expression (from Gray, 1992):

$$\log\left(\frac{W}{\lambda}\right) = const + \log A + \log gf\lambda - \Theta_x\chi - \log k_\nu \tag{3.2}$$

where A is the chemical abundance, $\Theta_x = 5040/T$ (where T is the temperature), χ is the excitation potential for the atomic level, gf is the oscillator strength (related to the atomic transition probability and different for each atomic level), k_ν is the ratio of the line absorbers to the continuum opacity and the absorption coefficient is lumped in the constant.

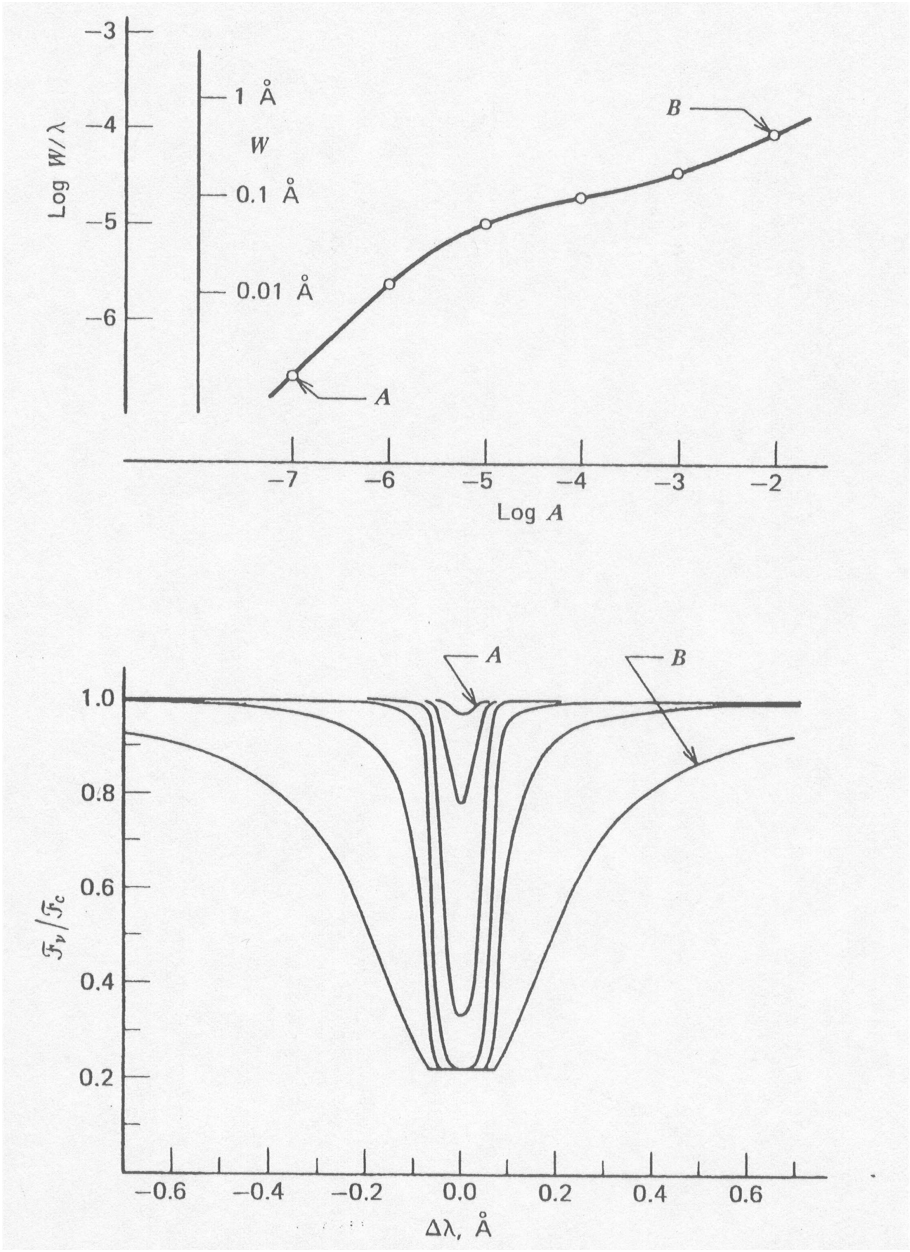

Figure 3.5: *Both the equivalent width (top) and the profile (bottom) change with the chemical abundance of the absorbing species. The circles on the curve of growth correspond to the profiles below (Fig.13.12 from Gray, 1992).*

k_ν depends on the electron pressure that, in turn, is controlled by the surface gravity. On the other hand, the absorption coefficient is a function of the thermal and microturbulent velocities, the latter is a small-scale non-thermal velocity that parametrise the spectral line broadening (see Gray, 1992, chapters 13, 14 and 18 for an in-depth discussion of the above mentioned quantities and their derivation). Thus, the equivalent width and the chemical abundance are then related to the stellar parameters (temperature, gravity and microturbulent velocity), which are also used to characterise a model atmosphere. Knowing these parameters and the physical characteristic of the line of interest and its equivalent width, it is then possible to calculate the correspondent elemental abundance using Eq. 3.2.

Equation 3.2 also tell us that, for a given star, curves of growth for lines of the same species, where A is constant, will differ only in the displacements along the abscissa according to their individual values of $gf\lambda$, χ and k_ν. From the model atmosphere point of view, we can choose a line (it has a fixed $gf\lambda$ and χ and the model fixes Θ_x and k_ν) and vary the equivalent width to generate its curve of growth. In this way it is also possible to investigate how changes in the temperature, in the gravity or in the microturbulent velocity can affect the chemical composition (see chapter 4 for an analysis on the iron abundances).

A few more words must be added on the general subject of chemical composition. The quantity normally derived from observations of stellar spectra is the number of atoms of some elements as a fraction of the number of atoms of hydrogen. Abundances are expressed relative to hydrogen because in the vast majority of the stars hydrogen atoms are close to 90% of all atoms, and spectral lines are measured relative to the continuum, whose intensity is usually directly or indirectly related to the hydrogen abundance. The total abundance of all the elements heavier than helium relative to hydrogen does vary considerably between stars. This quantity is sometimes called *metallicity* because lines of iron are often the easiest to detect in faint stars. The metallicity or the iron abundance, like all the other elements, is commonly quoted relative to its value in the Sun. The terminology commonly employed is [X/H], where X generally indicates a chemical element, which means $\log(N_X/N_H)_{star} - \log(N_X/N_H)_\odot$. Usually stars with a low (negative) value of this quantity are described as being *metal poor*, while stars with a high (positive) value are called *metal rich*. It is important to stress that all these observed abundances refer to the surface of the star.

Below we present the methodology used to calculate the elemental abundances of our sample of Cepheids: assembling the line lists, determining the equivalent widths and the atmospheric parameters and computing the abundance with the adopted model atmospheres. The spectrum synthesis is also discussed as an alternative method for abundance determination.

3.2 Line lists

A crucial step of any spectral analysis in order to derive elemental abundances is a careful assembling of a line list. It is fundamental to select unblended lines to prevent undesirable contribution from other elements that can affect the determination of the abundance, making them larger than they should be. As a starting point, we have assembled two line lists (FeI-II and α-elements[a]) choosing

[a]Light elements with an even atomic number: C, O, Mg, Si, S, Ar, Ca, Ti

lines used in previous studies on Cepheids and RR Lyrae from Clementini et al (1995), Fry & Carney (1997, hereafter FC97), Kiss & Vinko (2000) and Andrievsky et al (2002a) plus a selection of iron lines from VALD (Vienna Atomic Line Database; Kupka et al 1999). The Vienna Atomic Line Database is a critical collection of atomic line parameters of astronomical interest and provides tools for selecting subsets of lines for typical astrophysical applications (line identification, chemical composition and radial velocity measurements, model atmosphere calculations, etc). The VALD lines have been selected for effective temperatures typical of Cepheid stars (4500-6500 K).

We have, then, visually inspected each line on the observed spectra, in order to check their profile and to avoid blended lines. In order to do so, we have searched the VALD database for all the existing lines between 4800 and 7900 Å on stellar spectra characterised by stellar parameters typical of Cepheids (T_{eff}=4500 K, 5500 K and 6500 K, log g=2 and v_t=3 km/s). We then overplotted all the lines found in VALD, that fall within ±3 Å from each of our selected lines, and checked for their possible contribution to the equivalent width of our selected line (an example is shown in Fig. 3.6). This test was carried out on 3 different observed spectra, characterised by effective temperatures (as found in the literature from previous analyses) close to 4500 K, 5500 K and 6500 K, respectively. Any contribution larger than 5% of the line strength made us discarding the line under scrutiny. There remains, of course, the possibility that some lines could be missing in the VALD compilation, but these should be only weak lines, whose contribution would then be negligible.

Our final lists includes 246 FeI lines, 17 FeII lines, 5 OI lines, 4 NaI lines, 6 MgI lines, 4 AlI lines, 49 SiI lines, 28 CaI lines, 53 TiI lines and 18 TiII lines, spanning a spectral range from 4800 Å to 7900 Å which is the range covered by our FEROS spectra. Our UVES spectra cover a narrower spectral range for which we can use 181 FeI lines, 13 FeII lines, 2 OI lines, 2 NaI lines, 5 MgI lines, 2 AlI lines, 27 SiI lines, 22 CaI lines, 42 TiI lines and 12 TiII lines. For all the lines, we have adopted the physical properties (oscillator strengths, excitation potentials) listed in VALD. A high number of lines for each element reduces the internal errors on the final determination of the abundance.

Figure 3.7 compares the distribution of the equivalent widths of our iron lines with those from Fry & Carney (1997), in the case of the same star, the Galactic Cepheid VCen. As it can be clearly seen, our list is significantly larger and well samples the best range of equivalent widths (at around 20 mÅ as suggested by Cayrel 1988 for the determination of elemental abundances and as show at the beginning of this chapter) to obtain iron abundances.

The complete lists of lines are given in Appendix B (Table B.1 and B.2) where the four columns list respectively the wavelength, the ion identification, the excitation potential and the *gf* values of each line.

3.3 Equivalent widths

The second crucial step of our spectral analysis is the measurement of the equivalent widths (W) of the elemental lines we have assembled in our final lists. Because of their large number, we have used a semi-interactive routine developed by Dr. Patrick François: *fitline* (private communication), that greatly increases the efficiency while yelding accurate measurements (see below). This code is based on genetic algorithms, which mimic how DNA can be affected to make the evolution of species (Charbonneau 1995). It uses a Gaussian fit, which is defined by four parameters: central

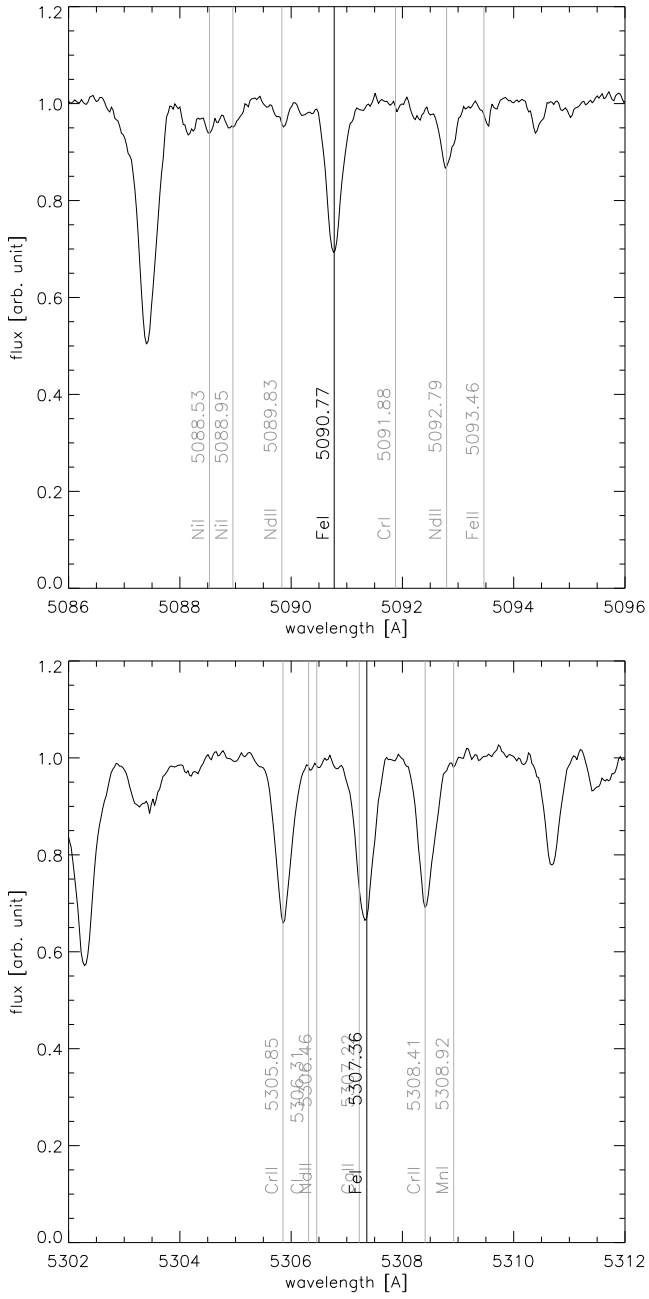

Figure 3.6: *Examples of visual inspection on the selected iron lines. The iron lines are plotted in black while the other elemental lines are plotted in gray. In the top panel it is shown an unblended line and in the bottom panel there is an examples of a blended line.*

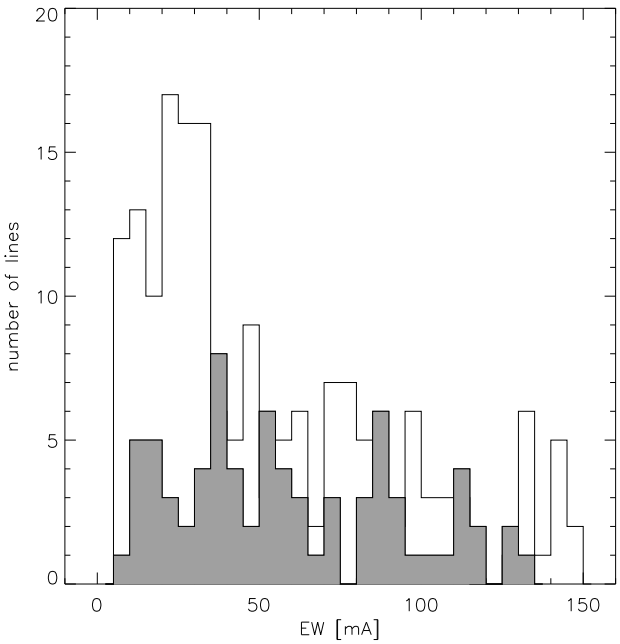

Figure 3.7: *The distributions of the equivalent widths (W) of our lines (empty histogram) and Fry & Carney's lines (1997, dark grey histogram), in the case of the same star (VCen).*

wavelength, width, depth and continuum value of the line. A top-level view of the algorithm is as follows:

1. Compute an initial set of Gaussians, picking random values of the four parameter (scaled to vary between 0 and 1) and calculate the χ^2 with the observed line for each Gaussian.
2. Compute a new set of Gaussian from the 20 best fit (fixed value) of the previous "generation" introducing random modification in the values of the parameters ("mutation").
3. Evaluate the "fitness" of the new set (χ^2 calculation for each Gaussian) and replace the old set with the new one.
4. Iterate the process (100 to 200 "generations") to get the best fit (lowest χ^2) for each observed line.

In practice, the final equivalent widths are determined in three steps: running *fitline* a first time to obtain preliminary evaluation of the equivalent widths, feeding these results to a routine that allows to inspect and interactively correct the position of the continuum for each line (visually inspecting the observed spectrum with the best fit superimposed) and, as last step, the algorithm calculates the final equivalent widths. These steps contitute a complete session of *fitline*. The necessary inputs to run this program are the 1-D spectrum of the star (in ASCII format) and the line list. The program's parameters that can be adjusted to achieve the best results are the width

of the gaussians and the tolerance range for the search of a blend. After several tests we found that the best approach was to run two sessions of *fitline*, using two different values for the width of the gaussian fitting (typically 32 and 26 pixels) and the tolerance range (typically 0.15 and 0.9 Å):

- the first session gives measures of W of the complete line list for a set of parameters, in Fig 3.8 an example of a good fit from the first session is shown (a);

- the lines that present a bad fit as output of the first session are re-measured adopting different values of the width of the gaussian, usually smaller, and the tolerance range, usually bigger. In this way, during the interactive process, it is easier to get a better fit of the lines of interest using the program feature for the measure of blended lines. Fig 3.8 shows example of a bad fit from the first session (b) and a good fit from the second session adopting a smaller width and a bigger tolerance range (c).

All the UVES spectra have been smoothed to improve the quality of the Gaussian fit (smooth_step = 11 pix using *splot* task in IRAF, corresponding to 0.16 Å for the first CCD and 0.19 Å for the second).

For about 15% of the lines, the Gaussian profile adopted by *fitline* could not satisfactorily reproduce the observed profile (see Fig 3.8, panel (d)). For these cases (usually very broad or asymmetric lines), the equivalent widths were measured manually with the IRAF *splot* task, using a gaussian fit again or a pixel summation. The width of fitting gaussian of this task is is not fixed, at variance with fitline, then it is possible to improve the fitting of a single line. The mean difference, as computed for those lines for which both methods could be applied, is around 1.5 mÅ comparable to the average error on the W inferred from the quality of the data (Equation 7, Cayrel 1988). We can then safely use all our W measurements, independently of the method followed to derive them.

For the determination of the elemental abundances, we have selected only lines with equivalent widths between 5 and 150 mÅ, this range allows the use of a large number of lines in the linear portion of the curve of growth, reducing the internal error on the final abundance. The lower limit was chosen to be a fair compromise between the spectral characteristics and the need for weak lines for an optimal abundance determination. The upper limit was selected in order to avoid the saturated portion of the curve of growth. We note that for T Mon, SZ Tau and KQ Sco an upper limit of 200 mÅ was chosen because these stars have broad and strong lines. In this way the number of selected lines is similar to the one used for the rest of the sample. We note that this higher upper limit does not have any effect on the final metallicities of the three stars, we have tested that the differences between the iron abundances obtained with the two set of Ws (with limit at 150 mÅ and at 200 mÅ) are within the errors.

Considering the mean difference on the W obtained with *fitline* and *splot* and the uncertainty in the continuum placement from two measurements of the W (carried out independently by the author and Dr Francesca Primas) we assume ±3 mÅ as error on the measured equivalent widths for the lines below 100 mÅ and ±5 mÅ for the stronger features.

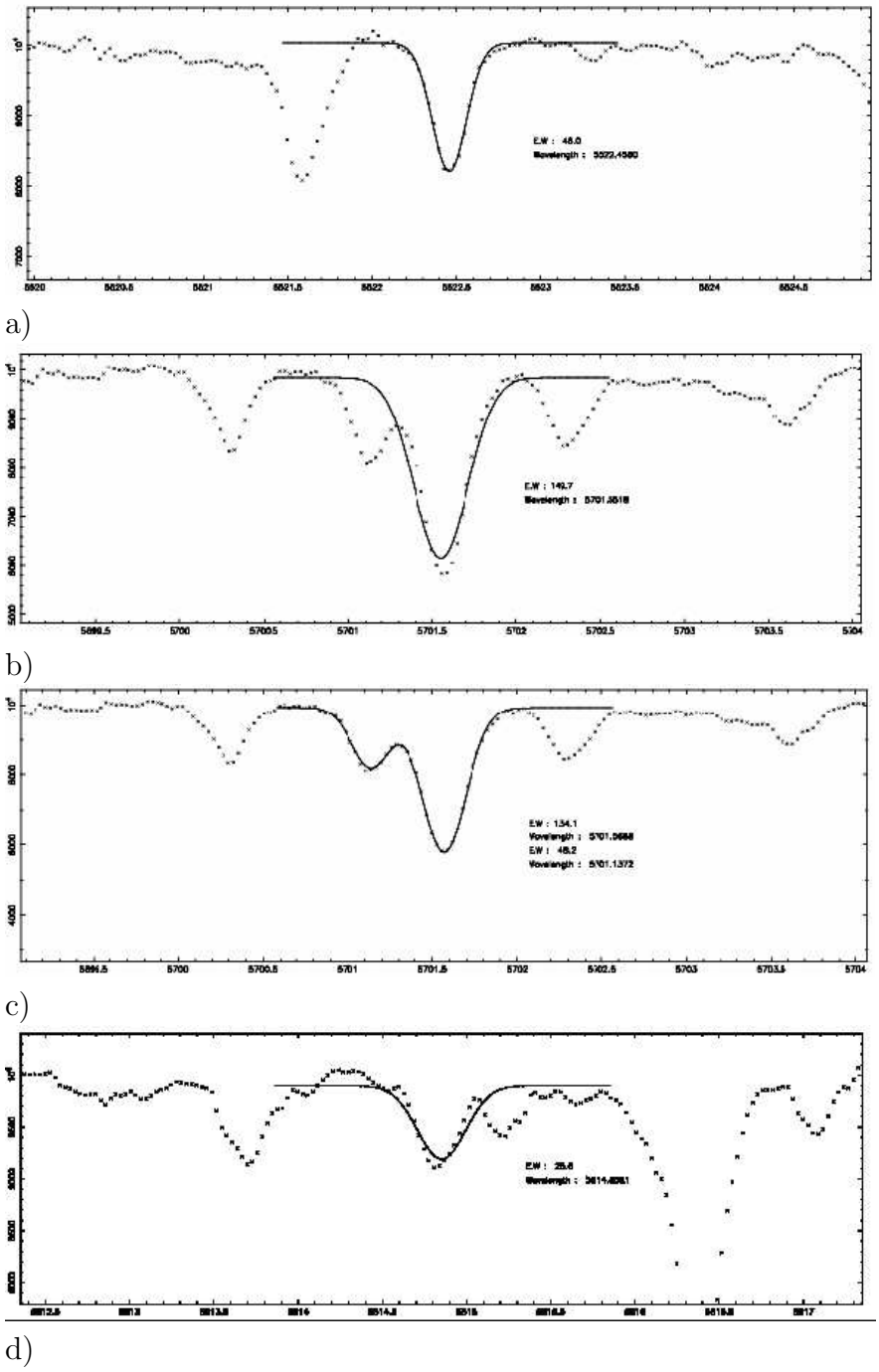

Figure 3.8: *Examples of measurements of equivalent widths with* fitline. *Panel (a) shows a good fit from the first* fitline *session, panel (b) a bad fit from the first* fitline *session, panel (c) a good fit from the second* fitline *session and panel (d) a bad fit from the second* fitline *session.*

3.4 Stellar parameters

The stellar parameters (effective temperature, gravity and microturbulent velocity) were derived spectroscopically. We have determined the stellar effective temperature $T_{\rm eff}$ by using the line depth ratios method described in Kovtyukh & Gorlova (2000). It is based on weak neutral metal lines (in our case, less than 100 mÅ in equivalent width in order to exclude line-broadening effects) with low excitation potentials, selected to obtain as close as possible pairs in wavelength space. The depth ratios of these lines are very sensitive to the effective temperature, thus they can used as temperature indicators. The application of this method is rather simple, it consists in measuring the depths of the lines selected by Kovtyukh & Gorlova (32 pairs), determining their ratios and calculating the $T_{\rm eff}$ using this relation:

$$T_{\rm eff} = a + b \cdot r + c \cdot r^2 + d \cdot r^3 \tag{3.3}$$

where r is the line depth ratio, a, b, c and d are the coefficients of the calibration for each pair. The final effective temperature is the mean value of the outcomes from each pair of lines.

The calibration of this method has been done using FC97 scale of temperatures. The line depth ratios have the advantage of being independent of interstellar reddening and metallicity effects, uncertainties that instead plague other methods like the integrated flux method or colors calibrations (Gray 1994). As a sanity check on our spectroscopic method, we have analysed 5 individual spectra of Galactic Cepheid AP Puppis taken at different phases along the pulsational period (ϕ=0.11 (observed twice), 0.31, 0.51, 0.91). Four out of these five spectra have been collected in an independent observational campaign led by Drs. Giuseppe Bono and Patrick François, who kindly let us use their spectra for this test. In Figure 3.9 are shown the effective temperatures derived for the five phases of AP Pup (filled squares) in comparison with the behaviour computed by Pel (1978) from Walraven photometry. The agreement is indeed very good.

The final number of temperature indicators we have used for the Galactic Cepheids is between 26 and 32, depending on the star, whereas for the Magellanic Cepheids we have measured between 20 and 28 ratios. From this method, we have obtained effective temperatures with an accuracy of about 40 K for the Galactic Cepheids and 50 K for the Magellanic ones (errors on the mean).

Microturbulent velocity (v_t) and gravity ($\log g$) were constrained by minimizing the log([Fe/H]) vs W slope (using the FeI abundance) and by imposing the ionisation balance, respectively. These two procedures are connected and require an iterative process (on average, between 5 and 7 iterations, depending on the star). We first achieved the minimization of the log([Fe/H]) vs W slope and, in a second time, the ionisation balance. We assumed the ionisation balance fulfilled when the difference between [FeI/H] and [FeII/H] is less than the standard error on [FeII/H] (typically $\sim$0.07 dex). This condition is usually satisfied by a set of values of $\log g$, the range of which was assumed to be our error on $\log g$. The final value of the gravity, i.e. the "best" ionisation balance, corresponds to a difference between [FeI/H] and [FeII/H] equal or less than the standard error on [FeI/H] (typically $\sim$0.02 dex). We note that this second condition cannot be fulfilled for 13 stars (5 Galactic, 3 LMC and 5 SMC Cepheids), for which we then assumed as "best" ionisation balance (and corresponding gravity) the one with the smallest difference between [FeI/H] and [FeII/H].

As first guess for the microturbulent velocity and the gravity, we adopted values typical of

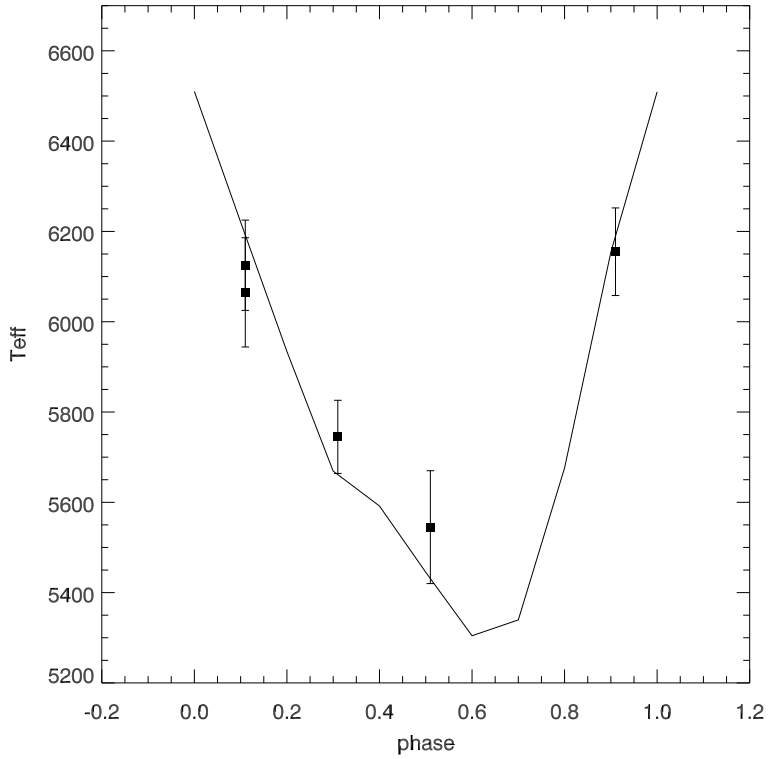

Figure 3.9: *Comparison between the behaviour of the effective temperature of the Galactic Cepheid AP Puppis found by Pel (1978, solid line) and our results using the line depth ratios method for 5 phases (filled squares) with their associate errorbars.*

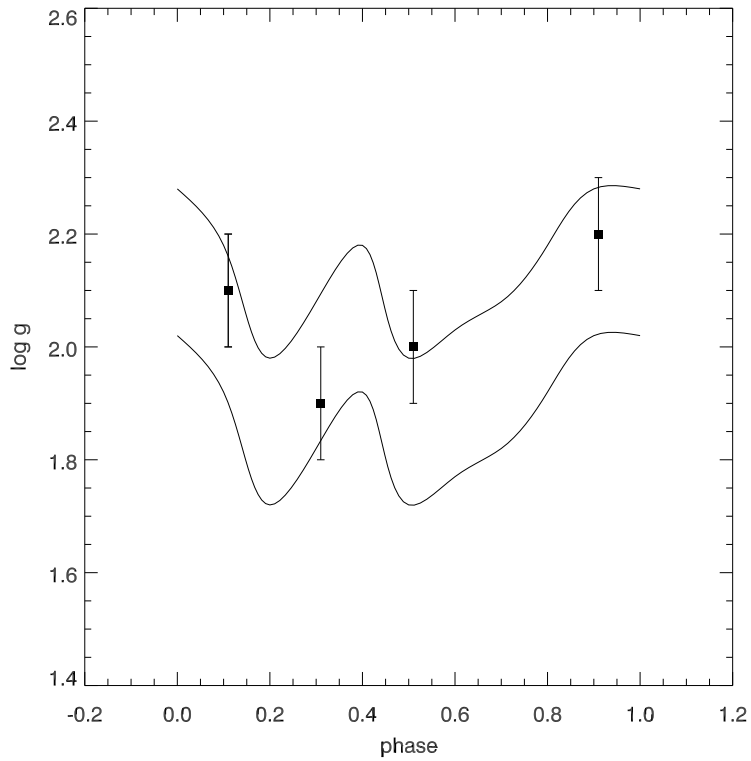

Figure 3.10: *Comparison between the behaviour of the gravity of the Galactic Cepheid AP Puppis found by Pel (1978, the two solid lines indicate the upper and lower limits) and our results for 5 phases (filled squares) with their associate errorbars. At ϕ=0.11, we have obtained the same value from the analysis of the two spectra.*

Cepheids (v_t= 3 km/s, $\log g = 2$) as inferred from previous studies (mainly FC97 and Andrievsky et al 2002a, 2002b). From the several iterations we have run, we have estimated errors in v_t to be 0.1 km/s and in $\log g$ to be 0.10 dex.

Our $\log g$ values for the five phases of AP Puppis follow well the trend found by Pel (1978), as it can be seen in Fig 3.10. At ϕ=0.11, we have obtained the same value from the analysis of the two spectra.

We note that for two stars (HV 2827 and HV 11211) we had to increase their temperatures, as determined from the line depth ratios, to fulfil our constrain for a good ionisation balance. This happened because we have used, in the iterative process, different values of $\log g$ down to the lowest value available in the grid of model atmospheres without a satisfactory result. For both stars the effective temperature has been increased by 50 K and their gravity is lowest value mentioned above, thus the final adopted temperatures are still within the estimated error on the determination of $T_{\rm eff}$.

3.5 Model atmospheres

With equivalent widths and stellar parameters determined as described above at hand, we have derived the elemental abundances of our stars by using the Kurucz WIDTH9 code and ATLAS9 model atmospheres with the new opacity distribution functions (ODFs) computed by Castelli & Kurucz (2003). The new ODFs grids of models (available on-line at http://wwwuser.oat.ts.astro.it/castelli/grids.html), computed for different values of metallicity, are characterised by $T_{\rm eff}$ from 3500 K to 50000 K and $\log g$ from 0.0 dex to 5.0 dex (respectively in step of 250 K and 0.5 dex). For all the values of metallicity the grids of models have also been derived with an enhancement of +0.4 dex over the solar values of the α elements (O, Ne, Mg, Si, S, Ar, Ca, Ti) abundances.

The final abundances are closely connected to the determination of the microturbulent velocity and the gravity that needs, as mentioned above, an iterative process. The v_t and $\log g$ of the model atmosphere are changed at each iteration in order to achieve the best value of the two quantities and the elemental abundance.

The new ATLAS9 models are computed using new ODFs based on the Grevesse & Sauval (1998) solar abundance, at variance with both Kurucz (1993) and Castelli (Castelli et al 1997) models computed using Kurucz's (1990) ODFs, which are based on the solar abundances from Anders & Grevesse (1989). Analogously to Castelli models, the new ODFs models are calculated without the overshooting approximation implemented in the Kurucz models.

The detailed description of the atmospheric models and their computation with ATLAS9 code is beyond the scope of this work and we only briefly summarised their characteristics below. The ATLAS9 model stellar atmospheres have been calculated in radiative and convective equilibrium for the complete range of stellar temperatures (Local Thermodynamical Equilibrium), using the following approximations: plane-parallel, horizontally homogeneous, steady-state, non-moving atmospheres with energy and abundances constant with depth. The convection theory used to calculate these model atmospheres is the local mixing-length theory (thoroughly described in Kurucz 1970) with some modifications related to the optical thickness of the convective elements and the horizontal

averaging of the opacity (see Lester et al 1982 for an in-depth discussion). The approximate overshooting introduced in the Kurucz 1993 models, with its advantages and drawbacks, is thoroughly discussed by Castelli et al (1997).

We have used a grid of models characterised by a solar metallicity for the Galactic and LMC Cepheids and a grid characterised by [Fe/H]=−1.0 dex and enhanced α elements abundances (+0.4 dex) for the SMC Cepheids. We chose these grids because they are closer to the average values of metallicity of these galaxies, which are about solar,1/3 solar and 1/5 solar. The grids of models have been interpolated to obtain the effective temperature computed for each star with the line depth ratio method and steps of 0.10 dex for the logarithm of the gravity.

We extensively tested grids of models with different chemical composition computing iron abundances of some stars for each galaxies to check possible major differences, especially for MC Cepheids (see Table 3.1).

With respect to the LMC Cepheids we tested the model atmospheres characterised by [Fe/H]=−0.5 dex with and without the enhanced α elements abundances and we can conclude that there is a really small difference in the iron abundances ($\sim$ 0.01-0.02 dex) with the ones computed with the models at solar metallicity (with and without α enhancement).

With respect to the SMC we found virtually no difference in the iron content whether one uses the models at [Fe/H]=−1.0 dex with or without the enhanced α elements abundances. Analogously to the conclusion we have drawn for the LMC, we obtained a very small difference ($\sim$ 0.01/0.02 dex) in the iron abundances computed with the model atmospheres characterised by [Fe/H]=−0.5 dexand [Fe/H]=−1.0 dex, with and without α enhancement.

A comparison between model atmospheres with new ODFs and old ODFs (Castelli models) also shows small differences in the computed iron abundances: $\sim$ 0.01-0.03.

As last test, we checked the effect of the overshooting approximation using the old ODFs Kurucz models computed, finding that the differences in the abundances with old ODFs models without overshooting, on average, are around 0.05 dex for Galactic and SMC Cepheids and around 0.06 dex for LMC Cepheids.

We conclude that the results from the different classes of models agree within the errors.

3.6 Spectrum synthesis

An alternative method to determine elemental abundances is offered by the spectrum synthesis technique. It uses the model atmosphere to predict a whole stretch of spectrum (synthesis of the line profiles of the region of interest). It is the only method that can be applied when line blending is severe. The technique works best when all the spectral lines of the region of interest can be identified and have know physical parameters. This technique is basically a trial-and-error method in which the abundances and the line-broadening parameters are arbitrarily adjusted until the shape of the observed spectrum is reproduced. The drawbacks of this method are the following: the analysis of a large sample of lines is time consuming (calculation of synthetic profiles over a wide range in wavelenghts need a large amount of CPU time), to obtain accurate results detailed information also on the spectral lines in the vicinity of the line of interest are need and this cannot

Table 3.1: *Summary of the tests with different kind of model atmospheres. In column 2, 3 and 4 are listed the differences between the grids of model without and with the α-elements enhancement. In the last column are listed the differences between the grids of model computed with the old-ODFs and the new-ODFs (solar metallicity for the Galactic and LMC stars and [Fe/H]=-1.0 for the SMC stars). For the LMC and SMC stars are also listed the differences between grids of models characterise by different metallicity.*

<table>
<tr><td></td><td>[Fe/H]=0.0</td><td>[Fe/H]=−0.5</td><td>[Fe/H]=−1.0</td><td>oldODF-newODF</td></tr>
<tr><td>Galaxy</td><td>−0.01</td><td>-</td><td>-</td><td>−0.01</td></tr>
<tr><td rowspan="2">LMC</td><td>−0.01/ − 0.02</td><td>−0.01/ − 0.03</td><td rowspan="2">-</td><td rowspan="2">−0.01/ − 0.03</td></tr>
<tr><td colspan="2">0.01/0.02</td></tr>
<tr><td rowspan="2">SMC</td><td rowspan="2">-</td><td>−0.01</td><td>−0.01</td><td rowspan="2">−0.01/ − 0.03</td></tr>
<tr><td colspan="2">0.01/0.02</td></tr>
</table>

always be achieved.

We used the *synth* routine of the MOOG code (April 2002 release, see Sneden 1973 for a general description), that is a FORTRAN code developed to perform a variety of LTE line analysis and spectrum synthesis tasks. One of the chief assets of MOOG is its ability to do on-line graphics, so it is possible to interactively change the values of the elemental abundances and the line-broadening parameters.

The *synth* routine needs as inputs a list of the lines, the observed spectrum and a model atmosphere. The line list of the region under scrutiny has to be carefully assembled to obtaine an high accuracy. Then the code calculate the synthetic profile in the region of interest and compare it with the observed spectrum. As an example, in Figure 3.11 are illustrated a set of trial synthetic spectra superimposed to an observed spectrum. This output display can be manipulated while running MOOG, to adjust the plot parameter or the smoothing of the synthetic spectra to reach the best match with the observed spectrum.

We adopt this method to determine the oxygen abundances of our sample of star (for more details see section 5.1.1).

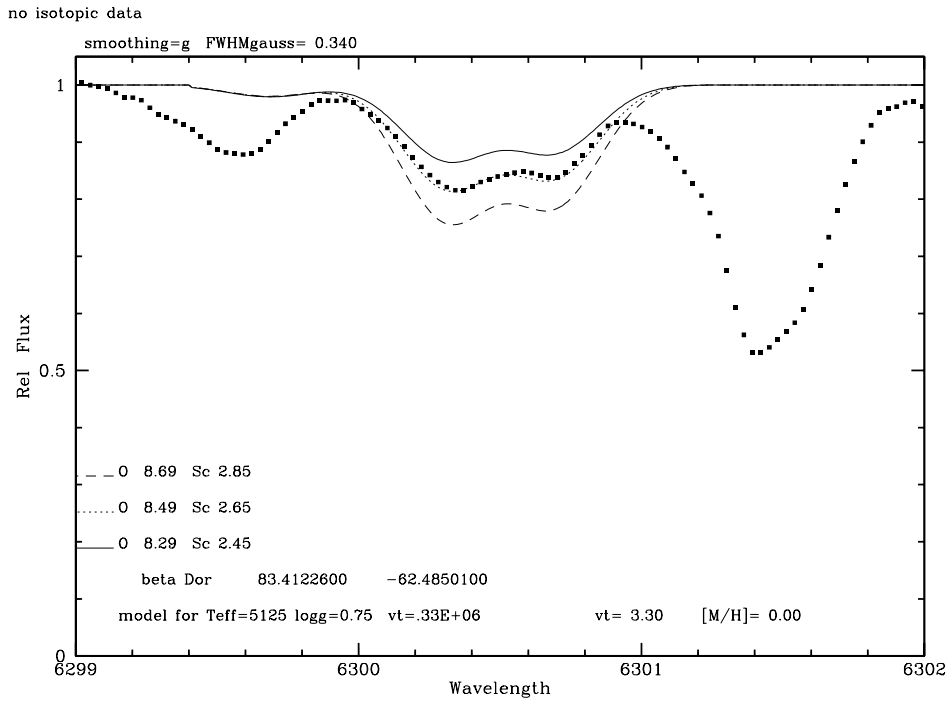

Figure 3.11: *Example of a set of synthetic spectra superimposed to an observed spectrum (filled squares) to measure the 6300 [OI] line. The abundance of oxygen and scandium on a scale where log[n(H)]=12 are indicated for each synthetic spectrum (on the left of the plot). The name of the star, its coordinates and the stellar parameters that characterise the adopted model atmosphere are also indicated (bottom of the plot).*

Chapter 4

Results: iron abundances

4.1 Abundances and their uncertainties

As already mentioned in Chapter 3, we have derived the iron abundances of our stars by using the Kurucz WIDTH9 code and the LTE model atmospheres computed by Castelli & Kurucz (2003). The FeI and Fe II abundances for each star are the mean values of the abundances obtained from each spectral line we have measured for the ion under scrutiny and falls in the useful range of equivalent widths (see section 3.3).

The outcome of the WIDTH9 code is on a scale where log[n(H)]=12, to determine the iron abundance relative to the Sun we have adopted a solar iron abundance of log[n(Fe)]=7.51 on the same scale (Grevesse & Sauval, 1998) and we have assumed our final iron content to be the FeI value. We chose FeI because the number of measured lines is significantly higher than the number of FeII lines. The FeII lines are necessary to constrain the gravity of the star (see section 3.4).

Our iron abundances, together with the adopted stellar parameters, are listed in Table 4.1 and Table 4.2 for the Galactic and Magellanic Cepheids, respectively.

For our Galactic sample, we find that the mean value of the iron content is solar (σ = 0.10, see Fig 4.1), with a range of values between -0.18 dex and $+0.25$ dex. These two extremes are represented by 3 and 1 stars, respectively (out of the 36 in total). We note that more than 50% of the stars have a sub-solar metallicity.

As we have already mentioned in Chapter 2, there are two binaries stars (KN Cen and S Mus) among our Galactic sample with a bright B dwarf as a companion. These bright companions give a contribution to the continuum level of the observed spectra but do not present any lines in the visual band (dominated by the Cepheid) since their absorption lines are in the ultra-violet region (due to their high effective temperature, $\sim$20,000 K). In order to test the effect of this contribution we have subtracted from the observed spectrum of the two binaries the estimated spectrum in the optical of the B dwarf, which presents only a continuum without any lines (as explained above), obtaining the true spectra of the two Cepheids. Then we have measured a sub-sample of iron lines to test the effect on the final abundances. In the case of KN Cen the differences of the Ws of a sub-sample of iron lines measured on the observed spectrum and the Cepheid spectrum are within

the errors, thus the final measurement of the iron content is not affected. Regarding S Mus the Ws measured on spectrum without the companion contribution are 12-15% larger than the ones measured on the observed spectrum. Thus the iron abundance of this Cepheid is ∼0.1 higher than the one we have obtained from the combined spectrum. This happens because the intensity of the lines (due only to the Cepheid contribution) compared to the continuum of the combined spectrum is, in percentage, less than the intensity of the lines compare to the continuum of the Cepheid alone. In other word the contribution of the companion makes the lines of the Cepheid weaker. We report the corrected value of the abundance of S Mus in Table 4.1.

For the LMC sample, we find that the mean value is about ~ -0.33 dex ($\sigma = 0.13$, see Fig 4.1), with a range of values between -0.62 dex and -0.10 dex. We note that one extreme represents an isolated case while 3 stars define the other one (the lowest values of the iron content in this galaxy).

For the SMC sample, we find that the mean value is about ~ -0.75 dex ($\sigma = 0.08$, see Fig 4.1), with a range of values between -0.87 and -0.63. For this galaxy the lowest value of the iron abundance is an isolated case while the other extreme is defined by 3 stars.

In Fig 4.1 are also plotted the mean iron abundances for the LMC and SMC found using F and K supergiants by Hill et al (1995) and Hill (1997), which are nonvariable stars with age and spectral type similar to Cepheids (see section 4.3). These results are in good agreement with our average values.

4.1.1 Tests on dependencies on period and stellar parameters

Figure 4.2 shows the relations between the iron content and the pulsational period (panel a), the effective temperature (panel b), the microturbulent velocity (panel c) and the logarithm of the gravity (panel d). The iron abundance does not present any trend with the stellar parameters. The [Fe/H] vs logP plot shows an apparent trend due to a selection effect in magnitude (i.e. in period), since only the brightest SMC Cepheids (i.e. with longer periods) have been chosen for our campaign. This is due to a compromise between a good quality of the spectra (i.e. good signal-to-noise), necessary to determine the elemental abundances and a reasonable observing time. The SMC Cepheids of our sample have apparent magnitudes in the V band between 12 and 15 mag, fainter Cepheids (i.e. short periods) in this galaxy reach magnitudes of 19 mag, which implies more than one night of observing time per spectrum to obtain the same signal-to-noise of our observation, this means a too burdersome observing programme in the case of a large sample of stars such ours.

We have also tested if there are correlations among the stellar parameters and between them and the pulsational period (see Fig. 4.3). The microturbulent velocity does not show any trend with the effective temperature, with the period and the gravity (Fig. 4.3 panel a, b and c, respectively). These last two results are at variance with what has been found by Fry (1997, PhD thesis) for her sample of 23 Galactic Cepheids (dashed lines). Figure 4.3 panel d shows our spectroscopic gravities against the pulsational period, compared also with the Fernie (1995) relation. Fernie calibrated a period-gravity relation for variable stars. He used a $\log g$ determination from published photometry and spectroscopy of Cepheids, RR Lyraes, SX Phe stars, δ Sct, BL Her and W Vir stars, and Mira to derive an empirical relation for all radially pulsating variables. We can see that our results follow fairly well the trend of Fernie's relation.

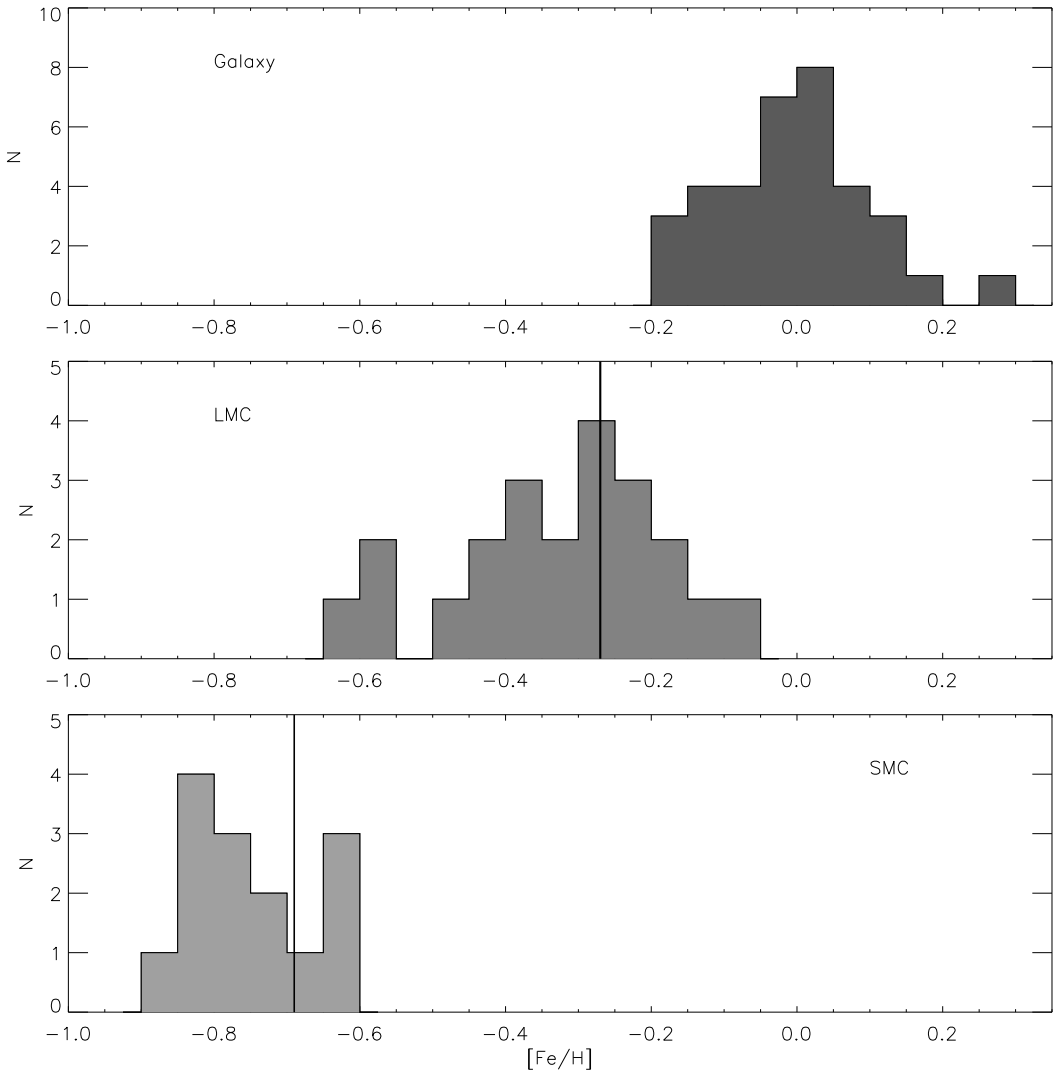

Figure 4.1: *Histograms of the [Fe/H] ratios derived for all the stars of our sample in the Galaxy, the LMC and the SMC. The solid lines indicate the mean values found using F and K supergiants by Hill et al (1995) and Hill (1997) (see Table 4.7 and Section 4.3).*

Table 4.1: *Stellar parameters, FeI and FeII abundances with their errors, number of measured lines of our sample of Galactic Cepheids.*

ID	T_{eff} K	v_t km s^{-1}	$\log g$	[FeI/H]	σ_{FeI}	n(FeI)	[FeII/H]	σ_{FeII}	n(FeII)
EU Tau	6055	2.30	2.1	0.00	0.02	181	+0.02	0.07	12
AX Vel	5855	3.10	1.8	−0.07	0.02	153	−0.06	0.04	11
ST Tau	5740	2.95	1.9	−0.04	0.01	183	−0.05	0.06	11
RZ CMa	6280	3.10	2.2	−0.06	0.01	157	−0.06	0.06	10
SZ Tau	5880	2.80	1.7	+0.03	0.02	152	+0.04	0.05	10
T Vel	5830	2.55	1.8	+0.04	0.01	185	+0.03	0.07	10
AP Pup	6065	3.05	2.1	−0.07	0.02	145	−0.07	0.06	8
V Cen	6130	2.80	1.9	−0.02	0.02	157	−0.03	0.05	9
V Car	5555	3.05	1.8	−0.04	0.01	182	−0.02	0.04	9
RS Ori	6405	2.70	2.2	−0.15	0.02	145	−0.14	0.05	7
W Gem	5750	2.90	1.9	+0.04	0.01	189	+0.05	0.07	9
GH Lup	5480	3.60	1.5	+0.03	0.01	163	+0.01	0.06	9
SX Vel	5375	2.55	1.2	−0.03	0.01	184	−0.02	0.06	10
S Mus	5775	2.75	1.8	+0.18	0.01	187	+0.19	0.05	8
S Nor	5280	2.80	1.1	+0.04	0.01	180	+0.04	0.07	9
β Dor	5175	3.00	1.3	−0.11	0.01	164	−0.11	0.04	6
ζ Gem	5175	3.70	1.4	−0.14	0.02	152	−0.14	0.05	6
XX Cen	5260	2.95	1.3	+0.04	0.01	171	+0.04	0.07	8
UU Mus	5895	3.05	1.7	+0.05	0.01	170	+0.05	0.06	7
U Nor	5230	2.60	1.1	+0.10	0.01	178	+0.13	0.04	9
BN Pup	5050	2.95	0.6	−0.04	0.01	172	−0.07	0.07	9
LS Pup	6545	3.50	2.2	−0.11	0.02	115	−0.10	0.05	8
VW Cen	5240	4.20	1.2	+0.05	0.02	124	+0.07	0.09	5
RZ Vel	5135	4.40	1.6	−0.16	0.02	132	−0.14	0.07	6
WZ Car	4520	1.80	2.1	+0.18	0.02	164	+0.19	0.13	4
VZ Pup	5225	3.25	1.1	−0.18	0.02	141	−0.15	0.07	9
SW Vel	6590	3.75	1.7	−0.17	0.02	96	−0.17	0.05	11
X Pup	5850	3.30	1.4	−0.04	0.02	153	−0.05	0.07	8
T Mon	4760	3.80	0.6	−0.01	0.02	154	−0.03	0.07	8
RY Vel	5245	4.10	1.2	−0.07	0.01	138	−0.06	0.05	6
KQ Sco	4840	3.60	0.7	+0.25	0.02	154	+0.27	0.07	8
AQ Pup	5170	3.10	0.8	−0.09	0.01	174	−0.09	0.06	6
KN Cen	5985	3.80	1.6	+0.07	0.02	121	+0.09	0.08	7
l Car	4705	3.60	0.4	0.00	0.02	132	0.00	0.07	8
U Car	5975	3.00	1.2	+0.12	0.01	160	+0.13	0.06	6
RS Pup	4960	3.50	0.7	+0.12	0.02	152	+0.10	0.09	7

Table 4.2: *Stellar parameters, FeI and FeII abundances with their errors, number of measured lines of our sample of Magellanic Cepheids.*

ID	T_{eff} K	v_t km s^{-1}	$\log g$	[FeI/H]	σ_{FeI}	n(FeI)	[FeII/H]	σ_{FeII}	n(FeII)
				LMC					
HV 6093	5785	4.50	1.5	−0.60	0.02	75	−0.60	0.08	6
HV 2337	5560	3.30	1.6	−0.35	0.02	91	−0.36	0.05	7
HV 2405	6170	4.20	2.3	−0.27	0.03	86	−0.28	0.09	5
HV 12700	5415	3.15	1.4	−0.36	0.02	122	−0.35	0.06	7
HV 12452	5455	2.90	1.0	−0.35	0.02	124	−0.37	0.07	9
HV 2733	5465	2.90	1.8	−0.28	0.02	115	−0.27	0.10	6
HV 971	5925	2.30	1.4	−0.29	0.02	136	−0.29	0.06	9
HV 2864	5830	2.80	1.5	−0.19	0.02	129	−0.20	0.07	9
HV 2260	5765	3.40	1.6	−0.38	0.02	136	−0.36	0.06	4
HV 997	5755	3.10	1.2	−0.21	0.02	114	−0.22	0.08	5
HV 2352	6095	3.65	1.6	−0.49	0.02	83	−0.47	0.07	8
HV 2580	5355	2.75	0.7	−0.24	0.02	128	−0.25	0.05	7
HV 2836	5445	2.85	1.0	−0.16	0.02	115	−0.19	0.08	6
HV 2793	5425	2.90	0.9	−0.10	0.02	122	−0.11	0.10	6
HV 1013	4740	5.35	0.2	−0.59	0.03	77	−0.60	0.08	2
HV 1023	5825	3.10	1.1	−0.28	0.02	101	−0.27	0.06	6
HV 2294	5075	3.90	0.5	−0.42	0.02	103	−0.42	0.06	5
HV 879	5625	3.05	1.0	−0.14	0.02	113	−0.14	0.08	5
HV 877	4685	5.40	0.5	−0.44	0.02	78	−0.47	0.08	4
HV 2369	4750	6.00	0.3	−0.62	0.03	81	−0.63	0.07	4
HV 2827	4790	4.00	0.0	−0.38	0.02	91	−0.33	0.13	5
HV 5497	5100	3.40	0.3	−0.25	0.02	95	−0.24	0.08	5
				SMC					
HV 1365	5335	2.48	0.6	−0.82	0.02	112	−0.84	0.04	8
HV 1954	5890	2.47	1.0	−0.76	0.04	101	−0.75	0.06	10
HV 817	5850	3.25	1.0	−0.82	0.02	87	−0.84	0.05	6
HV 11211	4825	2.60	0.0	−0.83	0.02	124	−0.81	0.08	5
HV 2209	6130	2.30	1.1	−0.65	0.02	106	−0.67	0.06	8
HV 847	4785	2.80	0.0	−0.75	0.02	122	−0.77	0.06	6
HV 823	5990	3.80	1.4	−0.80	0.03	65	−0.81	0.09	4
HV 865	6130	1.90	0.5	−0.87	0.03	77	−0.82	0.05	6
HV 2064	5550	3.10	0.7	−0.64	0.02	107	−0.64	0.05	7
HV 2195	5965	2.90	1.0	−0.67	0.02	97	−0.68	0.06	7
HV 837	5135	2.90	0.0	−0.83	0.02	110	−0.80	0.06	6
HV 824	5170	3.00	0.7	−0.73	0.02	118	−0.74	0.06	6
HV 834	5750	2.95	1.2	−0.63	0.02	109	−0.64	0.06	6
HV 829	5055	3.30	0.2	−0.76	0.01	108	−0.73	0.08	6

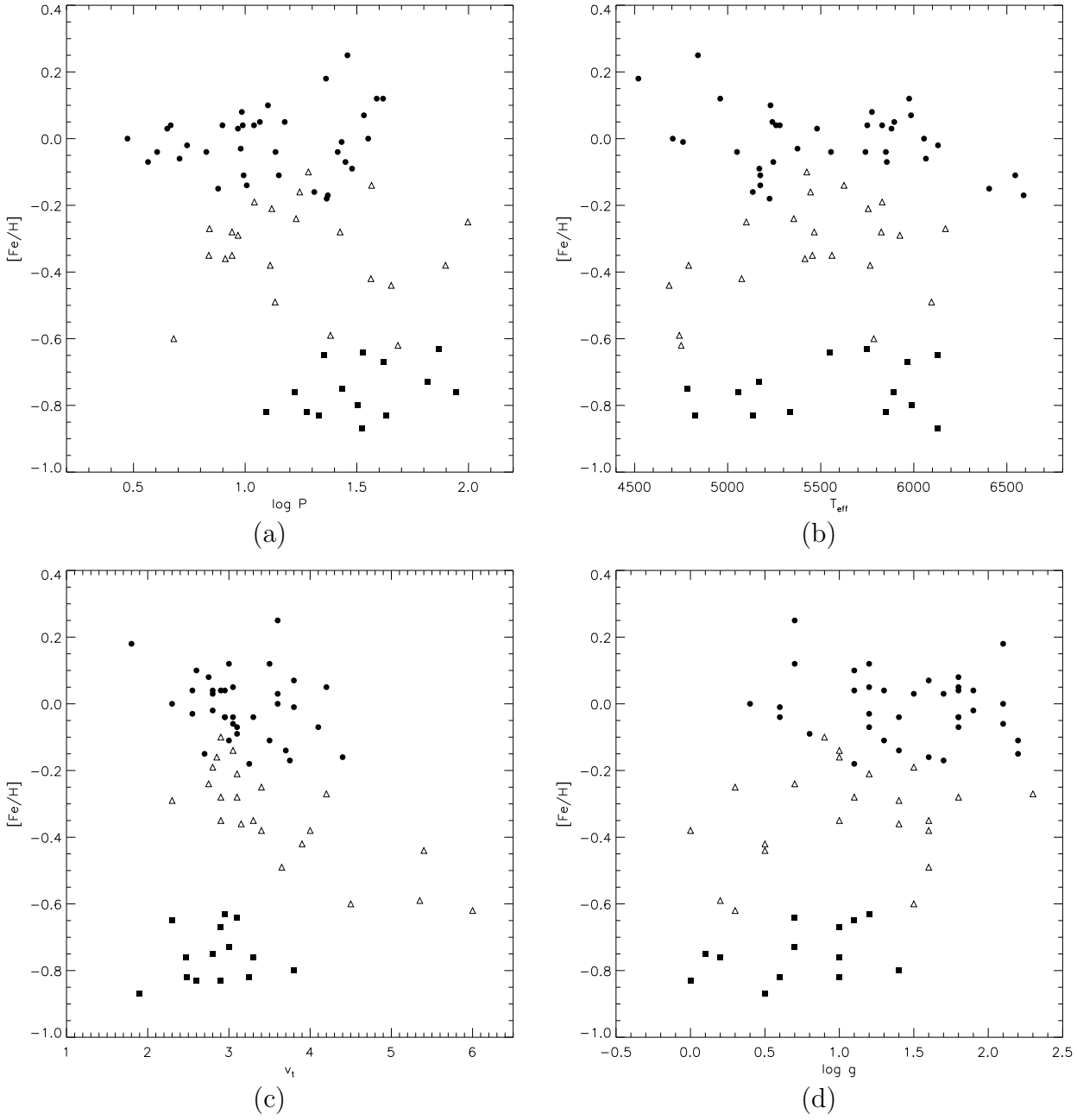

Figure 4.2: *Iron abundances are plotted as a function of the pulsational period (panel a), the effective temperature (panel b), the microturbulent velocity (panel c) and the logarithm of the gravity (panel d) for all the stars of our sample. Filled circles, open triangles and filled squares represent, respectively, Galactic Cepheids, LMC Cepheids and SMC Cepheids.*

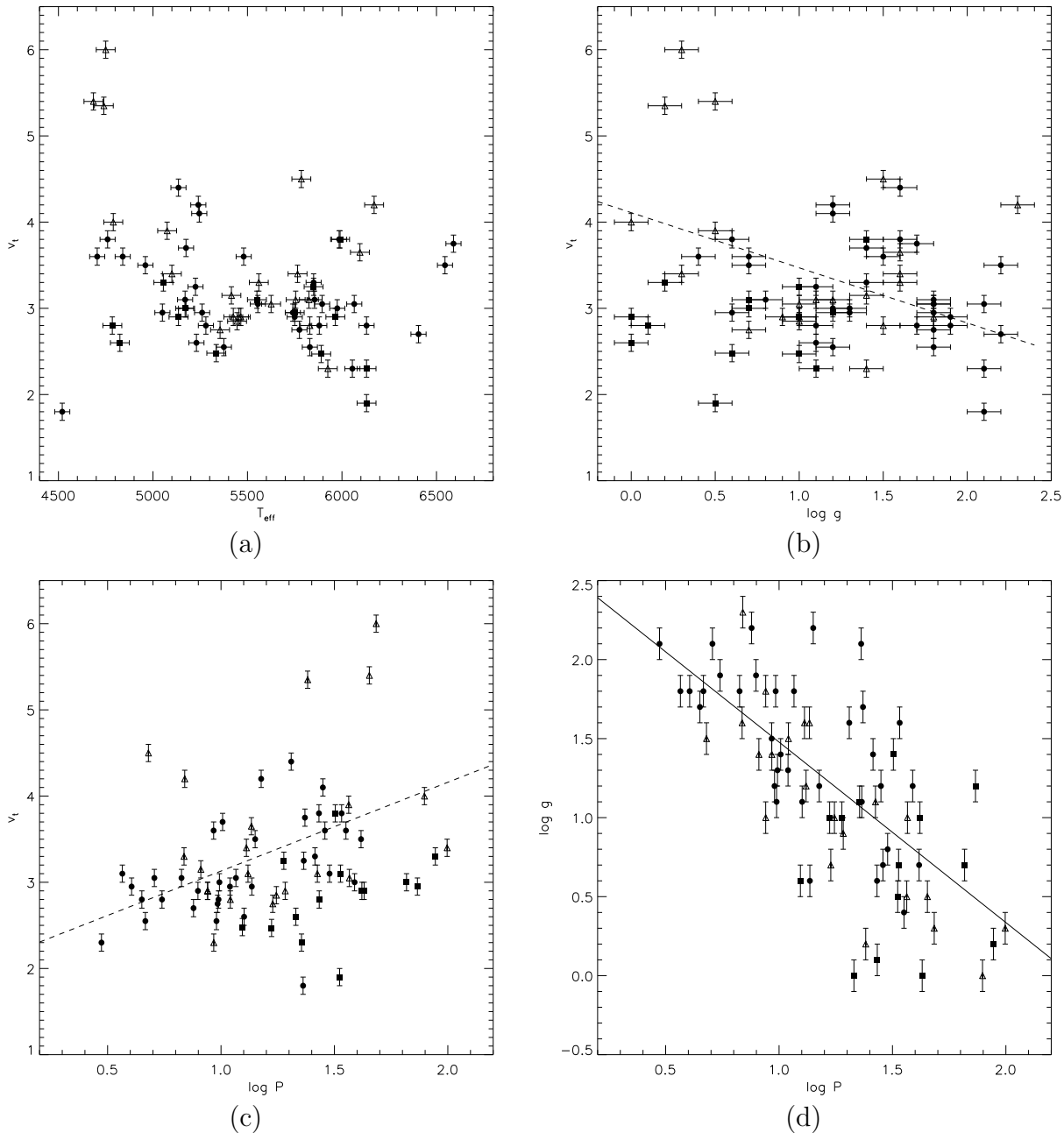

Figure 4.3: *The microturbulent velocity is plotted as a function of the effective temperature, the pulsational period and the gravity (panel a, b and c, respectively), for all the stars of our sample.In panel d, the gravity is plotted as a function of the period. Filled circles, open triangles and filled squares represent, respectively, Galactic Cepheids, LMC Cepheids and SMC Cepheids. The dashed lines represent Fry's relations and the solid line is Fernie's relation.*

Table 4.3: *Effects on derived FeI and FeII abundances from changes in the atmospheric parameters.*

	Δ [FeI/H]	Δ [FeII/H]
$\Delta T_{\rm eff} = +100\ K$	+0.07dex	0.00dex
$\Delta \log g$=+0.1dex	0.00dex	+0.04dex
Δv_t=+0.1 km s^{-1}	−0.03dex	−0.02dex

4.1.2 Uncertainties

The internal uncertainties in the resulting abundances are due to errors from the line-to-line scatter that derive from errors in the atomic data (gf-values) and W measurements. For FeI, which has many lines, the uncertaity in the mean (i.e. $\sigma/\sqrt{(N)}$, where σ is the standard deviation and N is the number of lines) is less than $\pm$0.04 dex with a typical value of $\pm$0.02 dex, while the uncertainties in the mean for FeII is less than $\pm$0.15 dex with a typical value of $\pm$0.07 dex, due to its smaller number of lines.

It is also important to understand the effects of potential systematic errors in the stellar parameters on the final derived abundances (see Table 4.3). In order to do so we have determined the curves of growth for different effective temperatures, microturbolent velocities and gravities in the case of FeI and FeII at a solar iron content (see Fig. 4.4, Fig. 4.5 and Fig. 4.6). We have chosen the FeI line at 5560.21 Å and the FeII line at 6432.68 Å as representative of the behaviour of the two ions because both lines have been measured in all the stars of our sample, they have an average strength and a good gaussian profile.

As expected, we find that FeI has an insignificant dependence on the gravity (Fig. 4.5 top panel) whereas FeII does not depend on the effective temperature (Fig. 4.4 bottom panel). Keeping constant the other stellar parameters we observe that:

- an increase in temperature of 100 K results in an increase in [FeI/H] of about 0.07 dex;
- an increase in v_t of 0.1 km s^{-1} gives a decrease in [FeI/H] of about 0.03 dex and a decrease of 0.02 dex for [FeII/H];
- an increase in $\log g$ of about 0.1 dex produces an increase in [FeII/H] of about 0.04 dex.

These dependencies are summarised in Table 4.3 and we estimated the systematic error to be 0.10 dex for FeI and 0.15 dex for FeII.

We have obtained similar results from curves of growth calculated for a [Fe/H]=−1.0 dex.

A further source of uncertainty and concern could be the fact that our metallicities have been derived from single epoch observations, hence maybe not representative of the average metallicity of each star. However, we note that Fry & Carney (1997, hereafter FC97) did not find any significant difference in their derived [Fe/H] as a function of phase (the test was performed on four of their longest period cepheids) and Luck & Andrievsky (2004) and Kovtyukh et al (2005) show that the elemental abundances for Cepheids with a period between 6 and 68 days are consistent for all

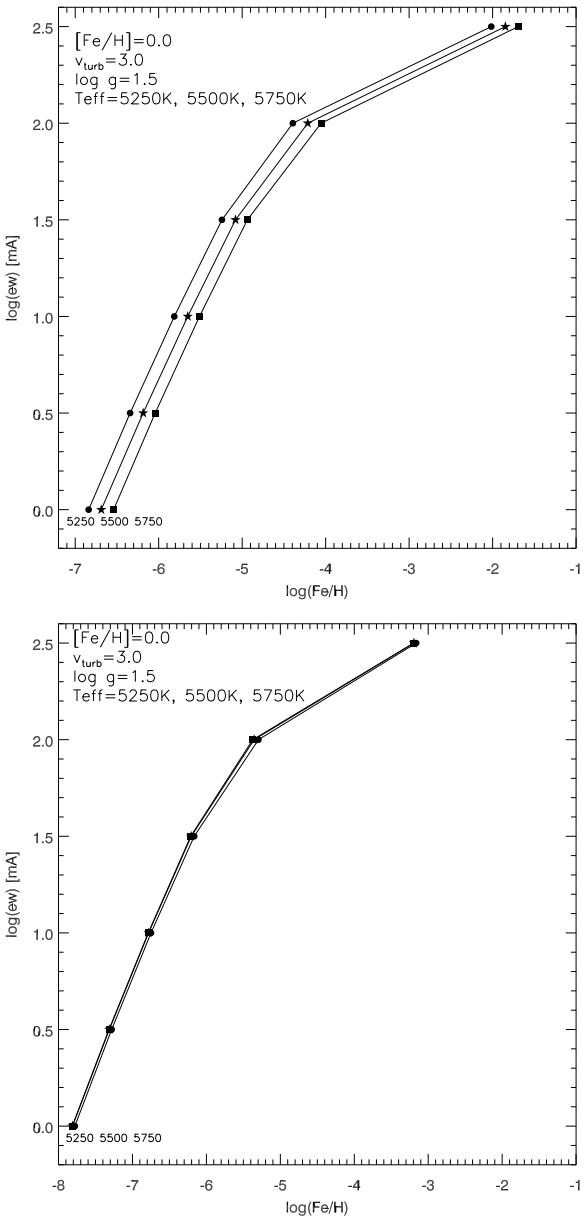

Figure 4.4: *Curves of growth for FeI and FeII (top and bottom panel, respectively), calculated for a range of temperature between 5250 K and 5750 K, for a solar metallicity,* $\log g$*=1.5 and* v_t*=3.0 km* s^{-1}*.*

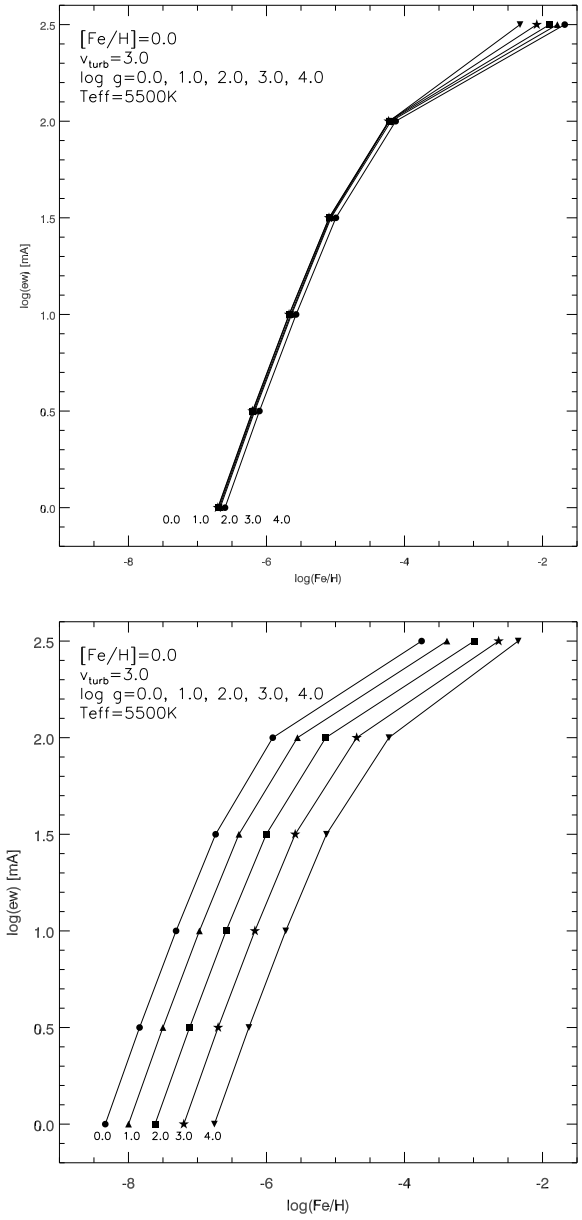

Figure 4.5: *Curves of growth for FeI and FeII (top and bottom panel, respectively), calculated for a range of the logarithm of the gravity between 0.0 and 4.0, for a solar metallicity,* $T_{\rm eff}$*=5500 K and* $\rm v_t$*=3.0 km* s^{-1}.

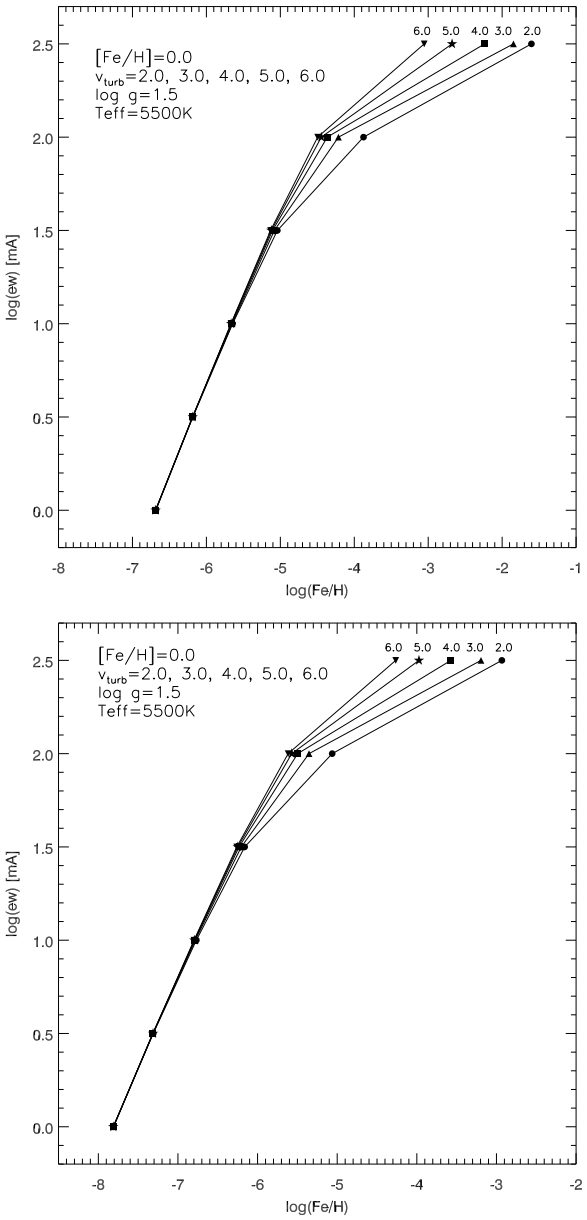

Figure 4.6: *Curves of growth for FeI and FeII (top and bottom panel, respectively), calculated for a range of the microturbulent velocity between 2.0 and 6.0, for a solar metallicity,* $T_{\rm eff}$*=5500 K and* $\log g$*=1.5.*

Table 4.4: *Stellar parameters and iron abundance along the pulsational period of Galactic Cepheid AP Puppis. Phase 0.11 was observed twice 50 days apart, leading to very consistent results.*

Phase	T_{eff} K	v_t	$\log g$ km s^{-1}	[Fe/H]
0.11	6065	3.05	2.1	−0.07
0.11	6125	3.00	2.1	−0.03
0.31	5745	2.80	1.9	−0.03
0.51	5545	3.30	2.0	−0.06
0.91	6155	4.20	2.2	−0.13

pulsational phases. Moreover, our exercise on AP Puppis (see section 3.3 and Table 4.4) also lead to similar conclusions, for a star with a shorter period (5 days). As it can be seen in Table 4.4, not only do the derived stellar parameters nicely follow the expectations from photometry, as shown in Fig 3.9 and Fig 3.10, but the metallicities measured at all phases agree within the errors ($\sim$ 0.1 dex). All of these facts, then, indicate that we are able to recover the true stellar iron content from single epoch observations.

4.2 Comparison with previous studies on Cepheids

Before entering the core of our scientific discussion, i.e. to verify if there is any metallicity effect on the Cepheid PL relation (cf Chapter 6), let us first check how the iron content we have determined for our programme stars compare to previous works. For this purpose, we have selected the analyses of FC97, Andrievsky et al (2002a, 2002b, 2002c) and Luck et al (2003) for the Galactic Cepheids, and Luck & Lambert (1992, hereafter LL92) and Luck et al (1998, hereafter L98) for the Magellanic Clouds, since these are most recent and detailed studies on elemental abundances of Cepheids in these galaxies. When necessary, we have rescaled the literature [Fe/H] values to our solar iron abundance (see Table 4.5 and Table 4.6). In this comparison, one should keep in mind that the same stars have likely been observed at different phases and analysed with different tools and model atmospheres, which may lead to the determination of different combinations of stellar parameters. In the case of observation at different phases, as we have already mentioned in the previous chapter, our results on the five spectra of AP Pup and the conclusions of Luck & Andrievsky (2004) and Kovtyukh et al (2005) show that the derived elemental abundances do not depend on the phase. When multi-phase observations of the same star were available in the literature (this is the case for some of the Galactic Cepheids), we have compared the [Fe/H] values obtained for the same phase of our observations. Otherwise, we chose the iron content corresponding to the closest value of effective temperature to ours.

In total, for the Galactic sample, we have 6 stars in common with FC97 and 18 with the entire sample of Andrievsky's group. For the Magellanic Clouds sample, instead, we have 3 stars in common with LL92 and 7 with L98.

4.2.1 Galactic Cepheids

The mean difference between our results and those of FC97 and Andrievsky's analyses is comparable to the difference between FC97 and Andrievsky's values (0.08 ± 0.02). In more detail, the mean difference between our iron abundances and FC97 is 0.09 ± 0.02, which is satisfactory because is within the errors on our abundances (∼0.1 dex). For 4 stars (V Cen, S Nor, T Mon, ζ Gem) the agreement is at one σ, for the remaining 2 stars (we have 6 in common, in total) the agreement is well within the uncertainties. We note that our abundances for V Cen and S Nor are more in agreement with the metallicity derived by Andrievsky et al. (see below) than with FC97.

When comparing our results to Andrievsky's , we obtain a mean difference of 0.07 ± 0.05. For 14 stars (out of 18), the derived iron abundances are fully comparable within the associated errors. Of the remaining 4 stars, we note that SW Vel, β Dor, and T Mon abundances agree within 2-σ. This is not the case for ζ Gem, for which we cannot explain the difference (0.20 dex) and for which we find instead an agreement with FC97.

The mean differences between our data and FC97 and Andrievsky's analyses are within the errors determined for our abundances.

4.2.2 Magellanic Cepheids

In order to properly compare our results for the Magellanic Cepheids with the values obtained by LL92 and L98, we first have to rescale the latter values for the difference in the adopted solar iron abundance between us (7.51) and them (7.67 and 7.61, respectively). These revised values are reported in the last column of Table 4.6.

In general, the mean metallicities that L98 found with their complete sample (-0.30 dex and -0.74 dex for the LMC and SMC, respectively) are in very good agreement with our results (−0.33 dex and −0.75 dex), they also found a similar spread in both the galaxies. With LL92, instead, there are significant differences (up to 0.4–0.6 dex) which are difficult to understand. Our derived abundances are always smaller than the values derived by LL92, which suggests some hidden systematic effect, but we have not been able to uncover it. For some stars in common L98 and LL92 do not obtain an agreement.

When we move to a star-by-star comparison, larger differences emerge. The comparison between our and L98 abundances discloses a good agreement for 3 object (HV 837, HV 824 and HV 834) and a plausible agreement, i.e. within 2-σ, for other 2 stars (HV 5497, HV 829). Regrettably, this is not the case of HV 879 and HV 2827 for which we note rather large discrepancies (∼ 0.2-0.3 dex) that remain unexplained. As possible explanations, we note that L98 used different analytical codes, different oscillator strengths, and different values of the stellar gravity (they adopted the "physical" gravity calculated from the stellar mass, the luminosity and the temperature).

The larger differences with respect to LL92, for the 3 stars we have in common, could be due to the quality of the LL92 data set is significantly lower than ours (R ≈ 18000 vs 40000) and that their oscillator strengths may differ from our selection: they were taken from the critical compilations of Martin, Fuhr & Wiese (1988) and Fuhr, Martin & Wiese (1988), which are included in VALD but not among the references used for our *gf*-values. Moreover, they have used different

Table 4.5: *Adopted iron abundances of our Galactic sample compared, where it was possible, with previous works: Fry & Carney (1997), Andrievsky et al (2002a, 2002b, 2002c), Luck et al (2003).*

ID	[Fe/H]	$[Fe/H]_{FC}$	$[Fe/H]_{A}$
EU Tau	0.00	-	−0.03 [a]
AX Vel	−0.07	-	-
ST Tau	−0.04	-	-
SZ Tau	+0.03	-0.02	+0.06 [a]
T Vel	+0.04	-	−0.04 [b]
AP Pup	−0.07	-	-
V Cen	−0.02	−0.12	+0.04 [a]
V Car	−0.04	-	-
RS Ori	−0.15	-	-
W Gem	+0.04	-	-
GH Lup	+0.03	-	-
SX Vel	−0.03	-	−0.04 [b]
S Mus	+0.08	-	-
S Nor	+0.04	−0.05	+0.06 [a]
β Dor	−0.11	-	−0.01 [a]
ζ Gem	−0.14	−0.04	+0.06 [a]
XX Cen	+0.04	-	-
UU Mus	+0.05	-	-
U Nor	+0.10	-	-
BN Pup	−0.04	-	+0.01 [c]
LS Pup	−0.11	-	-
VW Cen	+0.05	-	-
RZ Vel	−0.16	-	−0.11 [b]
WZ Car	+0.18	-	-
VZ Pup	−0.18	-	−0.16 [c]
SW Vel	−0.17	−0.10	−0.05 [b]
X Pup	−0.04	-	0.00 [a]
T Mon	−0.01	+0.09	+0.21 [b]
RY Vel	−0.07	-	−0.03 [b]
KQ Sco	+0.25	-	+0.16 [d]
AQ Pup	−0.09	-	−0.14 [b]
KN Cen	+0.07	-	-
l Car	0.00	-	-
U Car	+0.12	-	-
RS Pup	+0.12	-	+0.16 [b]

[a] Andrievsky et al (2002a)
[b] Luck et al (2003)
[c] Andrievsky et al (2002c)
[d] Andrievsky et al (2002b)

analytical tools: MARCS model atmospheres (Gustafsson et al. 1975) and a modified version of the LINES line-analysis code and MOOG (Sneden 1973) synthesis code. They state that their method overestimates the equivalent widths of the weak lines. In more detail, we noted that for HV 2195 the difference in the derived effective temperatures amounts to 635 K, the LL92 value being the highest. Their temperature was obtained from an extrapolation of the calibration they had used for the rest of the sample (due to the temperature calibration upper limit at 6000 K), which made them to quote a rather large uncertainty on the temperature of this star (± 200 K).A temperature difference of 635 K corresponds to a difference of 0.44 dex in the derived iron abundance, which in turn accounts for most of the difference observed between our and their result. In the case of HV 2294, we noted that the iron abundance derived by LL92 is based only on 5 FeI lines and that they have assumed, instead of determining from the minimisation of the log([Fe/H]) vs W slope, a value of microturbulent velocity of 5 km s^{-1} (to be compared to our value of 3.9 km s^{-1}). A microturbulent velocity difference of 1.1 km s^{-1} corresponds to a difference of -0.33 dex in the derived iron abundance, which cannot justify the observed difference between the two results because is in the wrong direction. We can only suppose that they made a wrong assuption for the microturbulent velocity of this star. Because of all these differences, which are difficult to quantitatively assess, and because of the HV 2195 case we have described above, we are confident that the observed large differences may be only apparent, being significantly reduced once the same tools and methods are applied to the analysis of the two data sets.

4.3 A broader comparison from different stellar population in the Magellanic Clouds

The mean metallicities of our Magellanic sample are in good agreement with previous results obtained for F, K supergiants and B stars in the Magellanic Clouds (see Table 4.7).

Russell & Bessell (1989) found a mean [Fe/H]= -0.30 ± 0.2 dex in the LMC and [Fe/H]= -0.65 ± 0.2 dex in the SMC, analysing high-resolution spectra of 16 F supergiants (8 for each galaxy). In 1995 Hill et al. obtained, from 9 F supergiants from the field of the LMC, a mean iron abundance of -0.27 ± 0.15 dex and Hill (1997) found a mean [Fe/H]= -0.69 ± 0.1 dex, analysing 6 K supergiants in the SMC. Andrievsky et al. (2001) re-analysed the sample of F LMC supergiants studied by Hill et al. (1995) and obtained a slightly lower mean value: [Fe/H]= -0.40 ± 0.15 dex.

Regarding the B stars, Rolleston et al. (1993) and Rolleston et al. (2002) found, from the analysis of 4 stars in the SMC and 5 stars in the LMC, respectively, mean values of metallicity of -0.8 ± 0.20 dex and -0.31 ± 0.04 dex. Korn et al. (2000) obtained for the LMC (studying 6 non-supergiant B stars) a mean [Fe/H]= -0.40 ± 0.2 dex and [Fe/H]= -0.70 ± 0.2 dex for the SMC (from 3 non-supergiant B stars).

In conclusion, the mean iron content of Cepheids, for both the Magellanic Clouds, agree very well with the results obtained for nonvariable stars of similar age, evolutionary models and stars that are progenitors of Cepheids. Cepheids do not show any peculiar differences with these two other population of stars, this indicate that, during this evolutionary stage, there are no significant changes of the original iron content of the gas from which they were formed.

Table 4.6: *Stellar parameters and iron abundances of our Magellanic sample. When available the value from previous studies is also reported (Luck & Lambert 1992; Luck et al 1998). In the last column are listed the same values scaled to the solar abundance of iron adopted in our work.*

ID	[Fe/H]	$[Fe/H]_L$	$[Fe/H]_{Lc}$
LMC			
HV 6093	−0.60	-	
HV 2337	−0.35	-	
HV 2405	−0.27	-	
HV 12700	−0.36	-	
HV 12452	−0.35	-	
HV 2733	−0.28	-	
HV 971	−0.29	-	
HV 2864	−0.19	-	
HV 2260	−0.38	-	
HV 997	−0.21	-	
HV 2352	−0.49	-	
HV 2580	−0.24	-	
HV 2836	−0.16	-	
HV 2793	−0.10	-	
HV 1013	−0.59	-	
HV 1023	−0.28	-	
HV 2294	−0.42	−0.06 [a]	+0.10
HV 879	−0.14	−0.56 [b]	−0.46
HV 877	−0.44	-	
HV 2369	−0.62	-	
HV 2827	−0.38	−0.20 [b]	−0.10
HV 5497	−0.25	−0.20 [b]	−0.10
SMC			
HV 1365	−0.82	-	
HV 1954	−0.72	-	
HV 817	−0.82	-	
HV 11211	−0.83	-	
HV 2209	−0.65	-	
HV 847	−0.75	-	
HV 823	−0.80	-	
HV 865	−0.87	−0.44 [a]	−0.28
HV 2064	−0.64	-	
HV 2195	−0.67	−0.45 [a]	−0.29
HV 837	−0.83	−0.84 [b]	−0.74
HV 824	−0.73	−0.75 [b]	−0.65
HV 834	−0.63	−0.66 [b]	−0.56
HV 829	−0.73	−0.65 [b]	−0.55

[a] Luck & Lambert (1992)
[b] Luck et al (1998)

Table 4.7: *Comparison of the mean metallicities of the Magellanic Clouds with previous study. The number of studied stars are also listed.RB89: Russell & Bessell (1989), R93: Rolleston et al. (1993), H95: Hill et al. (1995), H97: Hill (1997), K00: Korn et al. (2000), A01: Andrievsky et al. (2001), R02: Rolleston et al. (2002)*

Reference	$[Fe/H]_{LMC}$	$[Fe/H]_{SMC}$	Notes
this work	-0.33±0.13	-0.75±0.08	22+14 Cepheids
RB89	−0.30±0.20	−0.65±0.20	8+8 F supergiants
R93	–	−0.80±0.20 [a]	4 B stars
H95	−0.27±0.15	–	9 F supergiants
H97	–	−0.69±0.10	6+3 K supergiants
K00	-0.40 ± 0.20	-0.70 ± 0.20	6 B stars
A01	−0.40±0.15	–	9 F supergiants
R02	-0.31 ± 0.04	–	5 B stars

[a] mean metallicity not from iron

Chapter 5

Preliminary results: α elements

The α elements are those light elements (with atomic number ≤ 22) whose most abundant isotopes are multiples of ^{4}He nuclei: O, Ne, Mg, Si, S, Ar, Ca and Ti. From a phenomenological point of view also Al and Na could be classified as mild α elements, even though their nuclei have odd numbers of protons (McWilliam 1997). However, the noble gas elements Ne and Ar cannot be detected in cool stars (like Cepheids) and S has only very weak spectral lines in the near-infrared. So these elements, usually, are not considered in the typical analysis of α elements in the optical band.

Massive stars ($M > 8\ M_\odot$) that end their life as Type II Supernovae[a] (SNe II) are the principal producers of α elements. Iron and the iron-peak elements (with atomic number between 22 and 30) are produced in both Type Ia Supernovae[b] (SNe Ia) and SNe II, though SNe Ia are the main source. The return of synthesised material to the interstellar medium through SNe Ia is slow relative to the "instantaneous" return from massive stars. Massive stars have a lifetime of less than $3{\cdot}10^7$ years, while SNe Ia have lifetimes similar to those of low and intermediate mass stars i.e. between $3{\cdot}10^7$ years and $15{\cdot}10^9$ years, since they originate from a white dwarf. A simple prediction is that stars that form shortly after the interstellar medium has been enriched by SNe II should have enriched [α/Fe][c] ratios, while those that form sometime after the SNe Ia contribute will have higher iron abundances and lower [α/Fe] ratios. Considering the individual α elements, Edvardsson and collaborators (1993) pointed out differences of trend with [Fe/H], this suggests that the α elements may not be made in a single process but produced in different amounts by different SNe. It is then interesting to investigate the individual behaviours of the α element abundances.

The evolution of the chemical abundances in a galaxy is intimately linked to its star formation history (SFH) (e.g. Tinsley 1979; Pagel 1998) and [α/Fe] is particularly interesting in its study. As described by Matteucci (2003), the timescale for changes in the [α/Fe] ratio depends not only

[a] Explosion of a massive star that has gone through all the steps of fusion. Its spectrum presents hydrogen Balmer lines.

[b] Explosion of a white dwarf that accreted matter from a nearby companion star until it reached the Chandrasekhar limit. Its spectrum is characterised by a Si absorption line near its light peak.

[c] Where α is the average abundance relative to H of the α elements

on the SFH but also on the initial mass function[a] (IMF), the SNe Ia timescale and the timescales for mixing the SNe Ia and SNe II products back into the interstellar medium.

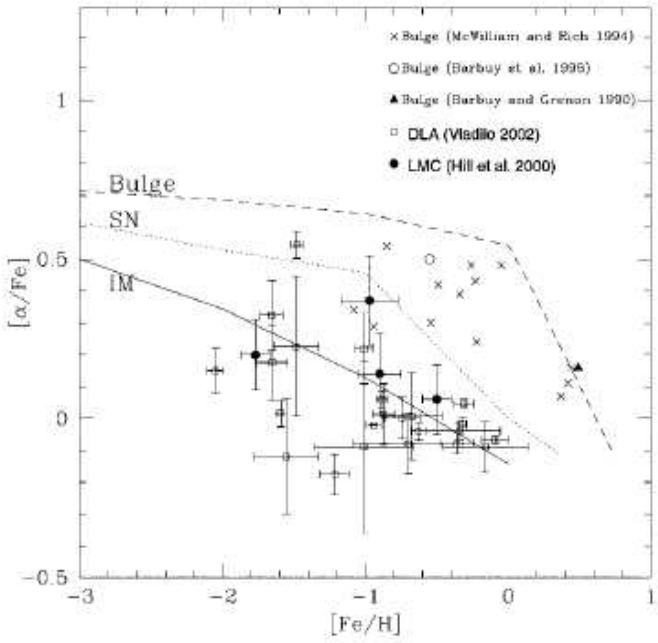

Figure 5.1: *The predicted [α/Fe] ratios for three different histories of star formation but equal IMF and nucleosynthesis: a spheroid (bulge or elliptical, dashed line), the solar neighbourhood (SN, dotted line) and a Magellanic irregular galaxy (IM, solid line). For comparison are also shown data points for stars and clusters in the Galactic bulge (crosses, open circles and filled triangles), for globular clusters in the LMC (filled circles) and Damped Lyman-α objects (open squares). Figure from Matteucci 2003.*

The SFH influences the α abundance ratio vs. iron abundance diagrams in the following ways: galaxies with low star formation activity either in burst or continuous (spiral and irregular galaxies) will show a short plateau in [α/Fe] ratio at very low metallicities, whereas galaxies with strong and fast star formation (elliptical galaxies or bulges) will have a longer plateau for [α/Fe].

Figure 5.1 shows the theoretical prediction by Matteucci (2003) of the [α/Fe] ratio as a function of [Fe/H] for different SFHs. In particular,the dashed line represents the position for a spheroid (bulge or elliptical), the dotted line for the solar neighbourhood and the solid line for a Magellanic irregular galaxy. For comparison are also shown data points for stars and clusters in the Galactic bulge, for globular clusters in the LMC and Damped Lyman-α system[b].

[a]Relation that specifies the mass distribution of a newly formed stellar population

[b]Thick region of hydrogen with a very high energy light source, typically a quasar, that shines at us behind this region. The observed spectrum presents a Lyman-α line in absorption.

We observe that [α/Fe] increases with decreasing [Fe/H] for the three different SFHs. In particular we note that in the range between about -1.0 dex and 0.2 dex, which corresponds to the range of the iron content for our stars, the trend for the Magellanic irregular is shallower than the trend for the solar vicinity and it reaches a value of [α/Fe]$\sim$0.1-0.2 dex at [Fe/H]=$-$1.0, while the other reaches [α/Fe]$\sim$0.5 dex at the same iron abundance.

Our analysis of the α elements is focused on the determination of O, Na, Mg, Al, Si, Ca and Ti abundances for our programme stars. We investigate the behaviours of the abundances relative to iron as a function of the iron content and we will use the resulting abundances to be able to get a better estimate of the total metallicity. This is used to assess the effect of the chemical composition on the Cepheid Period-Luminosity relation (see Chapter 6).

5.1 Abundance analysis

We have derived the abundances of sodium, magnesium, aluminium, silicon, calcium and titanium with the method of the equivalent widths; while we have adopted the spectrum synthesis technique to determine the oxygen abundances because the lines adopted as index of the abundance are weak and one has a known blend with a NiI feature (see Chapter 3 for a description of the methods). We will explain the details about the determination of oxygen abundances in the next section. Regarding the other elements we have calculated their abundances with the Kurucz WIDTH9 code using as inputs the equivalent widths of the lines we have selected and the LTE model atmospheres (computed by Castelli & Kurucz 2003) characterised by the set of stellar parameters we have determined in the analysis of the iron abundances (see section 3.4). In other words, for this second step of the chemical analysis of our sample of Cepheids, we only need to measure the equivalent widths of the selected lines of the α elements and run the WIDTH9 code with the model atmosphere previously adopted in the calculation of the iron content for each star. The final abundance of an element is the mean value of the abundances obtained from each spectral line that falls in the useful range of equivalent widths (5-150 mÅ, see section 3.3).

We calculate the abundances of the α elements relative to the Sun adopting the solar abundances from Grevesse & Sauval (1998), listed in Table 5.1, on a scale where log[n(H)]=12. Recently, new solar abundances have been published (Lodders 2003, Asplund et al 2004) but revision for the elements we are interested in are negligible.

The internal error in the determination of the α elements abundances are listed in Table 5.2. They are due to uncertainties in the atomic data (gf-values) and equivalent width measurements and they can be evaluated from the line-to-line scatter. We adopted for each element the average over all the sample of the standard deviations of the mean:

$$\sigma = \sqrt{\langle \sigma_{[X/H]} \rangle^2_{all\ stars}} \tag{5.1}$$

where $\langle \sigma_{[X/H]} \rangle$ is the standard deviation of the mean of the abundance of element X given by the individual lines for each star.

To understand the effects of potential systematic errors in the stellar parameters on the final abundances a series of tests were conducted on three stars, chosen for their stellar parameters

Table 5.1: *Solar abundances of Na, Mg, Al, Si, Ca and Ti from Grevesse and Sauval (1998) and of O from Holweger (2001), on a scale where log[n(H)]=12.*

Element	Abundance
O	8.74
Na	6.33
Mg	7.58
Al	6.47
Si	7.55
Ca	6.36
Ti	5.02

Table 5.2: *The internal uncertainties in the resulting abundances for each α element.*

Abundance	Error
[O/H]	0.10
[Na/H]	0.10
[Mg/H]	0.10
[Al/H]	0.10
[Si/H]	0.05
[Ca/H]	0.10
[TiI/H]	0.05
[TiII/H]	0.08

that exemplified the average characteristics of Cepheids ($T_{\rm eff}$ close to 4500 K, 5500 K and 6500 K, $\log g$ ∼1.5 and v_t ∼3.0 km s^{-1}). For each test star, the same set of line measurements used in the abundance determinations was run through 6 different atmospheres with WIDTH9, each with one stellar parameter varied from the original value. The parameters were varied by the following quantities: $T_{\rm eff}$ ±100 K, $\log g$ ±0.1 dex and v_t±0.1 km s^{-1}. For each star in a given test, the resulting abundances for each elements were compared with the abundances derived with the original parameters. These differences were averaged over all the 3 stars. The results are listed in Table 5.3.

5.1.1 Oxygen abundances

To determine the oxygen abundances we have selected the [OI] forbidden lines at 6300.31 Å and 6363.78 Å. These are the most popular indices of the oxygen abundance in cool stars along with the triplet of OI at 7771.94 Å 7774.16 Å and 7775.39 Å and the OH lines (the latter are in the ultra-violet and infrared bands). The triplet lines can be observed in the FEROS spectra, i.e. for the Galactic Cepheids of our sample, but not in the spectra of the Magellanic Cepheids because they have been observed in a narrower spectral range: from 4800 Å to 6800 Å (UVES setting centred at 5800 Å).

Table 5.3: *Effects on derived α elements abundances from changes in the atmospheric parameters.*

	$\Delta T_{eff} = \pm$ 100 K	$\Delta \log g = \pm 0.1$ dex	$\Delta v_t = \pm 0.1$ km s^{-1}
[Na/H]	$\pm$ 0.06	$\pm$ 0.00	$\mp$ 0.01
[Mg/H]	$\pm$ 0.06	$\pm$ 0.00	$\mp$ 0.01
[Al/H]	$\pm$ 0.05	$\pm$ 0.01	$\mp$ 0.01
[Si/H]	$\pm$ 0.05	$\pm$ 0.00	$\mp$ 0.01
[Ca/H]	$\pm$ 0.09	$\pm$ 0.01	$\mp$ 0.02
[TiI/H]	$\pm$ 0.11	$\pm$ 0.01	$\mp$ 0.01
[TiII/H]	$\pm$ 0.01	$\pm$ 0.04	$\mp$ 0.01

However the 7771 Å triplet is rather strong and highly sensitive to the effective temperature and they form in condition far from the Local Thermodynamical Equilibrium. Many studies (e.g. Nissen et al 2002) point out the discrepancies of the [OI] abundances and OI triplet abundances obtained with the 1-dimension model atmospheres (i.e. the classical approach) and we use this kind of model atmospheres. Thus, to obtain the final oxygen abundances of the Galactic Cepheids, we have decided to use only the two forbidden lines.

More oxygen lines in the optical band would improve the accuracy of the analysis, however weaker (forbidden and allowed) OI lines either appear to be heavily blended with several other features, lack atomic data, are affected by large uncertainties in the continuum location or suffer some of these problems simultaneously. Thus they cannot be reliable for an abundance analysis (Allende Prieto et al 2001).

Both the [OI] forbidden lines are weak and the line at 6300 Å has a well-known blend with a NiI feature at 6300.33 Å (see Fig 5.2 from Allende Prieto et al 2001). Its contribution to the 6300 feature is not negligible and it is not possible to evaluate it correctly with the equivalent width method we have adopted for the other elements. Thus we used the spectrum synthesis technique that allows a detailed evaluation of this blended line. Fig 5.2 shows the difference between the best fit obtained from the comparison of observed and synthetic profiles considering the 6300 feature as a product of oxygen and nickel (panel a) and as entirely produced by oxygen (panel b, test made by Allende Prieto et al 2001 on the spectrum of the Sun). Without taking into account the Ni line, the predicted [OI] line has a wrong central wavelength and a line shape different from observed. It is then essential to take into account the nickel contribution for a correct determination of the oxygen abundance.

Regrettably we could not measure these [OI] lines in half of the Galactic sample and in 14 out of 22 LMC Cepheids, due to a quite severe blending with telluric lines. Unfortunately, we did not plan and carry out the necessary observations of calibrating stars for each night to subtract the contribution of the earth atmosphere, because the original goal of the observational campaign was only the determination of the iron abundance. Without these additional observations we cannot correct our spectra for the telluric lines and there are no alternative methods to solve the problem. We determined then the oxygen abundance only for a subsample of 40 out of 72 stars.

As we have explained in Chapter 3, to apply the spectrum synthesis method to our spectra

we use the MOOG code. This program needs as inputs a line list, the observed spectrum and a model atmosphere. We assembled two line lists (see Appendix B) of the [OI] 6300 Å and [OI] 6363 Å regions and we adopted for each star under scrutiny the model atmospheres determined from the analysis of the iron abundance. Then the code calculates the synthetic profile in the region of interest and compares it with the observed spectrum. Running MOOG, we can interactively change the initial values we have set for the oxygen abundance and, also, adapt the line-broadening parameters in order to reproduce the observed profile. We chose to superimpose a set of three trial synthetic spectra in order to evaluate the error on the final abundance. Representative syntheses of the [OI] 6300 Å are shown in Fig. 5.3.

The solar abundance value for oxygen we have adopted as reference (to determine [O/H]) is: 8.74 on a scale where log[n(H)]=12 (Holweger 2001). This is an updated and more correct value with respect to the one obtained by Grevesse & Sauval (1998). The final abundance is the mean

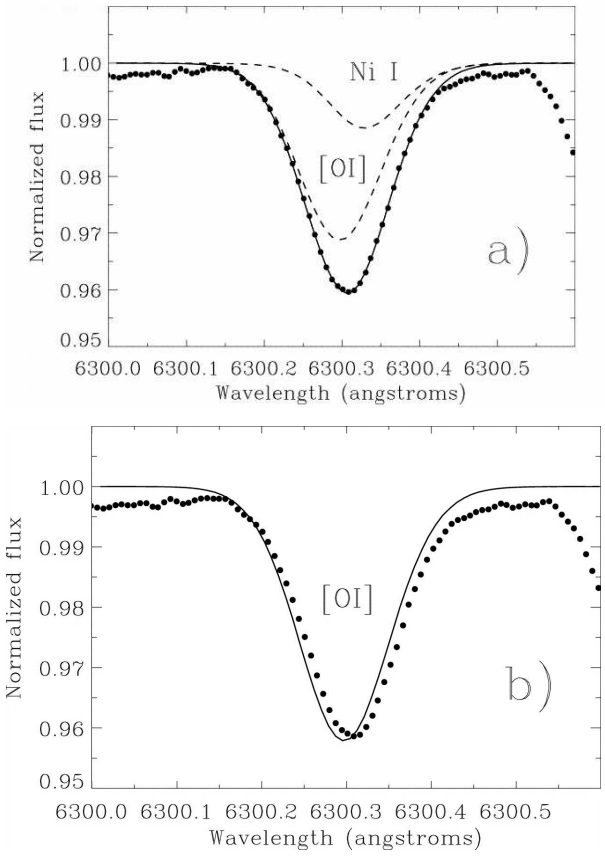

Figure 5.2: *(a) The comparison between the observed (filled circles) and the synthetic profiles after the determination of the best fit. The individual calculation of oxygen and nickel are also shown. (b) Best fit, assuming the observed feature is entirely produced by the oxygen forbidden line (from Allende Prieto et al 2001).*

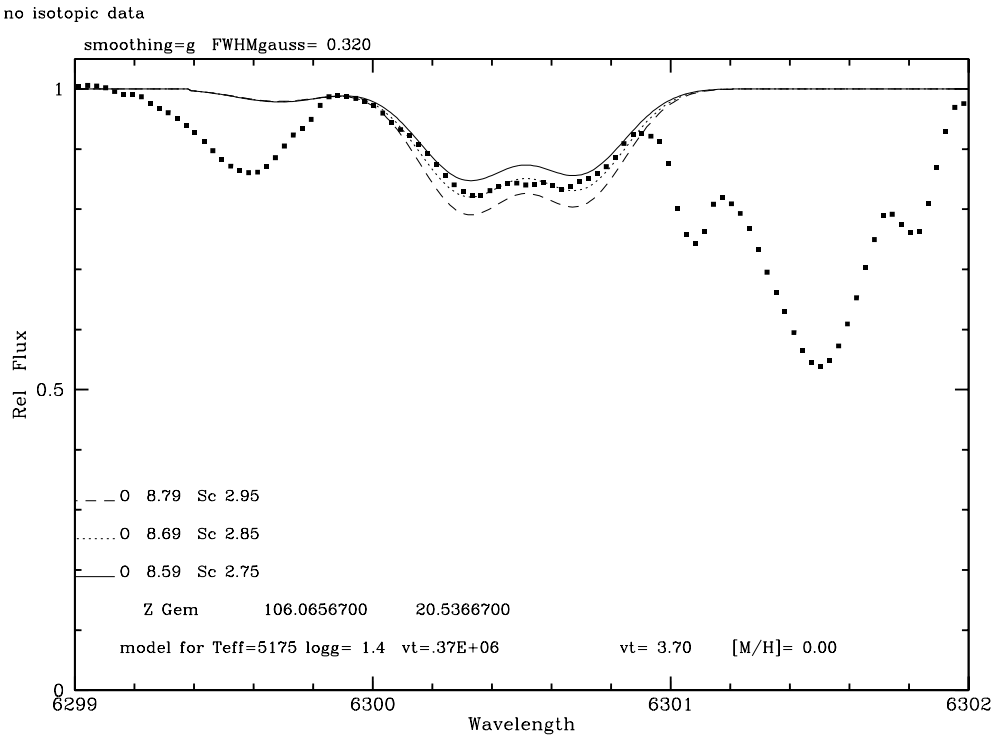

Figure 5.3: *Syntheses (solid, dotted and dashed lines) of [OI] at 6300.31 Å vs. observed spectra (black dots) for the Galactic Cepheid ζ Gem. The three abundances, determined on a scale where log[n(H)]=12, are:* $\log\epsilon$*(O)=8.79, 8.69 and 8.59. It can be see that the ScII line at 6300.6 can be easily matched and does not seriously perturb the measure of the O abundance.*

value of the abundances obtained for the two [OI] lines, and, from the quality of the fits, we expect the internal accurancy to be of order of $\pm$0.10 dex.

5.2 Results and comparison with previous works

The resulting abundance ratios (relative to iron) of the α element under scrutiny are listed in Table 5.4 and Table 5.5 for the Galactic and the Magellanic sample, respectively. For three Magellanic Cepheids we have not been able to measure any Na lines in the useful range of equivalent widths (5-150 mÅ, see section 3.2), because the Na lines in these spectra are too strong (i.e. above the limit of 150 mÅ). For one star (HV 1013) Al lines were all too weak, then we could not determine its Al abundance.

We observe that several stars present different abundances for TiI and TiII. Measuring these

ions gives us another gravity indicator (from their balance) besides iron, thus disagreement between the TiI and TiII abundances may indicate some problems about the gravity determination. We have checked that a change in the gravity of ± 0.1 dex (i.e. 1-σ deviation) solves the problem only partially: for stars with differences in abundance of the order of 0.2 dex we can obtain the balance between TiI and TiII; for stars with larger differences between the TiI and TiII abundances rather large variation in the gravity from the adopted value are needed to reach the balance. We have, then, tested the possibility of problems with the gf-values of the lines, recalculating the abundances with different gf-values for a sub-sample of lines but we did not observe any significant change in the Ti abundances.

The problem of the balance of TiI and TiII abundances seems quite common in the literature, for example in Luck & Lambert (1992), Luck et al (1998) and Andrievsky and collaborators' works (2002abc). They all found discrepancies in the TiI and TiII abundances, although they did not give any explanation or indication on the possible reasons. Fulbright (2000), in his study of halo and disk stars (in the Galaxy), observed an offset in the solar values of TiI and TiII. He derived the values of $\log \epsilon$(TiI)=4.86 and $\log \epsilon$(TiI)=5.00 from observation of the solar spectrum, while Grevesse & Sauval (1998) give $\log \epsilon$(Ti)=5.02. He corrected his TiI abundances for a value of +0.11 dex, estimated as the average of the differences between his TiI and TiII abundances, obtaining in this way the balance between the two ions. If we apply such correction to our stars we can solve partially the problem, reducing the differences only for the Galactic Cepheids, since the discrepancies for the Magellanic Cepheids are in the opposite direction. To solve this problem we need further investigations to determine other possible sources for these differences.

5.2.1 Individual trends of the abundance ratios

Figure 5.5 and Fig. 5.6 show the individual trends of the abundances ratio of the α elements as a function of [Fe/H]. The black squares, circles and stars indicate the abundance ratios of our SMC, LMC and Galactic Cepheids, respectively. The green upside-down triangles are data from Luck et al (1998), they are abundance ratios of Magellanic Cepheids and Galactic supergiants. The large set of abundances obtained for Galactic Cepheids by Andrievsky's group (Andrievsky et al 2002a, 2002b, 2002c; Luck et al 2003) is indicated by purple triangles.

Si and Ca

The top and bottom panels in Fig. 5.5 show, respectively, Si and Ca trends as function of [Fe/H]. Both Si and Ca ratios increase as the iron abundance decreases, reaching a value around 0.1 ± 0.05 dex and 0.2 ± 0.10 dex at [Fe/H]$=-0.9$. We note a fairly good agreement with Luck data in the range of iron abundances corresponding to the Magellanic Clouds, while it seems that our Si and Ca ratios are slightly underabundant and overabundant, respectively, in comparison with Andrievsky's results. These small differences can be due to the different programs used to determine the abundances and set of model atmospheres, that usually are of the order of 0.1 dex. Considering the observational results obtained by Sneden (2004) for Galactic globular and open clusters and halo field stars (see Fig 5.4), we observe that the Ca trend found for Cepheids agrees very well with it. Moreover both Si and Ca trends for the Magellanic sample follow the theoretical prediction by

Table 5.4: *Fe abundances and α element abundances relative to Fe of our sample of Galactic Cepheids.*

ID	[Fe/H]	[O/Fe]	[Na/Fe]	[Mg/Fe]	[Al/Fe]	[Si/Fe]	[Ca/Fe]	[TiI/Fe]	[TiII/Fe]
EU Tau	0.00	−0.10	+0.11	−0.15	−0.35	−0.07	+0.07	−0.23	−0.20
AX Vel	−0.07	−0.12	+0.03	−0.28	−0.15	−0.08	+0.08	−0.26	−0.19
ST Tau	−0.04	+0.04	+0.34	−0.04	−0.12	+0.05	+0.07	−0.11	0.00
RZ CMa	−0.06	−0.09	+0.06	−0.19	−0.23	+0.07	+0.10	−0.19	−0.03
SZ Tau	+0.03	−0.27	+0.22	−0.21	−0.20	−0.05	+0.17	−0.23	−0.30
T Vel	+0.04	−0.06	+0.05	−0.14	−0.23	+0.02	+0.10	−0.23	−0.09
AP Pup	−0.07	-	+0.08	−0.24	−0.15	−0.03	+0.02	−0.17	−0.11
V Cen	−0.02	-	+0.08	−0.11	−0.04	+0.02	−0.06	−0.15	−0.15
V Car	−0.04	+0.06	+0.15	−0.17	−0.13	−0.05	+0.05	−0.20	−0.11
RS Ori	−0.15	-	+0.25	−0.11	−0.36	+0.03	+0.12	−0.08	+0.23
W Gem	+0.04	+0.03	+0.12	−0.11	−0.20	+0.00	+0.04	−0.12	+0.06
GH Lup	+0.03	−0.10	+0.13	−0.15	−0.15	−0.04	+0.01	−0.23	−0.22
SX Vel	−0.03	-	+0.13	−0.12	−0.13	+0.01	+0.08	−0.19	−0.16
S Mus	+0.18	−0.18	+0.02	−0.24	−0.23	−0.18	−0.06	−0.33	−0.22
S Nor	+0.04	−0.14	+0.27	−0.23	+0.00	+0.04	+0.05	−0.25	−0.20
β Dor	−0.11	+0.08	+0.32	−0.08	−0.03	+0.00	+0.06	−0.25	−0.03
ζ Gem	−0.14	+0.09	+0.43	−0.07	+0.01	+0.01	0.00	−0.12	−0.04
XX Cen	+0.04	+0.06	+0.24	−0.17	−0.10	+0.02	+0.04	−0.28	−0.07
UU Mus	+0.05	-	+0.13	−0.30	−0.18	−0.07	+0.04	−0.21	−0.18
U Nor	+0.13	-	+0.26	−0.08	−0.19	−0.01	−0.02	−0.30	−0.24
BN Pup	−0.04	-	+0.13	−0.16	−0.05	+0.03	−0.04	−0.24	−0.14
LS Pup	−0.11	-	+0.10	−0.26	−0.38	−0.04	−0.05	−0.05	0.00
VW Cen	+0.05	-	+0.19	−0.31	−0.05	+0.05	−0.01	−0.36	−0.32
RZ Vel	−0.16	+0.16	+0.25	0.00	−0.11	+0.01	+0.01	−0.26	+0.33
WZ Car	+0.18	-	+0.40	−0.10	+0.10	−0.15	+0.24	+0.25	−0.11
VZ Pup	−0.18	-	+0.40	−0.25	−0.03	−0.10	+0.14	−0.32	+0.03
SW Vel	−0.17	−0.23	+0.26	+0.01	−0.18	−0.02	0.00	−0.03	−0.10
X Pup	−0.04	+0.04	+0.14	−0.27	−0.15	−0.05	+0.02	−0.24	−0.11
T Mon	−0.01	-	+0.32	−0.20	0.00	0.00	−0.04	−0.24	−0.25
RY Vel	−0.07	-	+0.29	−0.60	−0.03	−0.04	+0.13	−0.23	−0.21
KQ Sco	+0.25	-	+0.25	−0.45	−0.10	−0.10	−0.27	−0.40	−0.33
AQ Pup	−0.09	-	+0.20	−0.11	−0.03	0.00	+0.02	−0.23	−0.03
KN Cen	+0.07	-	+0.21	+0.22	−0.05	−0.01	+0.22	−0.15	−0.14
l Car	0.00	-	+0.06	−0.34	−0.12	−0.02	−0.19	−0.32	−0.38
U Car	+0.12	−0.12	+0.21	−0.15	−0.15	−0.08	+0.11	−0.14	−0.13
RS Pup	+0.12	-	+0.34	−0.15	−0.13	−0.09	−0.10	−0.40	−0.28

Table 5.5: *Fe abundances and α element abundances relative to Fe of our sample of Magellanic Cepheids.*

ID	[Fe/H]	[O/Fe]	[Na/Fe]	[Mg/Fe]	[Al/Fe]	[Si/Fe]	[Ca/Fe]	[TiI/Fe]	[TiII/Fe]
					LMC				
HV 6093	−0.60	-	−0.07	−0.17	−0.25	−0.06	+0.00	−0.06	−0.32
HV 2337	−0.35	+0.05	−0.13	−0.18	−0.18	−0.14	+0.15	−0.02	+0.04
HV 2405	−0.27	-	−0.04	+0.03	−0.30	−0.08	+0.03	+0.05	−0.05
HV 12700	−0.36	+0.19	−0.12	+0.02	−0.31	+0.02	+0.17	−0.06	+0.05
HV 12452	−0.35	+0.20	−0.07	+0.00	−0.21	+0.14	+0.15	+0.05	−0.12
HV 2733	−0.28	-	−0.17	−0.18	−0.17	−0.03	+0.11	−0.10	+0.11
HV 971	−0.29	-	−0.22	−0.15	−0.21	−0.02	+0.16	−0.03	−0.22
HV 2864	−0.19	-	−0.24	−0.05	−0.31	−0.10	+0.19	−0.01	−0.15
HV 2260	−0.38	+0.13	−0.05	−0.15	−0.01	+0.09	+0.23	+0.05	+0.09
HV 997	−0.21	-	−0.08	−0.16	−0.09	−0.02	+0.08	+0.00	−0.22
HV 2352	−0.49	−0.01	0.13	+0.11	−0.30	+0.07	+0.15	+0.05	+0.02
HV 2580	−0.24	−0.06	−0.20	−0.30	−0.17	−0.04	+0.09	−0.10	−0.21
HV 2836	−0.16	-	−0.32	+0.02	−0.32	−0.10	+0.08	−0.15	−0.22
HV 2793	−0.10	-	−0.38	−0.23	−0.37	−0.07	+0.02	−0.18	−0.26
HV 1013	−0.59	−0.06	-	−0.13	0.00	−0.01	+0.07	−0.19	−0.25
HV 1023	−0.28	-	−0.30	−0.26	−0.08	−0.08	+0.18	−0.08	−0.10
HV 2294	−0.42	-	−0.15	−0.04	−0.01	+0.09	+0.13	−0.04	0.00
HV 879	−0.14	-	−0.31	−0.30	−0.38	−0.13	0.00	−0.11	−0.09
HV 877	−0.44	-	−0.13	−0.35	−0.18	+0.01	+0.11	−0.17	+0.12
HV 2369	−0.62	+0.19	−0.07	−0.25	−0.09	+0.09	+0.07	−0.10	0.00
HV 2827	−0.38	-	−0.02	+0.02	−0.07	+0.07	+0.14	−0.11	−0.15
HV 5497	−0.25	-	−0.09	−0.43	−0.21	−0.07	+0.24	−0.08	−0.11
					SMC				
HV 1365	−0.82	−0.13	−0.21	−0.04	−0.26	+0.08	+0.15	−0.06	−0.13
HV 1954	−0.76	+0.04	-	+0.11	−0.05	+ 0.14	+0.24	+0.03	−0.26
HV 817	−0.82	+0.15	−0.01	0.06	−0.03	+ 0.01	+0.16	+0.14	−0.05
HV 11211	−0.83	−0.08	−0.32	−0.14	−0.26	+0.08	+0.22	−0.13	−0.19
HV 2209	−0.65	+0.13	−0.19	−0.08	−0.11	+0.05	+0.21	+0.12	−0.18
HV 847	−0.75	+0.13	−0.30	−0.20	−0.20	+0.11	+0.21	−0.09	−0.24
HV 823	−0.80	+0.05	-	−0.27	-	+0.03	0.04	+0.12	−0.04
HV 865	−0.87	+0.10	−0.26	−0.22	+0.16	−0.06	+0.08	−0.01	−0.05
HV 2064	−0.64	−0.03	−0.08	−0.19	+0.02	+0.04	+0.14	−0.02	−0.13
HV 2195	−0.67	+0.12	−0.34	−0.27	+0.12	+0.18	+0.16	+0.08	−0.16
HV 837	−0.83	+0.01	0.00	−0.11	−0.15	+0.12	+0.24	−0.01	−0.24
HV 824	−0.73	+0.22	−0.32	−0.15	−0.28	+0.06	+0.24	−0.01	−0.02
HV 834	−0.63	+0.13	−0.22	−0.26	−0.23	+0.08	+0.08	+0.01	+0.06
HV 829	−0.76	+0.09	+0.01	+0.14	−0.06	+0.06	+0.18	−0.02	−0.19

Matteucci (2003).

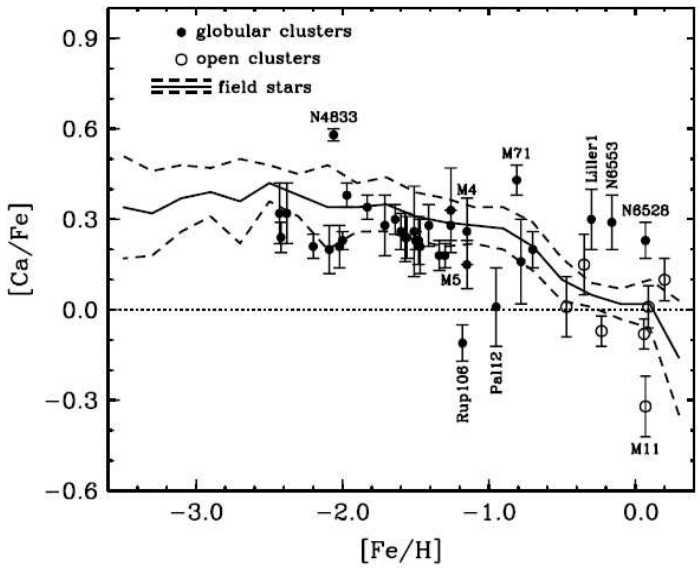

Figure 5.4: *Correlation with [Ca/Fe] abundance ratios with [Fe/H] in field and cluster stars. Each globular and open cluster point is the mean value for a single cluster. The lines representing the field-star trend with iron are averages of the abundances in 0.2 dex metallicity bins. The solid line shows the mean trend and the dashed lines indicate the scatter about the mean (from Sneden 2004).*

TiI and TiII

TiI and TiII (top and bottom panel in Fig 5.6) show a slightly increasing trend with a decreasing [Fe/H]. Due to the discrepancies that we have mentioned above they cannot be considered very reliable as indicators of the behaviour of the α elements as a function of the iron abundance. However we note that if we apply to TiI the correcting factor determined by Fulbright, TiI ratios present a trend more similar to Si and Ca behaviours. TiI and TiII ratios show a better agreement with Luck data than with Andrievsky's results, however we can note the discrepancies (in some cases quite large) of individual star between the abundances of the two ions in both the data sets adopted for the comparison. It is crucial to solve the problem of the discrepancies to be able to draw firmer conclusions about the behaviour of titanium as a function of iron.

O

In the top panel of Fig. 5.7, oxygen abundance ratios also present a increasing trend with decreasing iron abundance, reaching a value around 0.1±0.10 dex at [Fe/H]=−0.9. As for Si and Ca, this is in agreement with the theoretical prediction. Considering the other observational studies, we observe

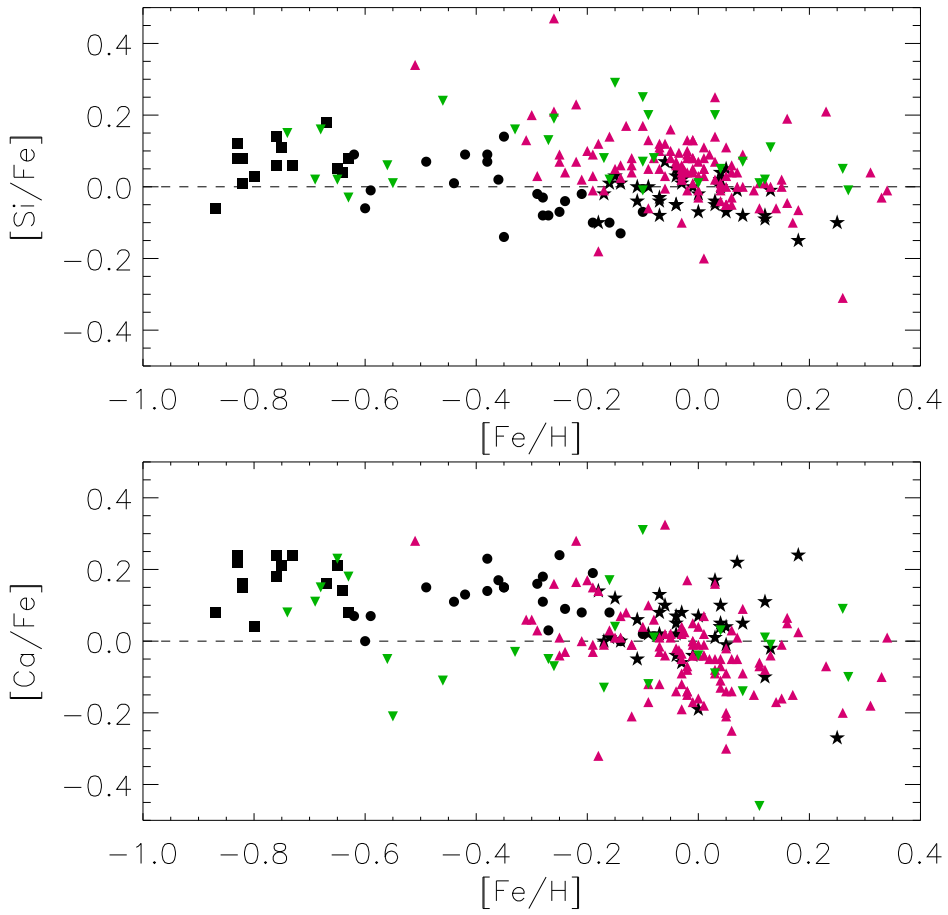

Figure 5.5: *The abundance ratios of Si and Ca are plotted as a function of [Fe/H]. The black squares, circles and stars indicate the abundance ratios of our SMC, LMC and Galactic Cepheids, respectively. The green upside-down triangles are data from Luck et al (1998). The large set of abundances obtained for Galactic Cepheids by Andrievsky's group (Andrievsky et al 2002a, 2002b, 2002c; Luck et al 2003) is indicated with purple triangles.*

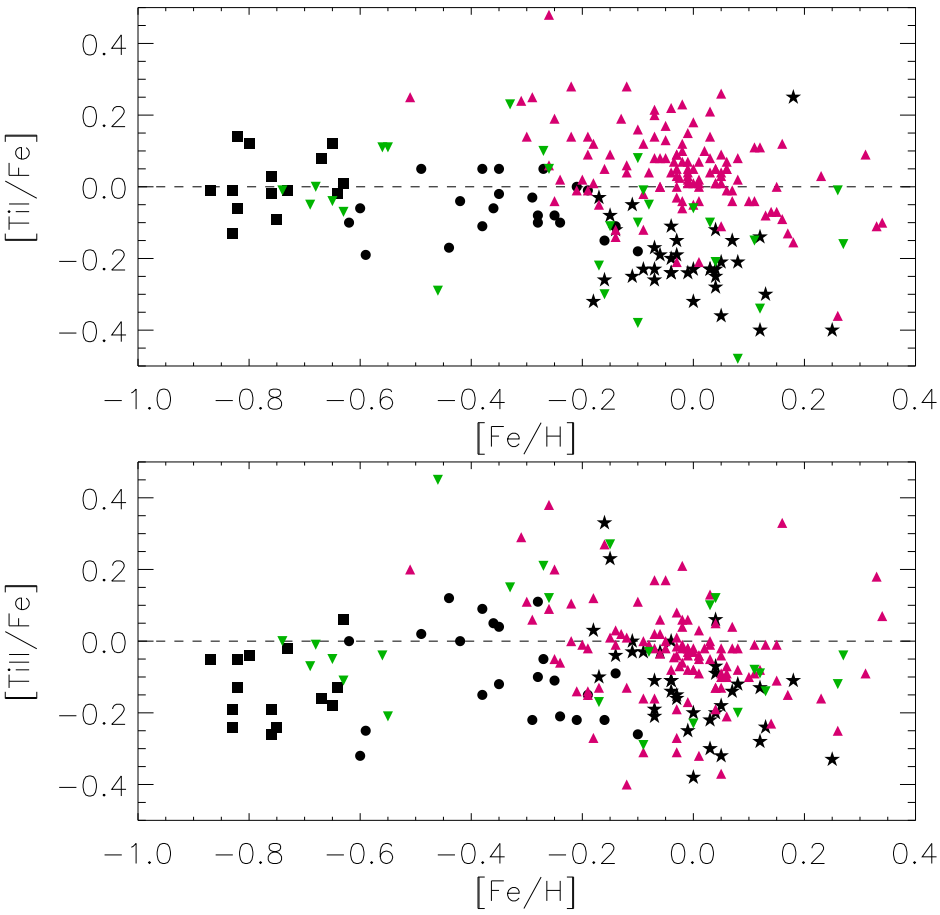

Figure 5.6: *The abundance ratios of TiI and TiII are plotted as a function of [Fe/H]. The black squares, circles and stars indicate the abundance ratios of our SMC, LMC and Galactic Cepheids, respectively. The green upside-down triangles are data from Luck et al (1998). The large set of abundances obtained for Galactic Cepheids by Andrievsky's group (Andrievsky et al 2002a, 2002b, 2002c; Luck et al 2003) is indicated with purple triangles.*

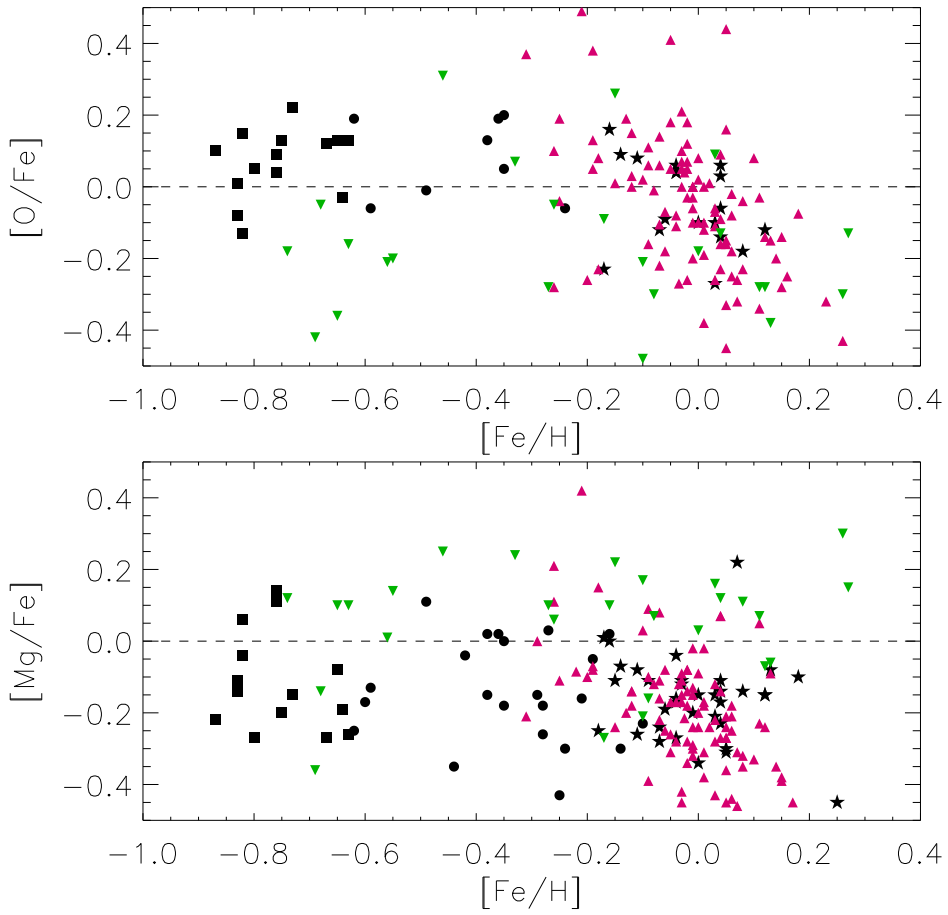

Figure 5.7: *The abundance ratios of O and Mg are plotted as a function of [Fe/H]. The black squares, circles and stars indicate the abundance ratios of our SMC, LMC and Galactic Cepheids, respectively. The green upside-down triangles are data from Luck et al (1998). The large set of abundances obtained for Galactic Cepheids by Andrievsky's group (Andrievsky et al 2002a, 2002b, 2002c; Luck et al 2003) is indicated with purple triangles.*

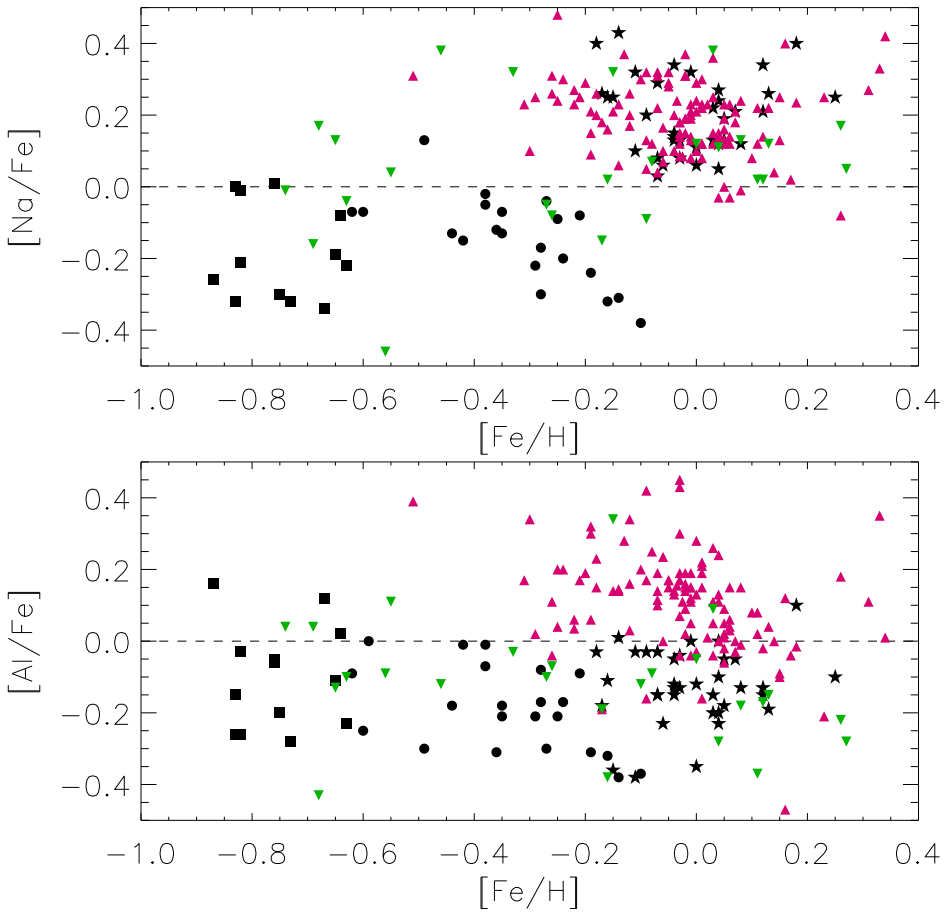

Figure 5.8: *The abundance ratios of Na and Al are plotted as a function of [Fe/H]. The black squares, circles and stars indicate the abundance ratios of our SMC, LMC and Galactic Cepheids, respectively. The green upside-down triangles are data from Luck et al (1998). The large set of abundances obtained for Galactic Cepheids by Andrievsky's group (Andrievsky et al 2002a, 2002b, 2002c; Luck et al 2003) is indicated with purple triangles.*

some differences with the Magellanic Cepheids of Luck's data set, their ratios are under-abundant compared to ours. There is, instead, a good agreement with the Galactic Cepheids analysed by Andrievsky and collaborators. Luck's oxygen abundances have been determined with the spectrum synthesis method as well but they used also the OI line at 6158 Å in addition to the [OI] forbidden lines. This line is among the OI lines in the optical that suffers of severe blending with other features as reported by Allende Prieto et al (2001), although Luck did not mention this problem and if or how it has been dealt with. The use of the OI line, then, may be responsible of errors on the final abundance obtained for each star. The Galactic supergiants observed by Luck also show [O/Fe] ratios slightly under-abundant respect to Andrievsky's and our results, in the same direction of the discrepancies noted for the Magellanic sample, indicating a possible systematic effect for the whole sample.

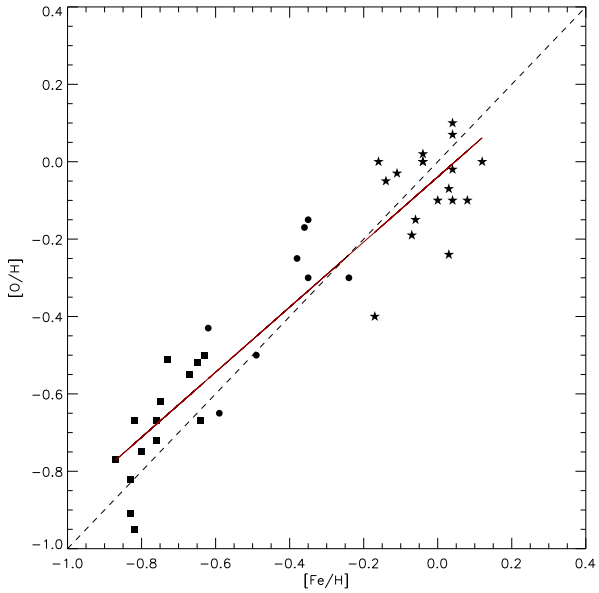

Figure 5.9: *Correlation between [O/H] and [Fe/H] for our sample of Cepheids. The solid purple line is the linear regression of the data and the dashed line indicate a relation with a slope of 1.*

In addition, for this element, we have also determined the correlation of its abundance relative to hydrogen as a function of iron (see Fig. 5.9), in order to test if [O/H] can be used as indicator of the metallicity instead of [Fe/H] for Cepheids star (e.g. in studies of the extragalactic distance scale, see next Chapter). We calculated a linear regression of our data and obtained a slope of 0.84 and a zero point of -0.04. We can conclude then that the oxygen abundance can approximate fairly well the iron abundance and they both can be reliable indicators of the metallicity for Cepheid stars.

Mg

The trend of Mg ratios (bottom panel in Fig. 5.7) is rather flat and shows that this element is under-abundant relative to the iron abundance. Our results for the Galactic Cepheids present a good agreement with Andrievsky data set, while are out of accord with Luck's abundance ratios, which are mostly overabundant. These discrepancies may be due to the choice of the lines adopted to determine the abundances, since the lines we have selected are all quite strong in Cepheid spectra (around 100 mÅ). Unfortunately, Luck et al did not publish their line list so it is not possible a comparison. However, Hill et al (1999) determined for 6 K supergiants in NGC 330 (a young cluster in the SMC) Mg abundance ratios between -0.23 and $+0.05$, in agreement with our under-abundant ratios.

Thus, to better understand the behaviour of [Mg/Fe] as a function of [Fe/H], it will be necessary a new analysis with additional Mg lines, possibly weak, to improve the accuracy of our results.

Na

The Na abundance ratios (top panel in Fig. 5.8)of our sample show two distinct trends: Galactic Cepheids show a plateau at a mean value around $+0.2$ dex, in very good agreement with Andrievsky's results and also with the Galactic supergiants studied by Luck; Magellanic Cepheis have under-abundant ratios that follow a flat trend, with a mean value around -0.13, while Luck results are around zero. This small difference is probably due to the different programs used to determine the abundances and set of model atmospheres, that usually is of the order of 0.1 dex. Hill et al (1999) observed a behaviour similar to our results in the 6 cool supergiants in NGC 330. Their abundance ratios vary between -0.30 and -0.02.

Al

Aluminium ratios are constantly under-abundant, with a mean value of ~ -0.14 dex, over the whole range of iron content of our sample of Cepheids (bottom panel in Fig. 5.8). This trend is in agreement with Luck data set, while the sample of Galactic Cepheids studied by Andrievsky and collaborators show overabundant [Al/Fe] ratios, with a mean value around $+0.15$ dex. Comparing the two analysis we are not yet being able to determine the reason of these differences. The analysis of K supergiants in NGC 330 by Hill et al gives Al ratios from -0.16 to $+0.02$ while the range found in a study of 10 giants in LMC globular clusters by Hill et al (2000) is between -0.43 to zero with two stars that show an overabundant ratio. These studies indicate that nonvariable supergiants (with [Fe/H] between -1.8 and -0.45 dex) have under-abundant values of the Al ratios in agreement with what we have found for our sample of Magellenic Cepheids.

5.2.2 Preliminary conclusions

Our analysis of the α element still needs improvements and refinements and a more detailed comparison with theoretical predictions for each element to better investigate the gas enrichment history that led to the formation of Cepheids.

However we can draw some preliminary conclusion considering oxygen, silicon and calcium as the most reliable indicators among the α elements we have analysed (see Fig. 5.10). The trends of the abundance ratios of these elements are in fairly good agreement with observational studies on Cepheids and on different kind of stellar population in the Galaxy and the Magellanic Clouds. Furthermore they agree with the theoretical predictions for the trend of [α/Fe] by Matteucci (2003).

Studying the correlation between [O/H] and [Fe/H] we can say that oxygen is a good indicator of iron content, i.e. of the metallicity, and it can be used to investigate its effect on the Cepheid PL relation.

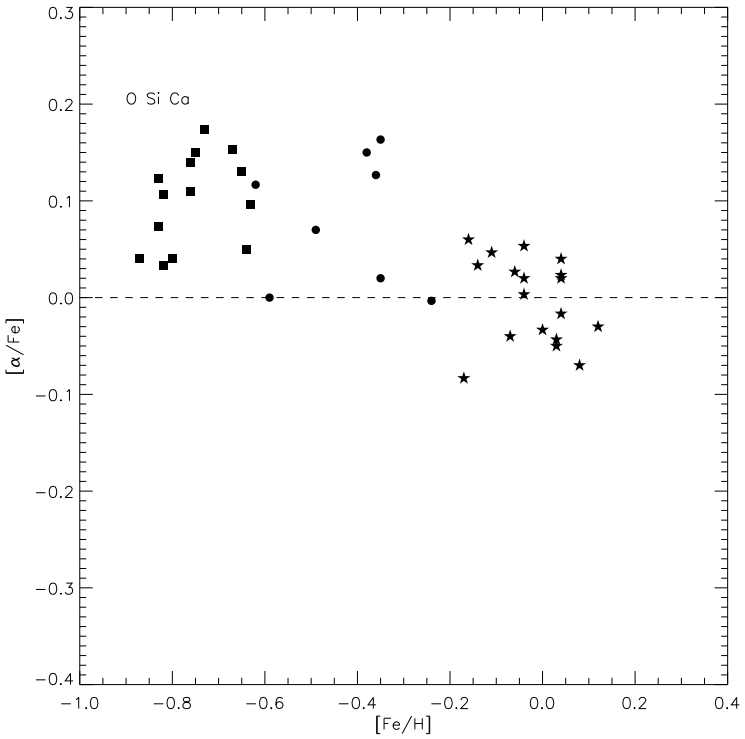

Figure 5.10: *[α/Fe] as a function of [Fe/H] using oxygen, silicon and calcium as the most reliable indicators among the α elements we have analysed.*

Chapter 6

The effect of the metallicity on the PL relation

The effect of the metallicity on the Cepheid PL relation has been a matters of conjectures and debate for several years from a theoretical and an observational point of view, as we have already discussed in section 1.6.

Using the iron abundances that we have determined for our sample of Galactic and Magellanic Cepheids, we investigate this effect in the V and K bands. Our test in these two bands aims to verify if there is a change of the influence of the metallicity as wavelength increases, since theoretical models by Bono et al (1999) predict a smaller effect in the infrared bands than in the optical one. Our sample of stars covers a range in metallicity of about 1 dex (see section 4.1), allowing us to use a rather wide baseline.

We determine PL relations using all the stars with magnitudes corrected for the reddening effect (see Table 2.1 and 2.2) and with periods between 3 and 70 days. This selection in period has been done following theoretical results from Bono et al (1999) that show a linear behaviour of the PL relations up to $\log P = 1.8$. Above this value (i.e. in the region of long period Cepheids) the PL relations start to bend due to the shift of the instability strip towards redder colours (see in Fig. 1.4 the shape and position of the instability strip in the HR diagram).

We then use for our study of the PL relation 60 out of 72 stars.

Figure 6.1 shows the linear regressions we have obtained for our sample of Cepheids in B, V and K bands. We can see the decrease of the intrinsic scatter from the blue band to the infrared band as show in section 1.4. We also note that the short-period end of these relations (i.e. below $\log P = 0.9$) is less populated, this is due to an effect of selection in magnitude: only the brightest SMC Cepheids (i.e. with long periods) have been observed. We choose for our analysis the V and K bands, as representative of the optical and infrared ranges of wavelengths.

To investigate the effect of the iron content on the PL relations in the V and K bands we have adopted the following approach: we calculate the residuals in both bands, $\delta(M_V)$ and $\delta(M_K)$, as the difference of the absolute magnitude of our Cepheids and the absolute magnitude determined from the standard PL relations of Freedman et al (2001) and Persson et al (2004), respectively.

We have adopted these relations as point of reference because they are among the most recent observational results in the current literature and are determined from large samples of stars of the Large Magellanic Cloud, which is the first rung of the extragalactic distance ladder.

The absolute magnitudes of our Cepheids are determined from the observed magnitudes (corrected for the reddening effect, see Chapter 2) and the distance of the star, as follows:

$$M = m - \log D + 5$$

where m is the apparent magnitude, M is the absolute magnitude and D is the distance of the star. The quantity $\mu = m - M$ is called distance modulus. The absolute magnitudes used as reference are calculated from standard PL relations mentioned above in the V and K band using the pulsational period of our programme stars.

Then we study the trends of the V-band and the K-band residuals as a function of the iron abundance. $\delta(M_V)$ and $\delta(M_K)$ are, effectively, the corrections to be applied to a standard PL relation as a function of the iron content.

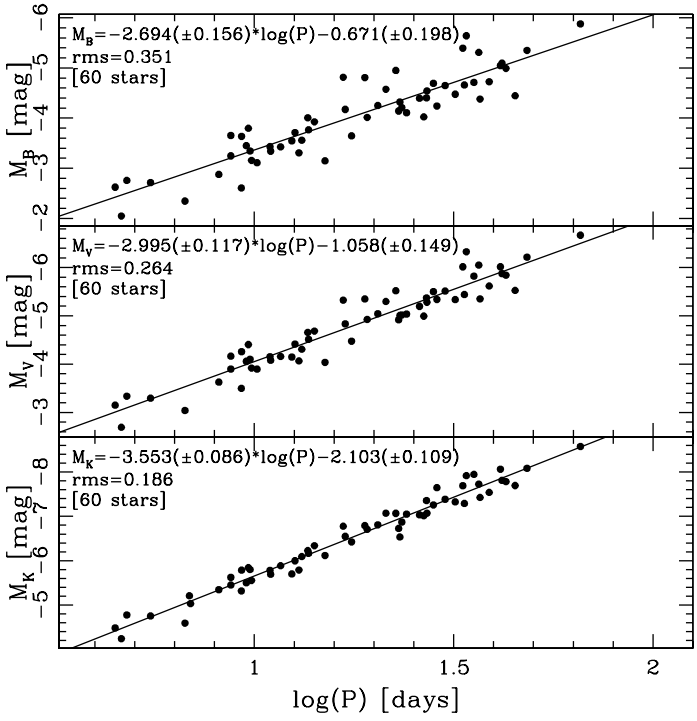

Figure 6.1: *PL relations determined for our sample of Cepheids in the B, V and K bands (top, middle and bottom panel, respectively). The decrease of the intrinsic scatter with the increase of the filter can be see.*

6.1 The adopted standard PL relations

As we have already mentioned in Chapter 1 the LMC is the first rung of the extragalactic distance ladder and its Cepheid PL relations are widely used as standard relations to determine distances or calibrate secondary distance indicators. The advantages of using this galaxy as testbed are the following:

- it is near enough so that Cepheid are bright enough for accurate photometry even with small telescopes;
- it has little depth along the line of sight (i.e. it is a fair approximation to use its distance for its Cepheids, van der Marel & Cioni 2001);
- the foreground Galactic extinction towards it is low;.

Freedman et al (2001) and Persson et al (2004) have both adopted as distance modulus of the LMC the value of 18.50 mag (i.e. 50 kpc), in agreement with the most recent results about the distance of this galaxy (see Chapter 2).

The PL relation in the V band by Freedman and collaborators is:

$$M_V = -2.760[\pm 0.03] \cdot (\log P - 1) - 4.218[\pm 0.02] \tag{6.1}$$

where M_V is the absolute magnitude in the V band and P is the period, with rms=$\pm$0.16. They have calculated it from a sample of 650 LMC Cepheids from the Optical Gravitational Lensing Experiment database (OGLE, Udalski et al 1999) with well-determined mean magnitudes in B, V and I band and periods between 2 and 32 days.

Persson and collaborators determined the PL relation in the K band from 92 LMC Cepheids, with periods between 3 and 100 days. For this sample of stars they have accurate J, H and K mean magnitudes and reddenings. Their result in the K band is :

$$M_K = -2.449[\pm 0.05] \cdot \log P - 3.281[\pm 0.04] \tag{6.2}$$

where M_K is the absolute magnitude in the K band and P is the period, with rms=$\pm$0.11.

The infrared data obtained by Persson et al are on the LCO (Las Campanas Observatory) photometric system[a] (Persson et al 1998) while the infrared data for our sample of Cepheids are on the SAAO (South Africa Astronomical Observatory) photometric system (Carter 1990; Carter & Meadows 1995). The K_s band in the LCO system is 0.32 μm wide and it is centred at 2.16 μm, it is called *short* because it has a cut-off at $\sim$2.3 μm in order to reduce the noise contribution from the thermal background. Thus observation in this band are less sensitive to variation in the ambient

[a]The infrared photometric systems are less well-standardised than systems in the optical and each observatory will often define its own system which differs slightly from the others. These differences arise because the atmospheric windows, which are transparent at infrared wavelengths, are themselves different at different observatories and, in particular, vary with altitude.

temperature. The K band in the SAAO system is centered at 2.2 μm with a width of 0.70 μm. To avoid systematic differences we decided to transform both systems in the 2MASS (Two Micron All Sky Survey) system, since this survey provides photometry for million of galaxies and nearly a half-billion stars over the entire sky and represents an important point of reference. We utilise the following colour transformations calculated by Carpenter (2001) for the LCO system:

$$(K_s)_{2MASS} = (K_s)_{LCO} + (-0.002 \pm 0.002)(J - K_s)_{LCO} - 0.010 \pm 0.004 \tag{6.3}$$

and the SAAO system:

$$(K_s)_{2MASS} = K_{SAAO} + (0.020 \pm 0.007)(J - K)_{SAAO} - 0.025 \pm 0.006 \tag{6.4}$$

6.2 Results

To assess the effect of the metallicity we have to divide our sample of Cepheids into bins of metallicity. The choice of the number of bins is crucial because more bins one adopts more details can be unraveled about this effect, but it is also essential to use a statistical significant number of stars to well populate the PL relation in each bin. We decided to separate our stars in two bins that have different sizes but the same number of objects. Each bin contain 30 Cepheids and has an average metallicity about -0.50 dex (metal-poor bin) and about solar. We chose this approach after several simulation (see section 6.3 for more details) to test the level of incompleteness of a sub-sample of a population of Cepheids. Utilising two bins, we have a number of stars, that cover a wide range of periods, high enough to determine a PL relation that approximate well the PL relation of the complete population of Cepheids in each bin (i.e. range of metallicity).

6.2.1 The effect of iron content

Firstly we studied the effect of the iron content alone since it is one of the most used indicator of the metallicity (its lines are present in large numbers and are easy to detect in stellar spectra). As we have shown in Chapter 4, oxygen in this kind of stars is a good tracer of the iron abundance (the slope of their correlation is $\sim$1) and, then, of the metallicity, thus the results present below obtained for the iron content are very similar to the ones determined for [O/H] alone.

Our results for the V and K bands are presented in Fig 6.2 and Fig 6.3, respectively.

In the top panels of Fig 6.2 are shown the PL relations in the V band calculated (linear regression) in each bin. In each panel are also indicated the average iron content of the bin, the root mean square of the linear regression and the number of stars. The bottom panels show:

- **left hand panel**: the slope of the PL relation calculated in each bin as a function of the iron abundance we have derived from the FEROS and UVES spectra; the filled squares represent the mean values and the vertical error-bars are the errors on the mean, the solid line is the value of the slope of the standard PL relation adopted as reference;

- **middle panel** : the zero point (ZP) of the PL relation calculated in each bin as a function of [Fe/H]; the filled squares represent the mean values and the vertical error-bars are the errors on the mean, the solid line is the value of the zero point of the standard PL relation adopted as reference;
- **right hand panel**: the residuals $\delta(M_V)$, determined as we have explained above, as a function of [Fe/H]; the filled squares represent the mean values and the vertical error-bars are the errors on the mean, the solid line is the null value which corresponds to an independence of the PL relation from the iron content.

The horizontal bars indicate the size of the bins in all the panels..

Analogous panels in Fig 6.3 show the PL relations calculated in the two bins (top panels) and the trends (bottom panels) of slope, ZP and residuals as a function of the iron abundances in the K band.

From the simulation we have carried out (see Fig. 6.6) we note that the slope and the zero point are correlated, thus their trends with [Fe/H] are correlated too. The net effect of the iron content on the PL relation is given by the residuals δ. A positive δ means that the luminosity of a Cepheid is fainter than the one obtained with the standard PL relation. Of course for LMC Cepheids the residuals are zero by definition, since the standard PL relations have been calculated with LMC stars, but the metal-poor bin include also SMC Cepheids that have a lower average metallicity.

Considering the V-band (Fig 6.2) the slope of the PL relation increases with the iron content (bottom left panel) while the zero point increases (bottom middle panel). The mean values of $\delta(M_V)$ in both bins are positive and there is an increasing trend with the iron content, this means that metal-rich Cepheids are fainter than metal-poor ones at a fixed period.

On the contrary, for the K band (bottom panels in Fig 6.3), we observe a flat trend of $\delta(M_K)$ around zero, because slope and zero point show opposite behaviours: a steep decrease and a steep increase with [Fe/H], respectively. Thus, as net effect, there is no change in the luminosity of Cepheids as the iron content increases. In this band then, [Fe/H] has a large effect on the slope and the zero point but the net effect on the PL relation is neglegible and, since the reddening effects are minimised too, it is the best band in which we can use the PL relation to determine distances. Moreover, as we have already mentioned in section 1.6, Bono et al (1999) predicted that the effect of the metallicity decreases with increased wavelength (i.e. the dependence is milder in the infrared bands) and our data confirm this behaviour.

6.2.2 The effect of the estimated total metallicity

As a second step, we studied the effect of the total metallicity that we have estimated as the sum of the iron, oxygen, silicon and calcium abundances. As we have explained in Chapter 5, O, Si and Ca are the most reliable indicators among the α elements we have analysed. In this way we test if the contribution of light elements changes the effect of the chemical composition on the PL relation.

Since we were able to determine the oxygen abundances only for 40 Cepheids of our sample, we determined the values of [O/H] for the other stars from the correlation with the iron abundance

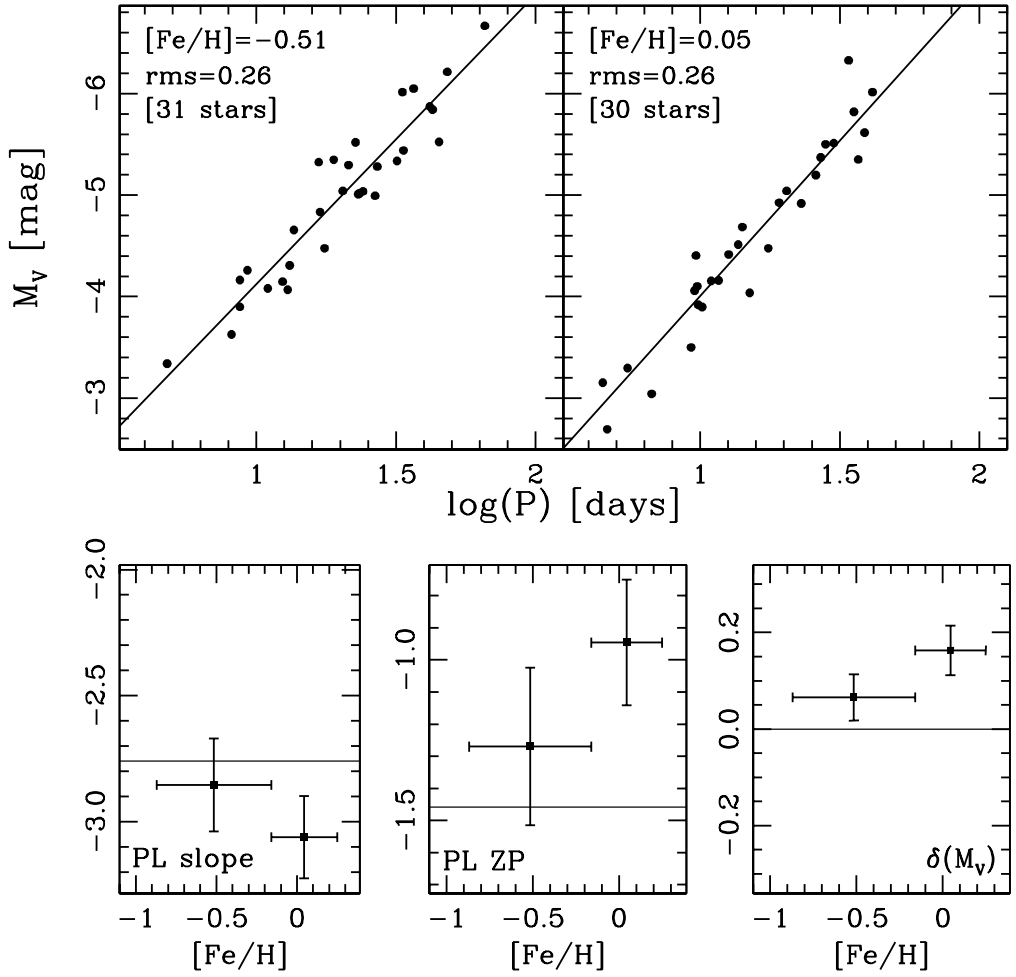

Figure 6.2: *The top panels show the PL relations calculated in each bin for the V band. The bottom panels show, from left to right, the PL slope, the PL zero point and the residuals $\delta(M_V)$, respectively, as a function of the iron abundance. The mean values of the PL slope, the PL zero point and $\delta(M_V)$ in each metallicity bin are plotted as filled squares, with the vertical error-bars representing its associated error. The horizontal bars indicate the dimension of the bins. The horizontal solid lines indicate the values of the slope and zero point of the standard PL relations and the null value which corresponds to an independence of the PL relation from the iron content.*

and used them in the estimate of the total metallicity for each star.

Our results in the V and K band are shown in Fig 6.4 and Fig 6.5, respectively. The panels in both figures are analogous to the panels in Fig 6.2 and Fig 6.3, presenting the PL relations

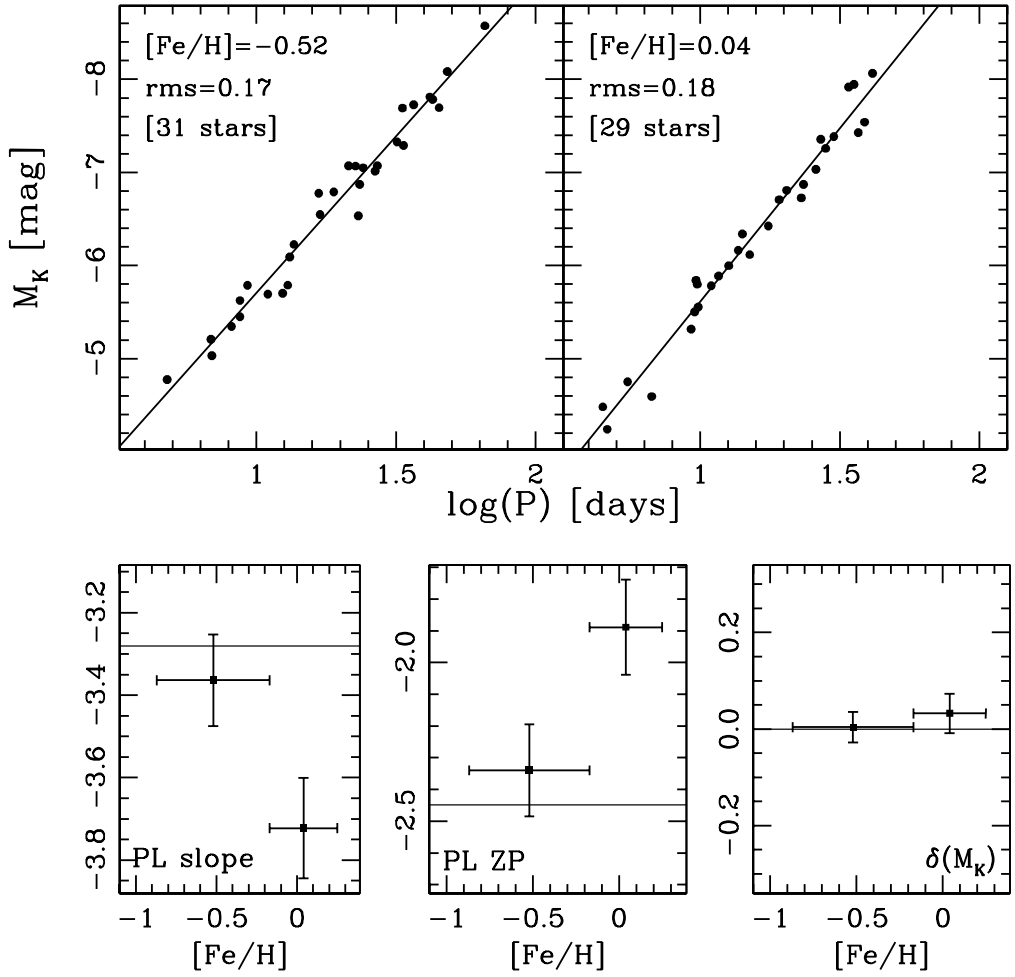

Figure 6.3: *The top panels show the PL relations calculated in each bin for the K band. The bottom panels show, from left to right, the PL slope, the PL zero point and the residuals $\delta(M_K)$, respectively, as a function of the iron abundance. The mean values of the PL slope, the PL zero point and $\delta(M_K)$ in each metallicity bin are plotted as filled squares, with the vertical error-bars representing its associated error. The horizontal bars indicate the dimension of the bins. The horizontal solid lines indicate the values of the slope and zero point of the standard PL relations and the null value which corresponds to an independence of the PL relation from the iron content.*

calculated in each bin and the trends of the slope, ZP and residuals of the magnitude as a function of [M/H] instead of [Fe/H].

Comparing these results to the previous one obtained for the iron abundance alone we note that

the trends of the slope and the ZP become steeper and the residuals show a very small change in the bin at solar metallicity. Considering then the net effect from the residuals, the total metallicity that we have estimated have a slightly larger effect on the PL relation in the V band than the effect due to the iron abundance alone. In the K band we still observe a neglegible net effect but larger effects on the slope and ZP.

This shows that a detailed chemical analysis of Cepheids is needed to precisely evaluate the metallicity effect on the PL relation.

This result will be greatly improved once the problems that affect the other α elements we have analysed will be solved. We will be able to estimate the total metallicity from all the α elements and the iron.

6.3 Uncertainties

We have already discussed in section 1.4 that the PL relation is a statistical relation and it provides the average of the Cepheid absolute magnitudes as a function of the period. It has an intrinsic scatter correlated to the finite width of the instability strip, which decreases with increased wavelength from 1.2 mag to 0.5 mag from B band to K band (see Fig. 1.7). Thus it is crucial to observe a number of stars that well-sample the instability strip to calibrate the PL relation and it has to be done in every metallicity bin to accurately evaluate the effect of the iron content.

To check the reliability of our results we carry out several simulations, in order to understand if the selection of Cepheids we have done to assemble our sample can affect in some way our conclusions about the effect of the iron abundance on the PL relation. We extract randomly several times a subsample of stars from a sample of observed Cepheid that populate well the PL relation. We choose as reference a sample of 771 LMC Cepheids from the OGLE database (Udalski et al 1999) for the test in the V band and the sample of 92 LMC Cepheids (Persson et al 2004) for the test in the K band. The latter is the larger observed sample of Cepheids in the infrared bands.

We extract different subsample (e.g. 15, 20, 30, 100 stars) to test how well the resulting PL relation approximates the PL relation of the complete population of stars and to decide how to divide our sample of Cepheids in bins of metallicity. Considering the total number of Cepheids we can use to assess the effect of the iron content, which is 60, and the results of the simulation, the best approach is to separate in two subsample of 30 stars.

Figure 6.6 shows two examples (V band) of 500 extractions of a sample of 30 stars and of a sample of 100 stars. For each extraction a linear regression is performed to derive the slope and zero point of the PL. These pairs of slope and ZP are, then, plotted against each another, showing a correlation of the two quantities. Slope and ZP of the underlying PL are reported as thin vertical and horizontal lines, respectively. The top and right small panels in Fig 6.6 show the histograms of the resulting distributions of slope and ZP. The two different simulations show that the errors on the slope and ZP of the extracted subsample decrease as the number of stars of the latter increases, in fact the scatter of the slope-ZP relation and of their distributions decreases.

From our simulations we can draw the following conclusions:

- the number of 30 Cepheids per bin is not enough to accurately characterise the Cepheid PL

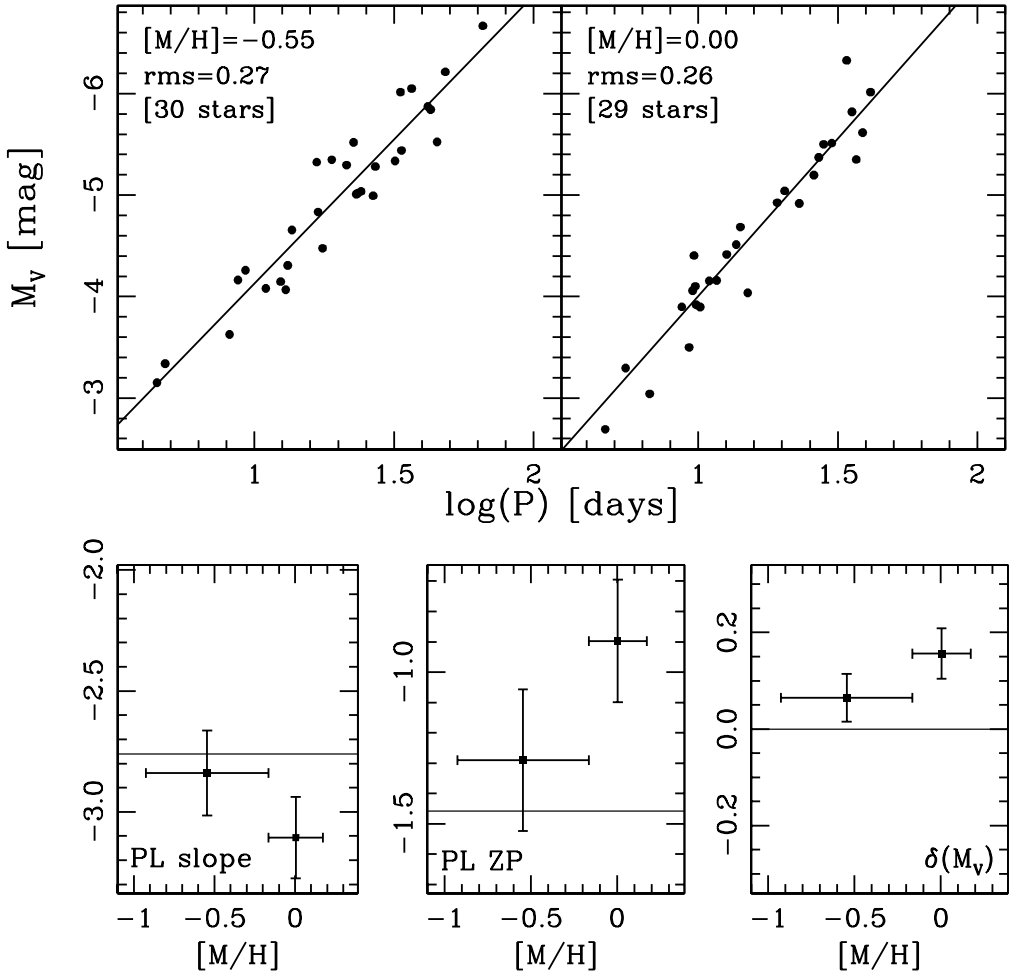

Figure 6.4: *The top panels show the PL relations calculated in each bin for the V band. The bottom panels show, from left to right, the PL slope, the PL zero point and the residuals $\delta(M_V)$, respectively, as a function of the estimated total metallicity [M/H]. The mean values of the PL slope, the PL zero point and $\delta(M_V)$ in each metallicity bin are plotted as filled squares, with the vertical error-bars representing its associated error. The horizontal bars indicate the dimension of the bins. The horizontal solid lines indicate the values of the slope and zero point of the standard PL relations and the null value which corresponds to an independence of the PL relation from [M/H].*

relation but allows us to obtain some qualitative indications on the effect of the iron content;

- the increasing trend of the V-band residuals $\delta(M_V)$ as a function of the iron content is real

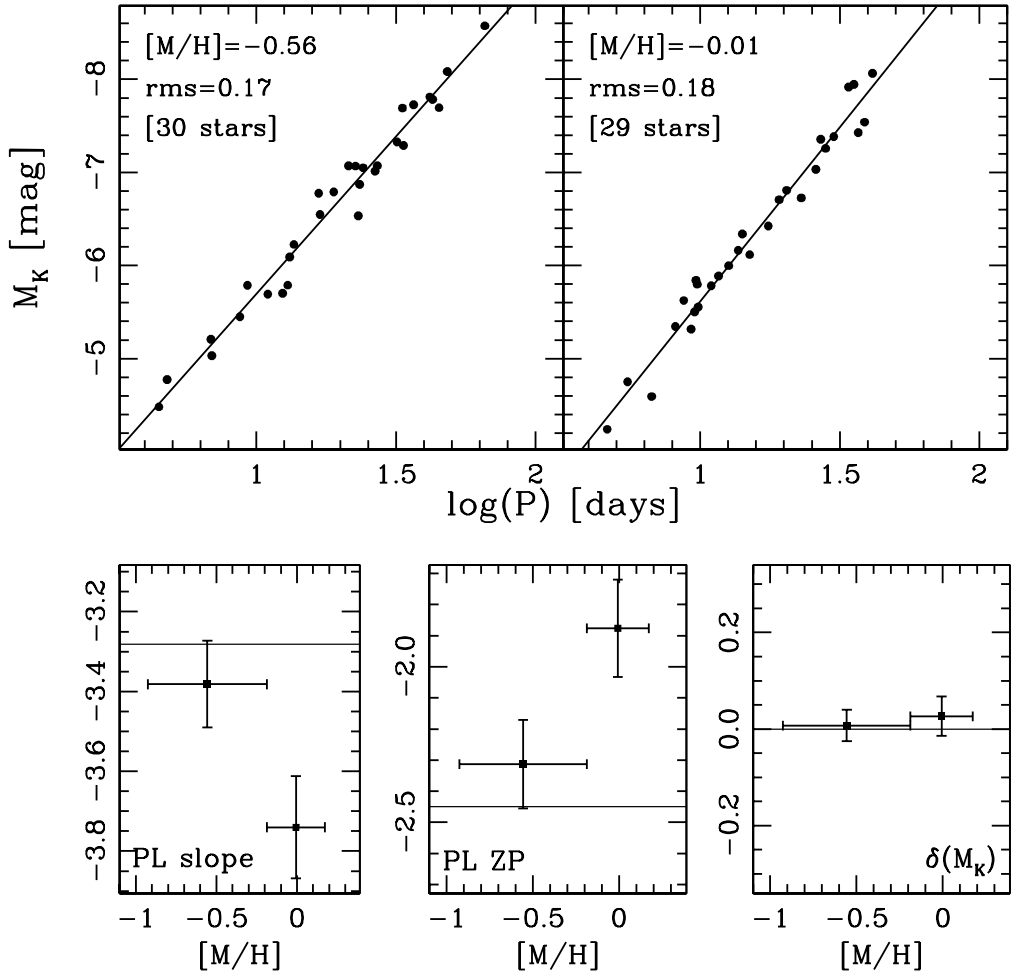

Figure 6.5: *The top panels show the PL relations calculated in each bin for the K band. The bottom panels show, from left to right, the PL slope, the PL zero point and the residuals $\delta(M_K)$, respectively, as a function of the estimated total metallicity. The mean values of the PL slope, the PL zero point and $\delta(M_K)$ in each metallicity bin are plotted as filled squares, with the vertical error-bars representing its associated error. The horizontal bars indicate the dimension of the bins. The horizontal solid lines indicate the values of the slope and zero point of the standard PL relations and the null value which corresponds to an independence of the PL relation from [M/H].*

with a confidence level of 99%, and not due to "bad" sampling of the instability strip, since the distribution of the residuals with respect to the underlying PL relation for 30 stars shows that only the 1% is greater than 0.13 mag, thus the uncertainties due to the number of stars

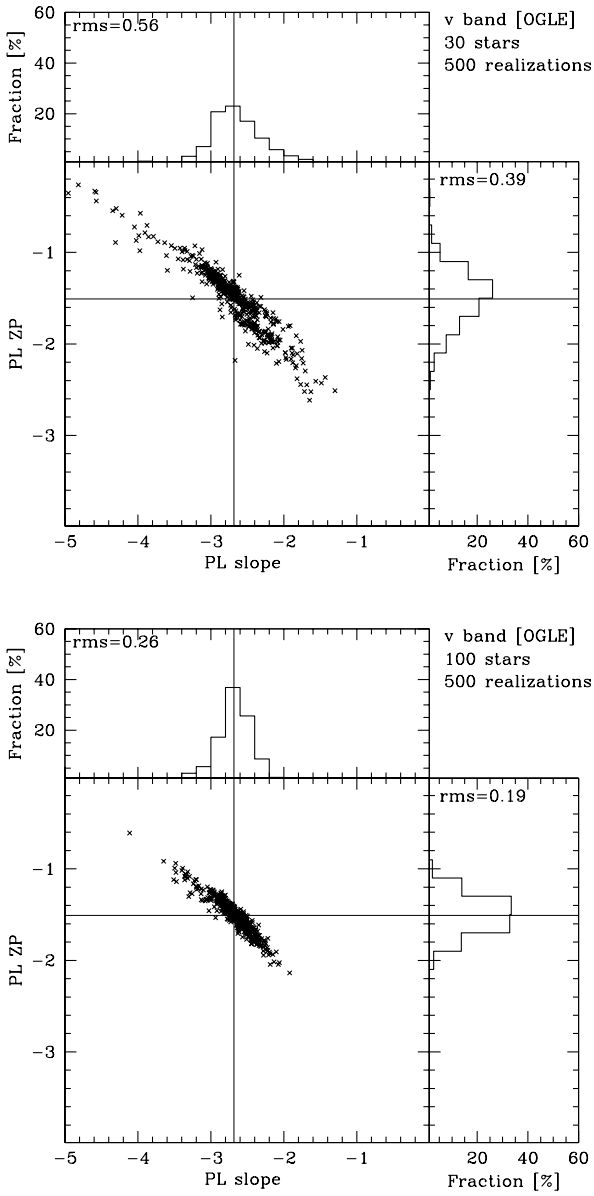

Figure 6.6: *In the Figure are shows two examples (V band) of 500 extractions of a sample of 30 stars (top panel) and of a sample of 100 stars (bottom panel). For each extraction a linear regression is performed to derive the slope and zero point of the PL. These pairs of slope and ZP are, then, plotted against each another. Slope and ZP of the underlying PL are reported as thin vertical and horizontal lines, respectively. The top and right small panels show the histograms of the resulting distributions of slope and ZP.*

used are much smaller than the effect observed on the V-band residuals;

- a sample of 100 star per bin evenly distributed in the linear part of the PL relation is needed to determine with a high accuracy (0.02 mag) the effect of the iron content, this implies an uncertainty in distance of 1%.

6.4 Comparison with previous results

We compare our results with two different behaviours (see Fig. 6.7) as examples of the effects of the metallicity on the PL relation currently reported in the literature (see section 1.6): independence from the iron contenent and a monotonic decreasing trend (e.g. Kennicutt et al. 1998; Sakai et al. 2004; Storm et al. 2004; Groenewegen et al. 2004), in the sense that metal-rich Cepheids are brighter than metal-poor ones. Many of these studies use [O/H] as tracer of the metallicity (see Table 1.1 and Fig. 1.9) and, since we have shown that [O/H] and [Fe/H] correlate, our comparison with respect to the iron content is reasonable.

We use for the comparison the classical results of Kennicutt et al (1998) adopted by HST Key Project to determine extragalactic distance with Cepheids (Freedman et al 2001). They have analysed two Cepheid fields in M101[a], with average values of metallicity around -0.4 dex and 0.28 dex (determined from measurements of oxygen in H II regions[b] in the two fields). They have observed 29 Cepheids in the outer field (low metallicity) and 61 Cepheids in the inner field (high metallicity) with periods between 10 and 60 days. Considering the outcome of our simulations, the two samples of stars observed by Kennicutt and collaborators are comparable to our sub-samples in each bin, it is then reasonable to compare the qualitative indications about the effect of the metallicity that can be derived from the two analyses.

The complete comparison is possible only in the V-band, since there are no data available for the monotonically decreasing $\delta(M)$ hypothesis in the K-band.

For the comparison with the two hypothesis mentioned at the beginning of this section we adopted the χ^2 technique[c].

V-band case

[a] Messier Object 101 or NGC 5457 is a spiral galaxy in the constellation Ursa Major. Its distance is about 9 Mpc and it is the brightest member of the M101 group of galaxies.

[b] An H II region is a cloud of glowing gas and plasma in which star formation is taking place. H II regions are named for the large amount of ionised atomic hydrogen they contain.

[c] This method is the most used member of the nonparametric family of statistical tests. The χ^2 is employed to test the difference between an actual sample and another hypothetical or previously established distribution such as that which may be expected due to chance or probability. χ^2 can also be used to test differences between two or more actual samples. Its general form is:

$$\chi^2 = \Sigma \frac{(Observed\,frequency - Expected\,frequency)^2}{Expected\,frequency}$$

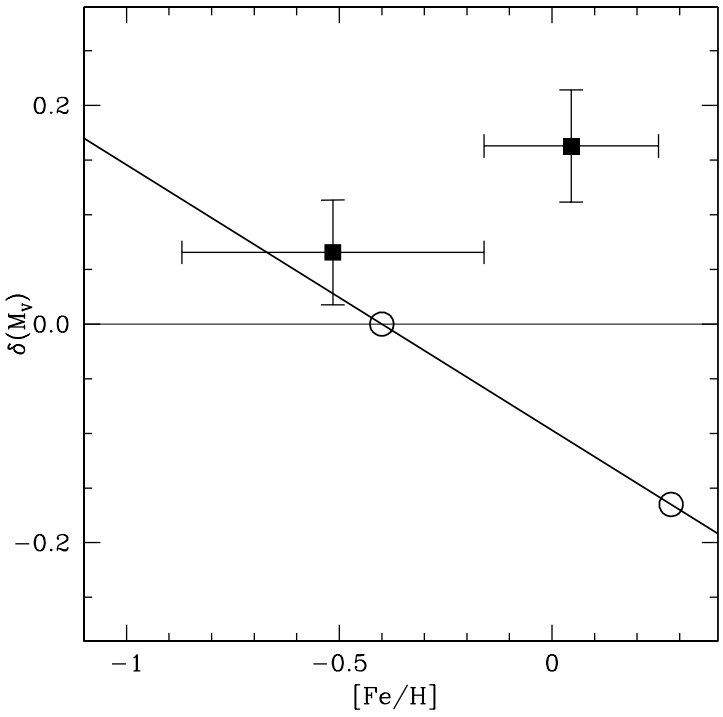

Figure 6.7: *The V-band residuals compared to Freedman et al. (2001) PL relation are plotted against the iron content measured from observed spectra (bottom right panel in Fig 6.2). The filled squares represent the mean value in each metallicity bin, with its associated errorbar. The metallicity dependence as inferred by Kennicutt et al. (1998) from two Cepheid fields in M101(open circles) is shown as a full line.*

- **No dependence of $\delta(M_V)$ on [Fe/H]**: the χ^2 test gives a value of 12.0. This means that we can exclude this hypothesis at the 99.99% level.
- **Monotonically decreasing $\delta(M_V)$**: we compare the classical results of Kennicutt et al. (1998, open circles and solid line in Fig. 6.7) with our data. The outcome of the χ^2 test is 28.6, meaning that this hypothesis is incompatible with our results with a confidence higher than 99.99%.

K-band case

No dependence of $\delta(M_K)$ on [Fe/H]: the χ^2 test gives values of 0.7, this means that there is a good agreement with our data so the metallicity has no effect on the PL relation in the K-band.

To conclude, we note different behaviours in the two bands. We observe an increasing trend of the V-band residuals with the iron content. This result, simply regarding the outcomes of χ^2 test,

is in disagreement with an independence of the PL relation on iron abundance and with the linearly decreasing trend found by observational studies in the literature (e.g. Kennicutt et al 1998). The K-band result, instead, perfectly agrees with the hypothesis of no dependence of the PL relation on the iron content.

It is also important to add that our result for the estimated total metallicity in the V band is in the sense that metal-rich Cepheids are fainter then metal-poor ones in agreement with the outcome of theoretical non-linear convective models (e.g. Bono et al 1999; Fiorentino et al 2002; Marconi et al 2005) and at variance with the linear radiative models (e.g. Chiosi et al 1992; Sandage et al 1999; Baraffe & Alibert 2001). However, as we have determined from the simulation, a far larger sample of Cepheids with individual determinations of the elemental abundances (in order to estimate the total metallicity) is needed to put tight constraints to the theoretical models.

6.5 LMC distance: "short" vs "long" scale

We have discussed in Chapter 1 and Chapter 2 that the distance of the LMC is crucial to calibrate the PL relation and that, regrettably, we can find in the current literature values of the distance modulus ranging from 18.1 mag to 18.8 mag, not always obtained with different techniques. Those studies finding a distance modulus less than 18.5 support the so-called "short" distance scale, whereas those finding it greater than 18.5 support the "long" distance scale (for a review of the results and methods see Benedict et al. 2002; Gibson 2000). Because of this range, it is interesting to study the different behaviour of the PL relation depending on the adopted LMC distance scale. In order to do that, we have repeated our calculation of the V-band and K-band residuals assuming as distance modulus of the LMC (μ_{LMC}) the values of 18.3 (representative of the "short" scale) and of 18.7 (for the "long" scale). The results are shown in Fig. 6.8.

In the right hand panels, the V-band residuals are plotted for the short and long distance scale cases (top panel and bottom panel, respectively). $\delta(M_V)$ monotonically increases with the metallicity from a negative value up to a positive value at solar metallicity for a μ_{LMC} of 18.7. On the other hand for a μ_{LMC} of 18.3, the V-band residuals show a slightly decrease or a plateau, it is not possible to distinguish between the two possibility due to the size of the errors. With respect to the "long" scale, the data trend is slightly steeper than the one obtained with μ_{LMC}=18.5 and start at a negative value of $\delta(M_V)$. Using again a χ^2 technique, we find that this result is in disagreement with an independence of the PL relation on iron abundance and with the linearly decreasing trend often found in the literature (e.g. Kennicutt et al. 1998). With respect to the "short" scale, $\delta(M_V)$ presents a plateau or slightly decreases. This trend is quite different from the one obtained with μ_{LMC}=18.5, the effect of the iron content is in the same direction but stronger, in particular for stars at sub-solar metallicity. Also this result disagrees with an independence of the PL relation on the iron abundance and the monotonic decreasing behaviour at the 99.99 % level (utilising the χ^2 method).

The K-band residuals are reported in the left hand panels for the two cases. For a μ_{LMC} of 18.3 (top panel) we observe a decreasing trend with [Fe/H]. For the "long" distance scale (bottom panel) $\delta(M_K)$ monotonically increases up to solar metallicity. We note quite different behaviours, considering the two distance scale. For the "short" scale case, the luminosity's residuals present

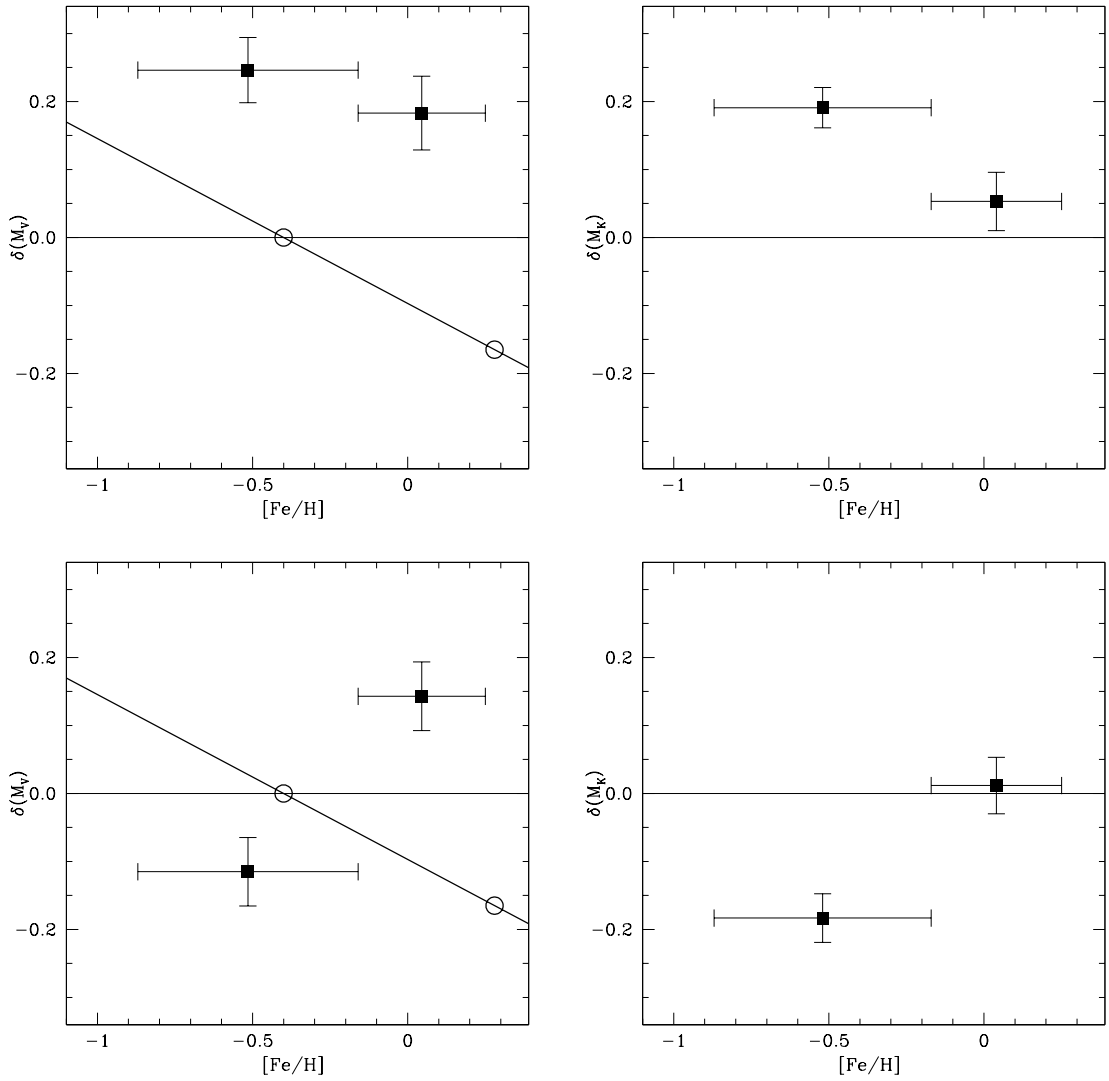

Figure 6.8: *In the right hand panels, the V-band residuals compared to Freedman et al. (2001) PL relation are plotted against the iron content measured from observed spectra, assuming a LMC distance modulus of 18.3 (top) and of 18.7 (bottom). The filled squares represent the mean value in each metallicity bin, with its associated errorbar. The metallicity dependence as inferred by Kennicutt et al. (1998) from two Cepheid fields in M101 (open circles) is shown as a full line. In the left hand panels, the K-band residuals compared to Persson et al. (2004) PL relation are plotted against the iron content measured from observed spectra, assuming a LMC distance modulus of 18.3 (top) and of 18.7 (bottom). The filled squares represent the mean value in each metallicity bin, with its associated errorbar.*

a decrease, this means that the iron content has an effect on the PL relation in the K-band, at variance with the result for μ_{LMC}=18.5 and it is more pronounced at sub-solar metallicity. For the "long" scale case, we observe a monotonic increase of $\delta(M_K)$ with [Fe/H] and, again, the data present an effect of the metallicity on the PL relation in the K-band but in the opposite direction of the one obtained considering μ_{LMC}=18.3. The results of the χ^2 method allow us to conclude that both behaviours are incompatible with the hypothesis of no dependence of the PL relation on the iron content at the 99.99% level.

We have said in Chapter 1 that the most recent determinations of the LMC distance are converging towards a common value around 18.5, so such distances of LMC as 18.3 and 18.7, nowadays, seem less probable (e.g. Romaniello et al. 2000; Carretta et al. 2000a; Walker 2003; Borissova et al. 2004). Thus we can consider the results obtained with μ_{LMC}=18.5 as a point of reference.

6.6 Future steps

We have concluded, from the outcome of our simulations, that a sample of 100 Cepheids evenly distributed in periods is needed to calibrate the PL relation and to constrain the effect of the iron content on it with high accuracy (0.02 mag). This number of stars is needed in each bin of metallicity and to discern much finer details, such as a non-monotonic trend, it will be really useful to consider at least 4 bins in the range of iron abundance we have studied ($-0.9 \leq$ [Fe/H] ≤ 0.2). This will allow us to comfortably distinguish among the different observational results and to put tight constraints on the theoretical models. What is needed in the future is a large campaign of observation, devoted to obtain the spectra of $\sim$400 Cepheids with metallicity that span a range of 1 dex. This means 15 nights of observation with a telescope such as the VLT and last generation instruments (namely FLAMES) to reach the necessary resolution and signal-to-noise to determine elemental abundances.

As we have discussed in section 1.4, the PL-Colour (PLC) relation is the physical relation that accurately defines the properties of individual Cepheids. A further step in the study of the effect of the iron content on the properties of these stars would be the investigation on the PLC relation. The removal of the extinction is essential to the calibration of the intrinsic PLC relation, i.e. to disentangle the extinction effect and the true colour deviations within the instability strip. Only then it is possible to look for a meaningful correlation of the luminosity residuals with the metallicity. Up today, however, there are still issues and debates concerning the different methods adopted to determine the extinction for individual stars (e.g. see Madore & Freedman 1991, Luck & Lambert 1992, Munari 2000).

Waiting for these further investigations, to safely measure the distances of galaxies, one can use the PLC relation in the infrared bands (J and K), so as to reduce the extinction problem to the level of other systematic and random errors and minimise the effect of the metallicity.

Conclusion

The goal of this thesis is to assess the effect of the metallicity on the Cepheid Period-Luminosity relation. Our approach is based on the direct determination of the elemental abundances of individual Cepheids.

In Chapter 2 we have discussed the observational aspect of this thesis. The stars of this study were selected to obtain an unprecedented sample of 36 Galactic, 22 LMC and 14 SMC Cepheids for which we have well-determined mean magnitudes in optical and infrared bands and accurate distances, taken from the literature. The selection criteria of the data set were described along with telescopes and instruments used to collect high-quality spectra. We have then illustrated the data reduction process to produce the 1-D spectra necessary for our analysis.

The methodology adopted to determine the elemental abundances was presented in Chapter 3. The careful assembling of a line list along with the measurement of the equivalent widths are crucial steps of the analysis and were discussed in details. Then we have explained how to determine the stellar parameters (effective temperature, gravity and microturbulent velocity) from the observed spectra. As last step we have described the most recent model atmospheres (calculated with new opacity distribution functions) used in the determination of the abundances, comparing the differences on the resulting abundances with a less recent grid of models (calculated with the old opacity distribution functions). We have interpolated the grid of model atmospheres to obtain the exact temperature calculated for each star and steps of 0.1 dex for the logarithm of the gravity. Finally we have outlined an alternative method to establish the elemental abundances: the spectrum synthesis technique.

The results of this thesis are presented in Chapter 4, Chapter 5 and Chapter 6.

Chapter 4 is focused on the iron abundances of our sample of Cepheids, determined with the WIDTH9 code using the measured equivalent widths and the model atmospheres adopted for each star. The random and systematic uncertainties on the abundances were analysed in details. We have then made a comparison of our abundances with results from previous studies on Cepheids and other stellar populations. The mean values and the range of abundances determined for the Galactic sample, the LMC sample and the SMC sample are, respectively: $[\mathrm{Fe/H}]_{\mathrm{Gal}}$=0.00 $\pm$0.10 dex with a range between -0.18 and $+0.25$; $[\mathrm{Fe/H}]_{\mathrm{LMC}} = -0.33 \pm 0.13$ dex, with a range between -0.62 and -0.10 dex and $[\mathrm{Fe/H}]_{\mathrm{SMC}} = -0.75 \pm 0.08$ dex, with a range from -0.87 to -0.63. The observed scatter in each galaxy corresponds to a real variation of the iron content among the sample of Cepheids we have studied. We have compared our iron abundances with studies on Galactic and Magellanic Cepheids and found a good agreement for the average values and for the individual

stars in common. We have then made a broader comparison with results for the Magellanic Clouds from the analysis of F and K non-variable supergiants (they have ages and temperatures similar to Cepheid stars) and of B stars, which are progenitors of Cepheids, and found a good agreement. Cepheids do not show any peculiar differences with these two other population of stars, this indicate that, during this evolutionary stage, there are no changes of the original iron content of the gas from which they were formed.

The α element abundances are presented in Chapter 5. We have determined the abundances of oxygen, sodium, magnesium, aluminium, silicon, calcium and titanium (neutral and ionised). The O abundances were obtained using the spectrum synthesis technique, which was discussed for the adopted O lines, while the other elements were studied using the same approach adopted for iron. The analysis of the random and systematic uncertainties was detailed. We have then studied the trends of the individual abundance ratios relative to iron as a function of the iron content of our programme star. We can draw some preliminary conclusion considering oxygen, silicon and calcium as the most reliable indicators among the α elements we have analysed, since more improvement and refinements of the analysis are needed for the other elements, in order to solve the problems that affect their abundances. The trends of the abundance ratios of O, Si and Ca are in fairly good agreement with observational studies on Cepheids and on different kinds of stellar populations in the Galaxy and the Magellanic Clouds. Furthermore they agree with the theoretical predictions for the trend of [α/Fe] by Matteucci (2003). We can also say that oxygen is a good tracer of the iron content, i.e. of the metallicity, thus it is reasonable to compare our results with observational studies that use [O/H] as indicator of the metallicity.

The final part (Chapter 6) of this thesis deals with the assessment of the effect of the metallicity on the Period-Luminosity relation. The elemental abundances we have determined were used to investigate this effect in the V and K bands, in order to check if there is a change of the effect as wavelength increases. To detect this influence we have divided our sample of Cepheids in two bins of metallicity that contain the same number of stars. The choice of the number of bins is crucial because more bins one adopts more details can be unraveled about this effect, but it is also essential to use a statistical significant number of stars to populate well the PL relation in each bin. We have chosen two bins as the best possible approach with this data set, after we have carried out several simulation. We have tested how well a randomly selected sub-sample of stars can approximate the PL relation obtained from a sample of Cepheids ($\sim$ 800 stars) that populate it well (distributed well in periods). We have determined the PL relation in each bin and, from the comparison with two standard PL relations (in the V and K bands), assessed the effect of the iron content on its slope and zero point and on the residuals of the magnitude. From the outcomes of the simulations we observe that the slope and the zero point are correlated, thus their trends with [Fe/H] are correlated too. The net effect of the iron content on the PL relation is given by the residuals δ.

In the V band the slope of the PL relation decreases with the iron content, while the zero point increases. The mean values of the V-band residuals in both bins are positive and there is an increasing trend with the iron content. We observe similar trends as function of the total metallicity, that we have estimated adding the iron, oxygen, silicon and calcium abundances, since the three latter elements are the most reliable indicators among the α elements we have analysed. This behaviour means that metal-rich Cepheids are fainter than metal-poor ones.

In the K band the residuals present a flat trend around zero, while slope and zero point show opposite behaviours: a steep decrease and a steep increase with [Fe/H], respectively. Again we observe similar behaviours of the residuals, the slope and the zero point as function of the estimated total metallicity.

We have compared our results with two different behaviours as examples of the effects of the metallicity on the PL relation currently reported in the literature: independence from the iron content and a monotonic decreasing trend, in the sense that metal-rich Cepheids are brighter than metal-poor ones (the complete comparison is possible only in the V-band). The result in the V band is in disagreement with both hypothesis, while the K-band result, instead, agrees with the hypothesis of no dependence of the PL relation on the iron content.

To conclude, we note different behaviours in the two bands. The metallicity has an effect on the Cepheid PL relation in the V band in the sense that metal-rich Cepheids are fainter than metal-poor ones, while it does not have any effects in the K band. Thus, to safely measure the distances of galaxies, one can use the PL relation in the infrared bands (namely K), so as to minimise the effect of the metallicity. Using the K band has the additional advantage of reducing the effects of the interstellar extiction to the level of other systematic and random errors.

Future work

In the immediate future, the first step to undertake is an improvement and a refinement of our analysis of the α elements to solve the problems for Ti, Mg, Na and Al. Moreover a detailed comparison with theoretical predictions for each element is needed to investigate the gas enrichment history that led to the formation of Cepheids.

To improve the study of the influence of the metallicity on the Cepheid Period-Luminosity relation a large campaign of observation is needed, devoted to obtain the spectra of $\sim$400 Cepheids with metallicity that span a range of 1 dex. It will be possible to have a high number of stars (100) in smaller bins of metallicity (one for each Magellanic Clouds and two for Galactic Cepheids) than the ones we have used in the current analysis, this will allow us to discern much finer details, such as a non-monotonic behaviour, to comfortably distinguish among the different observational results and to put tight constraints on the theoretical models. This means 15 nights of observation with a telescope such as the VLT and the latest generation of instruments (namely FLAMES) to reach the necessary resolution and signal-to-noise to determine elemental abundances.

A further step would be the investigation of the effect of the metallicity on the Period-Luminosity-Colour relation, since this is the physical relation that accurately defines the properties of individual Cepheids. It is crucial to disentangle the extinction effect and the true colour deviations within the instability strip. Only then it is possible to look for a meaningful correlation of the luminosity residuals with the metallicity.

Appendix A

Spectroscopy: basic principles

Following Thackeray ("Astronomical spectroscopy", 1961), Allington-Smith ("Dispersive astronomical spectroscopy", 2002) and Oliver ("Basic spectroscopy", 2004), we summarise here the main principles and characteristics of astronomical spectrographs.

The basic astronomical spectrograph is comprised of a slit, a collimator, a dispersing element (typically a diffraction grating or a prism), a camera and a detector (see Fig A.1):

- Slit: isolates a portion of sky that is imaged in a single beam
- Collimator: makes the beam parallel
- Dispersing element: disperses light as a function of wavelength
- Camera: forms image of object (star or slit) on detector
- Detector: records the image, usually in a digital format

In Figure A.1 are also indicated the focal lengths of the telescope, the collimator and the camera (F, *fcol* and *fcam*, respectively). The corresponding focal ratios are, respectively:
$\phi_{TEL} = F/D$, $\phi_{col} = f_{col}/a$ and $\phi_{cam} = f_{cam}/a$
where D is the diameter of the telescope and a is the camera aperture.

The most important design characteristics of a spectrograph are the *dispersion*, which defines how widely the various wavelengths are spread out, and the *resolution*, which describes the minimum difference in wavelength that can be determined.

A.1 Dispersion

The dispersion (also called angular dispersion) is the change of the diffraction angle corresponding to a change of wavelength: $d\Theta/d\lambda$. If we consider the linear displacement x on the detector plane we can define the linear dispersion as $dx/d\lambda = d\Theta/d\lambda \cdot f_{cam}$ using the relation between a

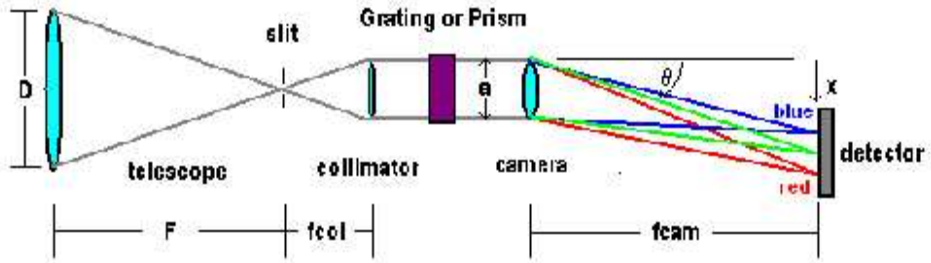

Figure A.1: *Basic astronomical spectrograph scheme. Where* D *is the diameter of the telescope,* F, fcol *and* fcam *are, respectively, the focal lengths of the telescope, the collimator and the camera,* a *is the camera aperture,* Θ *is the output angle of the diffracted beam and* x *is the linear displacement in the direction of the dispersion on the plane of the detector (figure from Oliver 2004).*

small angular change and a small linear change: $dx = d\Theta \cdot f_{cam}$, where f_{cam} is the camera focal length. While $dx/d\lambda$ is properly defined as linear dispersion, astronomers frequently work with the *linear reciprocal dispersion*, usually quoted in Å/mm. It is not uncommon to hear linear reciprocal dispersion referred to as "dispersion". (Linear reciprocal) dispersions between 50 and 200 Å /mm are typically considered "low" dispersion (mainly useful for spectral classification), between 10 and 50Å/mm are "medium" dispersion (typically used for radial velocities) and less than 10 Å/mm are "high" dispersion (needed for line profile analysis, abundance analysis).

A.1.1 Dispersing element

Spectrographs disperse light using different kind of dispersing elements, such as prisms, transmission and reflection gratings or grisms. The most common grating in astronomical spectroscopy is the reflection grating and we will use it as an example to establish the basic principles. A reflection grating has a series of closely spaced grooves so that light reflects off the grating surface as though there was a series of narrow parallel mirrors (see Fig A.2). Constructive interference between the reflected beams of light at specific angles for a given wavelength and not for other wavelengths results in the creation of a spectrum. The constructive interference condition is fulfilled when the path difference between adjacent rays is equal to multiples, m, of the wavelength of the illuminating light. This leads to the grating equation:

$$\frac{m \cdot \lambda}{d} = \sin\Theta + \sin i \tag{A.1}$$

where m is called the spectral order, d is the spacing between the repeated element in the grating and Θ and i are the angles of diffraction and incidence, respectively, as measured from the normal to the grating surface.

By differentiating with respect to the output angle we obtain the dispersion equation:

$$\frac{d\Theta}{d\lambda} = \frac{m}{d \cdot \cos\Theta} \tag{A.2}$$

The beam is dispersed into multiple rays of light. The 0^{th} order is not dispersed (white light) because all the wavelengths are deflected by the same angle. Given an order $m \geq 1$, red light is dispersed at a greater angle than blue light (see Fig A.3), thus producing a spectrum.

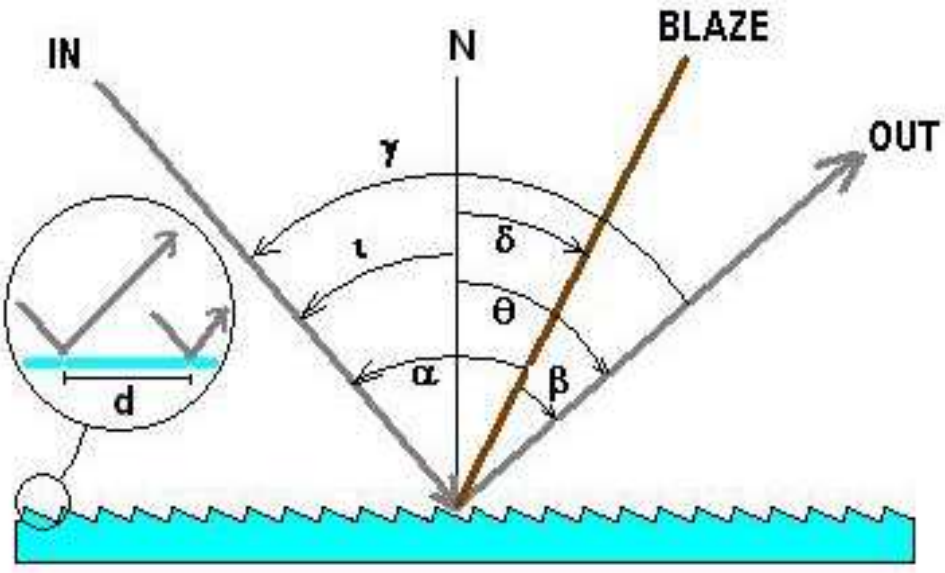

Figure A.2: *A reflection diffraction grating:* N *is the normal to the plane of the grating,* BLAZE *is the normal to the facets of the grating,* d *is the spacing between the repeated element in the grating,* δ *is the tilting angle of the facets to the grating plane,* Θ *and* i *are the angles of diffraction and incidence as measured from* N *while* β *and* α *are the same angles but measured from* BLAZE, γ *is the collimator-camera angle (figure from Oliver 2004).*

Also, the dispersion increases at higher orders, which is why high resolution spectrographs work at high m (UVES as a typical order value of 100). The blue end of order m+1 will overlap the red end of order m. Therefore it may be necessary to insert a colored glass filter to isolate the order of interest (order-separating filter) or a further dispersing element who separates them in the direction perpendicular to the dispersion (cross disperser). The useful spectral range (over which orders will not overlap) is approximately:

$$\lambda_{red} - \lambda_{blue} \cong \frac{\lambda_{central}}{m}$$

the higher m, the narrower the spectral range $\lambda_{red} - \lambda_{blue}$.

Blazed Gratings

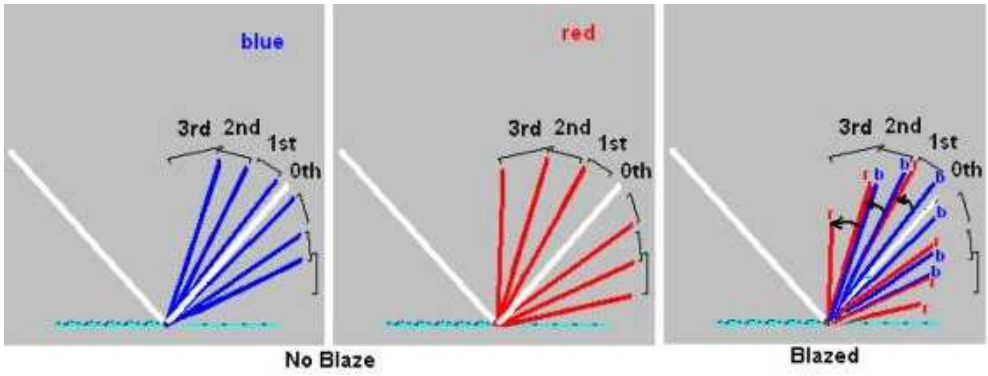

Figure A.3: *Dispersion increases with the order and the light wavelength as it can be see for blue and red light in the left and centre panel. The maximum intensity of the light corresponds to the 0^{th} order (no blaze). In the case of a blazed grating a large percentage of the incident light is casted into a prescribed order (1^{st}) as shown in the right panel (figure from Oliver 2004).*

The light ray with the maximum intensity is the one that follows the reflection law (incidence angle is equal to the refraction angle) and, in not-blazed gratings, it is in coincidence with the 0^{th} order spectrum, in which there is no dispersion. Blazing is a technique of angling the surface of the grooves in a grating so that it shifts the position of the maximum intensity from the 0^{th} order spectrum to a higher order spectrum, thus rendering the higher order brighter. The blaze condition is fulfilled when the reflection law is satisfied with respect to the normal to the facets of the grating, i.e. when $\alpha = \beta$ (see Fig. A.2). An example can be see in Fig A.3, right panel, where the maximum intensity corresponds to the 1^{st} order. The grating equation at the blaze condition is

$$\frac{m \cdot \lambda_B}{d} = 2 \sin\delta \cos\gamma/2$$

since $2\delta = i + \Theta$ and $\gamma = i - \Theta$, where λ_B is the wavelength for which the blaze condition is satisfied, γ is the collimator-camera angle which is fixed by the design of the spectrograph and δ is the tilting angle of the facets to the grating plane.

Grism

A grism is a combination of a diffraction grating and a prism. Here a grating has been glued to the surface of a prism. The equivalent of the grating equation (Eq. A.1) becomes

$$\frac{m \cdot \lambda}{d} = n \cdot \sin\Theta + \sin i$$

where n is the refraction index of the prism glass and the grating material, which are assumed to be equal. Considering the typical case shown in Fig A.4 where the input prism face and the facets are both normal to the optical axis, the most useful configuration is when the light is undeviated ($\Theta = -i$), allowing the camera and the collimator to be in line. The advantage of this configuration

is that the monochromatic image of the target will appear at the same location as a direct image obtained with the grism removed.

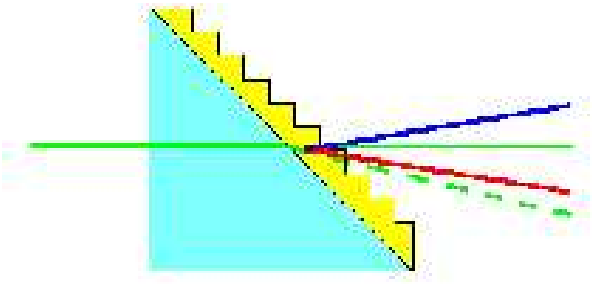

Figure A.4: *Grism scheme (figure from Oliver 2004).*

Echelle

To increase the resolution of a grating one can either decrease the spacing between groove d, or increase the order m. Combining Eq. A.1 and Eq. A.2, the dispersion equation can be rewritten as:

$$\frac{d\Theta}{d\lambda} = \frac{\sin\Theta + \sin i}{\lambda \cdot \cos\Theta}$$

from which it can be seen that high dispersion can also be achieved by operating at values of i and Θ close to 90°. This is the principle of an echelle grating, which has large d, and operates at high m (typically more than 50), i and Θ, and gives high dispersion. To prevent the overlapping of the orders a prism or a grating is mounted with its dispersion perpendicular to the echelle dispersion (cross-dispersion) so that it separates the various orders.

A.2 Resolution

The collimator/camera optical system images the focal plane of the telescope on to the detector plane of the spectrograph. In order to limit the spreading of light of a single wavelength in the dispersion direction, a slit is usually employed on the telescope focal plane to mask the light from the astronomical object. In the case of a single dominant point source in the image plane or if point sources are spaced far enough that spectra will not overlap, spectroscopy can be done without a slit. However, in the slitless case, the resulting spectrum can be significantly impacted by sky emission.

For a given value of the dispersion, the resolution $\delta\lambda$ depends on the width of the slit or on the size of the image parallel to the dispersion direction, whichever is smaller. This is easy to understand by considering that a spectrograph creates an image of the focal plane after dispersing the light. The "width" of a spectral line, then, will be given by the width of the slit or the image.

Formally, the resolution is determined by the width of the image, w, projected on the detector, w' : $\delta\lambda = w' \cdot d\lambda/dx$. To determine w', we use the conservation of etendue in its one-dimensional

case[a]:

$$w\Phi = w'\Phi'$$

where $\Phi = a/f_{col}$ and $\Phi' = a/f_{cam}$ are the beam angles at the slit and the detector. Then w' is given by:

$$w' = w\frac{\phi_{cam}}{\phi_{col}} = w\frac{f_{cam}}{f_{col}}$$

Using this relation we can derive the resolution of the system:

$$\delta\lambda = w\frac{\phi_{cam}}{\phi_{col}} \cdot \frac{d\lambda}{dx}$$

where $d\lambda/dx$ is the linear reciprocal dispersion discussed above. The bigger w, the lower the resolution. It is also quite common a dimensionless expression, called resolving power, defined as:

$$R = \frac{\lambda}{\delta\lambda} = \frac{\lambda\phi_{col}}{w\phi_{cam}(d\lambda/dx)}$$

[a]the etendue, or light gathering power, is defined as the product of the solid angle Ω of a radiation incident at a surface of area A in a medium with refractive index n. For optics in air or vacuum $n = 1$

Appendix B

Line lists

Our final lists includes 246 FeI lines, 17 FeII lines, 5 OI lines, 4 NaI lines, 6 MgI lines, 4 AlI lines, 49 SiI lines, 28 CaI lines, 53 TiI lines and 18 TiII lines, spanning a spectral range from 4800 Å to 7900 Å which is the range covered by our FEROS spectra. Our UVES spectra cover a narrower spectral range for which we can use 181 FeI lines, 13 FeII lines, 2 OI lines, 2 NaI lines, 5 MgI lines, 2 AlI lines, 27 SiI lines, 22 CaI lines, 42 TiI lines and 12 TiII lines. For all the lines, we have adopted the physical properties (oscillator strengths, excitation potentials) listed in VALD.

The line lists for the [OI] 6300 Å and 6363 Å regions are listed at the end of the appendix.

Table B.1: *FeI and FeII line list.*

wavelength [Å]	ion	EP [eV]	log(gf)
4896.438	FeI	3.88	-2.05
4917.230	FeI	4.19	-1.18
4924.770	FeI	2.28	-2.24
5049.820	FeI	2.28	-1.36
5056.841	FeI	4.26	-1.96
5083.338	FeI	0.96	-2.96
5088.153	FeI	4.15	-1.78
5090.774	FeI	4.26	-0.40
5217.389	FeI	3.21	-1.07
5242.491	FeI	3.63	-0.97
5326.143	FeI	3.57	-2.07
5339.929	FeI	3.27	-0.65
5364.871	FeI	4.45	0.23
5365.399	FeI	3.57	-1.02
5367.467	FeI	4.41	0.44
5373.708	FeI	4.47	-0.86

contined on the next page

continued from previous page			
wavelength [Å]	ion	EP [eV]	log(gf)
5383.369	FeI	4.31	0.64
5386.334	FeI	4.15	-1.77
5389.479	FeI	4.41	-0.41
5398.279	FeI	4.45	-0.67
5401.269	FeI	4.32	-1.92
5412.786	FeI	4.43	-1.72
5445.042	FeI	4.39	-0.02
5522.446	FeI	4.21	-1.55
5560.211	FeI	4.43	-1.19
5562.706	FeI	4.44	-0.66
5576.089	FeI	3.43	-1.00
5586.756	FeI	3.37	-0.12
5633.946	FeI	4.99	-0.27
5636.696	FeI	3.64	-2.61
5638.262	FeI	4.22	-0.87
5641.434	FeI	4.26	-1.18
5649.987	FeI	5.10	-0.92
5650.706	FeI	5.09	-0.96
5651.469	FeI	4.47	-2.00
5652.318	FeI	4.26	-1.95
5653.867	FeI	4.39	-1.64
5661.346	FeI	4.28	-1.74
5672.264	FeI	4.58	-2.80
5678.379	FeI	3.88	-3.02
5679.023	FeI	4.65	-0.92
5680.240	FeI	4.19	-2.58
5691.497	FeI	4.30	-1.52
5701.544	FeI	2.56	-2.22
5705.465	FeI	4.30	-1.36
5720.898	FeI	4.55	-1.95
5724.455	FeI	4.28	-2.64
5741.849	FeI	4.26	-1.85
5752.023	FeI	4.55	-1.27
5759.262	FeI	4.65	-2.07
5760.345	FeI	3.64	-2.49
5762.414	FeI	3.64	-2.28
5775.081	FeI	4.22	-1.30
5778.453	FeI	2.59	-3.43
		contined on the next page	

continued from previous page			
wavelength [Å]	ion	EP [eV]	log(gf)
5793.915	FeI	4.22	-1.70
5806.725	FeI	4.61	-1.05
5811.915	FeI	4.14	-2.43
5814.808	FeI	4.28	-1.97
5826.638	FeI	4.28	-2.94
5827.877	FeI	3.28	-3.41
5835.101	FeI	4.26	-2.37
5837.701	FeI	4.29	-2.34
5845.287	FeI	5.03	-1.82
5849.684	FeI	3.69	-2.99
5855.077	FeI	4.61	-1.48
5856.088	FeI	4.29	-1.33
5859.578	FeI	4.55	-0.40
5861.109	FeI	4.28	-2.45
5862.353	FeI	4.55	-0.06
5864.245	FeI	4.30	-2.52
5873.213	FeI	4.26	-2.14
5877.788	FeI	4.18	-2.23
5879.487	FeI	4.61	-2.14
5880.027	FeI	4.56	-1.94
5881.280	FeI	4.61	-1.84
5883.817	FeI	3.96	-1.36
5902.474	FeI	4.59	-1.81
5905.672	FeI	4.65	-0.73
5927.789	FeI	4.65	-1.09
5930.180	FeI	4.65	-0.23
5934.655	FeI	3.93	-1.17
5956.694	FeI	0.86	-4.61
5976.775	FeI	3.94	-1.31
5984.814	FeI	4.73	-0.34
5987.066	FeI	4.80	-0.56
6003.012	FeI	3.88	-1.12
6008.554	FeI	3.88	-1.08
6015.244	FeI	2.22	-4.68
6018.298	FeI	4.65	-2.66
6020.169	FeI	4.61	-0.27
6024.058	FeI	4.55	-0.12
6027.051	FeI	4.08	-1.09
			contined on the next page

continued from previous page

wavelength [Å]	ion	EP [eV]	log(gf)
6054.074	FeI	4.37	-2.31
6056.005	FeI	4.73	-0.46
6065.482	FeI	2.61	-1.53
6078.491	FeI	4.80	-0.42
6079.009	FeI	4.65	-1.12
6082.710	FeI	2.22	-3.57
6093.645	FeI	4.61	-1.50
6094.374	FeI	4.65	-1.94
6096.666	FeI	3.98	-1.93
6098.245	FeI	4.56	-1.88
6102.173	FeI	4.84	-0.63
6105.131	FeI	4.55	-2.05
6120.250	FeI	0.92	-5.95
6127.907	FeI	4.14	-1.40
6151.618	FeI	2.18	-3.30
6165.360	FeI	4.14	-1.47
6173.335	FeI	2.22	-2.88
6180.204	FeI	2.73	-2.59
6187.990	FeI	3.94	-1.72
6200.313	FeI	2.61	-2.44
6209.713	FeI	3.96	-3.23
6213.430	FeI	2.22	-2.48
6215.144	FeI	4.19	-1.32
6220.784	FeI	3.88	-2.46
6226.736	FeI	3.88	-2.22
6229.229	FeI	2.85	-2.81
6232.641	FeI	3.65	-1.22
6240.646	FeI	2.22	-3.23
6246.319	FeI	3.60	-0.73
6252.555	FeI	2.40	-1.69
6265.134	FeI	2.18	-2.55
6270.225	FeI	2.86	-2.46
6271.279	FeI	3.33	-2.70
6290.969	FeI	4.73	-0.97
6297.793	FeI	2.22	-2.74
6301.501	FeI	3.65	-0.72
6311.500	FeI	2.83	-3.14
6315.812	FeI	4.08	-1.71

contined on the next page

continued from previous page			
wavelength [Å]	ion	EP [eV]	log(gf)
6322.686	FeI	2.59	-2.43
6330.850	FeI	4.73	-1.74
6335.331	FeI	2.20	-2.18
6336.824	FeI	3.69	-0.86
6344.149	FeI	2.43	-2.92
6355.029	FeI	2.85	-2.35
6364.366	FeI	4.80	-1.43
6380.743	FeI	4.19	-1.38
6392.539	FeI	2.28	-4.03
6393.601	FeI	2.43	-1.43
6400.001	FeI	3.60	-0.29
6411.649	FeI	3.65	-0.60
6419.950	FeI	4.73	-0.24
6436.407	FeI	4.19	-2.46
6475.625	FeI	2.56	-2.94
6481.870	FeI	2.28	-2.98
6495.742	FeI	4.84	-0.94
6498.939	FeI	0.96	-4.70
6509.617	FeI	4.08	-2.97
6533.929	FeI	4.56	-1.46
6569.215	FeI	4.73	-0.42
6592.914	FeI	2.73	-1.47
6593.871	FeI	2.43	-2.42
6597.561	FeI	4.80	-1.07
6608.026	FeI	2.28	-4.03
6609.110	FeI	2.56	-2.69
6627.545	FeI	4.55	-1.68
6646.932	FeI	2.61	-3.99
6653.853	FeI	4.15	-2.52
6699.142	FeI	4.59	-2.10
6703.567	FeI	2.76	-3.16
6704.481	FeI	4.22	-2.66
6710.319	FeI	1.49	-4.88
6713.745	FeI	4.80	-1.60
6715.383	FeI	4.61	-1.64
6716.237	FeI	4.58	-1.92
6725.357	FeI	4.10	-2.30
6726.661	FeI	4.61	-0.83
		contined on the next page	

continued from previous page			
wavelength [Å]	ion	EP [eV]	log(gf)
6733.151	FeI	4.64	-1.58
6739.522	FeI	1.56	-4.79
6745.101	FeI	4.58	-2.16
6745.957	FeI	4.08	-2.77
6746.955	FeI	2.61	-4.35
6750.152	FeI	2.42	-2.62
6752.707	FeI	4.64	-1.20
6761.070	FeI	4.58	-2.53
6764.118	FeI	4.59	-2.59
6769.659	FeI	4.58	-2.66
6786.860	FeI	4.19	-2.07
6793.259	FeI	4.08	-2.33
6794.619	FeI	4.95	-2.11
6801.864	FeI	1.61	-5.04
6806.845	FeI	2.73	-3.21
6810.263	FeI	4.61	-0.99
6820.372	FeI	4.64	-1.32
6824.823	FeI	4.99	-2.13
6828.591	FeI	4.64	-0.92
6833.226	FeI	4.64	-2.08
6837.006	FeI	4.59	-1.69
6839.831	FeI	2.56	-3.45
6841.339	FeI	4.61	-0.75
6842.686	FeI	4.64	-1.32
6843.656	FeI	4.55	-0.93
6851.635	FeI	1.61	-5.32
6857.250	FeI	4.08	-2.15
6858.150	FeI	4.61	-0.93
6862.480	FeI	4.56	-1.57
6864.313	FeI	4.56	-2.32
6945.205	FeI	2.42	-2.48
6951.257	FeI	4.56	-1.46
6970.473	FeI	3.02	-3.23
6971.950	FeI	3.02	-3.34
6988.523	FeI	2.40	-3.66
6999.884	FeI	4.10	-1.56
7000.618	FeI	4.14	-2.39
7014.985	FeI	2.45	-4.25
		contined on the next page	

continued from previous page			
wavelength [Å]	ion	EP [eV]	log(gf)
7022.954	FeI	4.19	-1.25
7057.950	FeI	3.65	-3.38
7071.880	FeI	4.61	-1.70
7112.180	FeI	2.99	-3.00
7118.100	FeI	5.01	-1.57
7127.564	FeI	4.99	-1.36
7132.986	FeI	4.08	-1.63
7142.503	FeI	4.96	-0.93
7158.474	FeI	3.65	-2.89
7181.192	FeI	4.22	-0.88
7212.432	FeI	4.96	-0.99
7221.200	FeI	4.56	-1.80
7445.746	FeI	4.26	-0.24
7447.384	FeI	4.96	-1.29
7453.998	FeI	4.19	-2.41
7461.521	FeI	2.56	-3.58
7463.382	FeI	5.06	-1.72
7473.554	FeI	4.61	-1.87
7491.649	FeI	4.30	-1.01
7498.530	FeI	4.14	-2.25
7507.261	FeI	4.41	-3.48
7531.141	FeI	4.37	-1.31
7540.430	FeI	2.73	-3.85
7547.910	FeI	5.10	-1.64
7551.109	FeI	5.09	-1.63
7563.012	FeI	4.84	-1.88
7568.894	FeI	4.28	-0.88
7583.788	FeI	3.02	-1.88
7586.014	FeI	4.31	-0.87
7588.305	FeI	5.03	-2.06
7719.038	FeI	5.03	-1.37
7723.208	FeI	2.28	-3.62
7745.500	FeI	5.09	-1.29
7746.587	FeI	5.06	-1.51
7748.270	FeI	2.95	-1.75
7751.137	FeI	4.99	-0.89
7780.552	FeI	4.47	-2.36
7802.473	FeI	5.09	-1.58
		contined on the next page	

continued from previous page			
wavelength [Å]	ion	EP [eV]	log(gf)
7807.952	FeI	4.99	-0.70
7832.194	FeI	4.43	0.02
4893.820	FeII	2.83	-4.45
4923.927	FeII	2.89	-1.32
5414.073	FeII	3.22	-3.54
5824.415	FeII	3.42	-6.04
5932.055	FeII	3.20	-4.81
6149.258	FeII	3.89	-2.72
6179.384	FeII	5.57	-2.81
6247.557	FeII	3.89	-2.31
6331.954	FeII	6.22	-1.98
6383.722	FeII	5.55	-2.07
6432.680	FeII	2.89	-3.52
6446.410	FeII	6.22	-1.96
6516.080	FeII	2.89	-3.32
7222.394	FeII	3.89	-3.36
7449.335	FeII	3.89	-3.09
7479.693	FeII	3.89	-3.68
7711.723	FeII	3.90	-2.50

Table B.2: *AlI, CaI, MgI, NaI, OI, SiI, TiI and TiII line list.*

wavelength [Å]	ion	EP [eV]	log(gf)
6696.02	AlI	3.14	-1.35
6698.67	AlI	3.14	-1.64
7835.31	AlI	4.02	-0.65
7836.13	AlI	4.02	-0.49
4283.01	CaI	1.89	-0.29
4425.44	CaI	1.88	-0.29
4434.96	CaI	1.89	0.07
4878.13	CaI	2.71	0.43
5041.62	CaI	2.71	-0.66
5270.27	CaI	2.53	0.12
5512.98	CaI	2.93	-0.71
5581.97	CaI	2.52	-0.57
5588.75	CaI	2.53	0.31
5590.11	CaI	2.52	-0.60
5601.28	CaI	2.53	-0.55
5867.56	CaI	2.93	-1.58
6122.22	CaI	1.89	-0.39
6162.17	CaI	1.90	-0.17
6166.44	CaI	2.52	-1.16
6169.04	CaI	2.52	-0.80
6169.56	CaI	2.53	-0.53
6318.11	CaI	4.43	0.06
6439.08	CaI	2.52	0.03
6449.81	CaI	2.52	-1.02
6455.60	CaI	2.52	-1.56
6464.67	CaI	2.52	-4.27
6471.66	CaI	2.53	-0.65
6493.78	CaI	2.52	0.02
6499.65	CaI	2.52	-0.85
6717.68	CaI	2.71	-0.60
7148.15	CaI	2.71	-0.13
7202.20	CaI	2.71	-0.81
5172.68	MgI	2.71	-0.40
5528.41	MgI	4.35	-0.62
5711.09	MgI	4.35	-1.83
6318.72	MgI	5.11	-1.73
		contined on the next page	

continued from previous page			
wavelength [Å]	ion	EP [eV]	log(gf)
6319.24	MgI	5.11	-2.28
7759.30	MgI	5.93	-1.65
5889.95	NaI	0.00	0.12
5895.92	NaI	0.00	-0.18
6154.23	NaI	2.10	-1.56
6160.75	NaI	2.10	-1.26
6300.30	OI	0.00	-9.83
6363.77	OI	0.02	-10.30
7771.94	OI	9.15	0.37
7774.16	OI	9.15	0.22
7775.39	OI	9.15	0.00
4505.93	SiI	4.95	-2.15
4627.38	SiI	5.08	-1.52
4747.99	SiI	4.93	-1.75
4947.61	SiI	5.08	-1.82
5258.84	SiI	5.62	-0.18
5338.21	SiI	5.62	-0.63
5645.62	SiI	4.93	-2.03
5666.68	SiI	5.62	-1.05
5690.43	SiI	4.93	-1.87
5701.10	SiI	4.93	-2.05
5772.15	SiI	5.08	-1.75
5948.54	SiI	5.08	-1.23
6029.87	SiI	5.98	-0.42
6091.92	SiI	5.87	-1.39
6125.03	SiI	5.61	-1.46
6131.57	SiI	5.62	-1.20
6131.85	SiI	5.62	-1.14
6142.48	SiI	5.62	-0.92
6145.02	SiI	5.62	-0.82
6155.14	SiI	5.62	-0.88
6237.32	SiI	5.61	-0.53
6243.82	SiI	5.62	-0.77
6244.48	SiI	5.61	-1.24
6254.19	SiI	5.62	-0.60
6308.83	SiI	5.86	-2.00
6414.98	SiI	5.87	-1.10
6555.46	SiI	5.98	0.00
			contined on the next page

continued from previous page			
wavelength [Å]	ion	EP [eV]	log(gf)
6583.71	SiI	5.95	-1.57
6721.85	SiI	5.86	-1.02
6741.63	SiI	5.98	-1.55
6800.60	SiI	5.96	-1.75
6848.57	SiI	5.86	-1.65
7003.57	SiI	5.96	-0.97
7005.88	SiI	5.98	-0.98
7017.65	SiI	5.87	0.00
7034.91	SiI	5.87	-0.84
7165.55	SiI	5.87	-0.60
7226.21	SiI	5.61	-1.46
7275.29	SiI	5.62	0.00
7289.18	SiI	5.62	-0.20
7405.77	SiI	5.61	-0.82
7415.95	SiI	5.62	-0.50
7423.50	SiI	5.62	-0.31
7680.27	SiI	5.86	-0.69
7688.40	SiI	6.19	-1.47
7760.64	SiI	6.20	-1.35
7800.00	SiI	6.18	-0.69
7918.38	SiI	5.95	-0.61
7944.00	SiI	5.98	-0.31
4278.22	TiI	2.58	0.26
4393.92	TiI	2.27	0.02
4534.78	TiI	0.84	0.28
4548.76	TiI	0.83	-0.35
4617.27	TiI	1.75	0.39
4623.10	TiI	1.74	0.11
4759.27	TiI	2.26	0.51
4840.87	TiI	0.90	-0.51
4870.13	TiI	2.25	0.52
4928.34	TiI	2.15	0.05
4991.07	TiI	0.84	0.38
4999.50	TiI	0.83	0.25
5016.16	TiI	0.85	-0.57
5024.84	TiI	0.82	-0.60
5039.96	TiI	0.02	-1.13
5065.99	TiI	1.44	-0.89
			contined on the next page

continued from previous page			
wavelength [Å]	ion	EP [eV]	log(gf)
5120.42	TiI	2.58	0.55
5145.46	TiI	1.46	-0.57
5210.39	TiI	0.05	-0.88
5219.70	TiI	0.02	-2.29
5282.38	TiI	1.05	-1.30
5490.15	TiI	1.46	-0.93
5644.13	TiI	2.27	0.21
5648.57	TiI	2.49	-0.37
5673.41	TiI	3.11	-0.62
5679.91	TiI	2.47	-0.74
5689.47	TiI	2.30	-0.57
5713.88	TiI	2.29	-1.00
5716.45	TiI	2.30	-0.83
5739.46	TiI	2.25	-0.81
5766.33	TiI	3.29	0.30
5866.45	TiI	1.07	-0.84
5922.11	TiI	1.05	-1.46
5937.81	TiI	1.07	-1.95
5953.16	TiI	1.89	-0.33
5965.83	TiI	1.88	-0.41
5978.54	TiI	1.87	-0.50
5999.66	TiI	2.24	-0.79
6064.63	TiI	1.05	-1.85
6091.18	TiI	2.27	-0.42
6092.81	TiI	1.89	-1.36
6098.66	TiI	3.06	-0.11
6258.10	TiI	1.44	-0.36
6258.71	TiI	1.46	-0.24
6261.10	TiI	1.43	-0.48
6312.24	TiI	1.46	-1.52
6508.15	TiI	1.43	-1.99
6599.11	TiI	0.90	-2.06
6745.55	TiI	2.24	-1.10
6996.66	TiI	2.33	-1.03
7209.44	TiI	1.46	-0.50
7251.71	TiI	1.43	-0.77
7466.52	TiI	1.74	-1.49
4316.80	TiII	2.05	-1.58
		contined on the next page	

continued from previous page			
wavelength [Å]	ion	EP [eV]	log(gf)
4418.33	TiII	1.24	-1.99
4568.31	TiII	1.22	-3.03
4589.96	TiII	1.24	-1.62
4609.26	TiII	1.18	-3.43
4911.19	TiII	3.12	-0.65
4996.37	TiII	1.58	-3.29
5013.68	TiII	1.58	-1.99
5185.91	TiII	1.89	-1.37
5188.68	TiII	1.58	-1.05
5211.54	TiII	2.59	-1.36
5418.75	TiII	1.58	-2.11
5490.69	TiII	1.57	-2.65
5492.86	TiII	1.58	-3.31
6214.60	TiII	2.05	-2.03
6219.94	TiII	2.06	-2.82
6680.13	TiII	3.10	-1.86
6998.91	TiII	3.12	-1.45

Table B.3: *Line list for the [OI] 6300 Å region.*

λ	Ion	EP	gf-value
6299.610	CrI	3.84	1.00E-3
6299.660	ZrI	1.520	1.585E-1
6299.691	CN	0.23	4.34E-3
6300.265	CN	1.28	5.78E-3
6300.310	OI	0.00	1.78E-10
6300.336	NiI	4.266	1.000E-3
6300.482	CN	1.31	6.82E-3
6300.482	CN	1.24	2.01E-3
6300.698	ScI	1.507	1.200E-2

Table B.4: *Line list for the [OI] 6363 Å region.*

λ	Ion	EP	gf-value
6362.338	ZnI	5.796	0.150
6362.864	CrI	0.941	-3.623
6362.876	FeI	4.186	-1.970
6363.776	OI	0.020	-10.303
6364.366	FeI	4.795	-1.430
6364.566	NiI	1.951	-3.970
6364.701	FeI	4.584	-1.469

Bibliography

Allende Prieto, C., Lambert, D.L., Asplund, M. 2001, ApJ, 556, 63

Alloin, D. 1998, Astrophysical and Laboratory Spectroscopy. Proceedings of the Thirty-Third Scottish Universities' Summer School in Physics, held in St. Andrews, Scotland, September 1988. Editors, R. Brown, J. Lang; Publisher, The Scottish Universities' Summer School in Physics, Edinburgh, Scotland, 1988

Anders, E. & Grevesse, N.1989GeCoA..53..197

Andrievsky, S.M., Kovtyukh, V.V., Korotin, S.A. et al. 2001, A&A 367, 605

Andrievsky, S.M., Kovtyukh, V.V., Luck, R.E. et al. 2002a, A&A 381, 32

Andrievsky, S.M., Bersier, D., Kovtyukh, V.V. et al. 2002b, A&A 384, 140

Andrievsky, S.M., Kovtyukh, V.V., Luck, R.E. et al. 2002c, A&A 392, 491

Andrievsky, S.M., Luck, R.E., Martin, P. & Lepine, J.R.D. 2004, A&A 413, 159

Asplund, M., Grevesse, N., Sauval, A. J. 2004, A&A 417, 751

Baraffe, I. & Alibert, Y. 2001, A&A 371, 592

Becker, S.A., Iben, I., Jr., Tuggle, R.S. 1977, ApJ 218, 633

Becker, S.A.. 1981, ApJ 248, 298

Becker, S.A.. 1985, IAU COLL.82, TORONTO 84JUN P.104

Benedict, G.F., McArthur, B.E., Fredrick, L.W. et al. 2002, AJ 123, 473

Berdnikov, L.N., Turner D.G. 2001, ApJS 137, 209

Bohm-Vitense, E. 1994, AJ 107, 673

Bono, G., Caputo, F., Castellani, V., & Marconi, M. 1999, ApJ 512, 711

Bono, G., Caputo, F., Marconi, M. 2001, MNRAS 325, 1353

Bibliography

Bono, G., Groenewegen, M. A. T., Marconi, M. et al. 2002, ApJ 574, 33

Borissova, J., Minniti, D., Rejkuba, M. et al. 2004, A&A 423, 97

Caldwell, J.A.R. & Laney, C.D. 1991, in The Magellanic Clouds, 148th IAU Symposium, Kluwer Academic Publisher, Dordrecht, p.249

Caputo, F., Marconi, M., Musella, I. & Santolamazza, P. 2000, A&A 359, 1059

Carretta, E., Gratton, R.G., Clementini, G., Fusi Pecci, F. 2000, ApJ 533, 215

Carpenter, J.M. 2001, AJ 121, 2851

Carter, B. S. 1990, MNRAS, 242, 1

Carter, B. S. & Meadows, V. S. 1995, MNRAS 276, 734

Castelli, F., Gratton, R.G. & Kurucz, R.L. 1997, A&A 318, 841

Castelli, F. & Kurucz, R.L. 2003,in Modelling of Stellar Atmospheres, 210th IAU Symposium, Edited by N. Piskunov, W.W. Weiss and D.F. Gray. Published on behalf of the IAU by the Astronomical Society of the Pacific, p.A20

Cayrel, R 1988, in The Impact of Very High S/N Spectroscopy on Stellar Physics, 132th IAU Symposium, Kluwer Academic Publishers, Dordrecht., p.345

Charbonneau, P. 1995, ApJSS 101, 309

Chiosi, C., Wood, P.R., Bertelli, G. & Bressan, A. 1992, ApJ 387, 320

Chiosi, C., Wood, P.R., Capitanio, N. 1993 ApJS 86, 541

Ciardullo, R., Feldmeier, J.J., Jacoby, G.H., et al. 2002, ApJ 577, 31

Cioni, M.-R.L., van der Marel, R.P., Loup, C. & Habing, H.J. 2000, A&A 359, 601

Cioni, M.-R. L., Marquette, J.-B., Loup, C. 2001, A&A 377, 945

Clementini, G., Carretta, E., Gratton, R. et al., 1995, AJ 110, 2319

Christy, R.F. 1966, ApJ 144, 108

Cox, J. P., 1980, SSRv 27, 389

Dean, J. F., Warren, P. R., Cousins, A. W. J. 1978, MNRAS 183, 569

Dekker, H., D'Odorico, S., Kaufer, A et al. 2000, SPIE 4008, 534

Emerson, D., 1996, 'Interpreting Astronomical Spectra', pp. 472., Wiley-VCH

Bibliography

Eddington, A.S. 1927, MNRAS 87, 539

Eddington, A.S. 1941, MNRAS 101, 182

Eddington, A.S. 1942, MNRAS 102, 154

Edvardsson, B., Andersen, J., Gustafsson, B., 1993 A&A 275, 101

Evans, N.R. 1991, ApJ 372, 597

Fagotto, F., Bressan, A., Bertelli, G., Chiosi, C. 1994, A&AS 104, 365

Feast, M.W. & Catchpole, R.M. 1997, MNRAS 286, L1

Feast, M.W., Whitelock, P. 1997, MNRAS 291, 683

Feast, M.W. 1999, IAUS 192, 51

Feast, M.W. 2003, LNP 635, 45

Fernie, J.D., Evans, N.R., Beattie, B. & Seager S. 1995, IBVS 4148, 1

Fiorentino, G., Caputo, F., Marconi, M. & Musella, I. 2002, ApJ 576, 402

Fitch, W. S.1970 ApJ 161, 669

Fouqué, P. & Gieren, W.P. 1997, A&A 320, 799

Freedman, W.L. 1988, ApJ 326, 691

Freedman, W.L. & Madore, B.F. 1990, ApJ 365, 186

Freedman, W.L., Madore, B.F., Gibson, B.K., et al. 2001, ApJ 553, 47

Fry, A.M. 1997, Thesis (PHD). University of North Carolina at Chapel Hill

Fry, A.M. & Carney, B.W. 1997, AJ 113, 1073 (FC97)

Fulbright, J.P. 2000, AJ, 120, 1841

Fuhr, J.R., Martin, G.A., Wiese, W.L. 1988, 'Atomic transition probabilities. Iron through Nickel', New York: American Institute of Physics

Fuhr, J.R., Martin, G.A., Wiese, W.L. 1988, 'Atomic transition probabilities. Scandium through Manganese', New York: American Institute of Physics (AIP) and American Chemical Society(AIP) and American Chemical Society

Gibson, B.K. 2000, MmSAI 71, 693

Gould, A. 1994, ApJ 426, 542

Bibliography

Gray, D.F. 1992, Book-Review: 'Observations and Analysis of Stellar Photospheres', Sci 257, 1978

Gray, D.F. 1994, PASP 106,1248

Grevesse, N. & Sauval, A.J. 1998, SSRv 85, 161

Groenewegen, M.A.T 2004, MNRAS 353, 903

Groenewegen, M.A.T., Romaniello, M., Primas, F. & Mottini, M. 2004, A&A 420, 655

Gustafsson, B., Bell, R.A., Eriksson, K., Nordlund, A. 1975, A&A 42, 407

Hertzsprung, E. 1926, BAN 3, 203

Hill, V. 1997, A&A 324, 435

Hill, V., Andrievsky, S.M. & Spite, M. 1995, A&A 293, 347

Hill, V. 1999, A&A 345, 430

Hill, V., Spite, M., Primas, F. et al. 2000, A&A 364, 19

Hoeppner, W., Kaehler, H., Roth, M. L., Weigert, A. 1978, A&A 63, 391

Holweger, H. 2001, AIPC 598, 23

Hoskin M. 1999, The Cambridge Concise History of Astronomy, Edited by Michael Hoskin, pp. 376. ISBN 0521572916. Cambridge, UK: Cambridge University Press, March 1999

Iben, I., Jr., Tuggle, R. S. 1975, ApJ 197, 39

Jaschek, C. & Jaschek, M. 1995, Books-Review: 'The Behavior of Chemical Elements in Stars', Sci 270, 1236

Jensen, J.B., Tonry, J.L., Barris, B.J. et al. 2003, ApJ 583, 712

Kaler, J.B. 1989, Book Review: 'Stars and their spectra', Ap&SS 162, 176

Kaufer, A., D'Odorico, S. & Kaper, L. 2004, UVES User Manual, Issue 1.9, VLT-MAN-ESO-13200-1825

Kennicutt, R.C., Stetson, P.B., Saha, A., et al. 1998, ApJ 498, 181

Kervella, P., Thvenin, F., Morel, P. 2003, A&A 408, 681

Kervella, P., Bersier, D., Mourard, D., et al. 2004, A&A 428, 587

King, D. S., Hansen, C. J., Ross, R. R. et al. 1975, ApJ 195, 467

Kiss, L.L. & Vinko, J. 2000, MNRAS 314, 420

Bibliography

Kochanek, C.S. 1997, ApJ 491, 13

Korn, A.J., Becker, S.R., Gummersbach, C.A. & Wolf, B. 2000, A&A 353, 655

Kovtyukh, V.V. & Gorlova, N.I. 2000, A&A 351, 597

Kovtyukh, V.V., Andrievsky, S.M, Belik, S.I. & Luck, R.E. 2005, AJ 129, 433

Kraft, R.P. 1961, ApJ 134, 616

Kupka, F., Piskunov, N.E., Ryabchikova, T.A., Stempels H.C. & Weiss W.W. 1999, A&AS 138, 119

Kurucz, R.L. 1970, SAOSR, 309

Kurucz, R.L. 1990,Proceedings of the 3rd International Collogium of the Royal Netherlands Academy of Arts and Sciences, Amsterdam, August 28-31, 1989, Amsterdam: North-Holland, 1990, edited by J. E. Hansen., p.20

Kurucz, R.L. 1993, CD-ROMS #1, 13, 18

Laney, C. D. 1991, IAUS 148, 109

Laney, C.D. & Stobie, R.S. 1992, A&AS 93, 93

Laney, C. D. & Stobie, R. S. 1993, MNRAS 263, 921

Laney, C. D.& Stobie, R. S. 1994, MNRAS 266, 441

Laney, C.D. & Stobie, R.S. 1995, MNRAS 274, 337

Leavitt, H.S., Pickering, E.C. 1912, HarCi. 173, 1

Lester, J.B., Lane, M.C., Kurucz, R. L. 1982, ApJ, 260, 272

Lodders, K. 2003, ApJ 591, 1220

Luck, R.E. & Andrievsky, S.M. 2004, AJ 128, 343

Luck, R.E. & Lambert, D.L. 1981, ApJ 245, 1018

Luck, R.E. & Lambert, D.L. 1985, ApJ 298, 872

Luck, R.E. & Lambert, D.L. 1992, ApJSS 79, 303 (LL92)

Luck, R.E., Moffet, T.J., Barnes, T.G. III & Gieren, W.P. 1998, AJ 115, 605 (L98)

Luck, R.E., Gieren, W.P., Andrievsky, S.M., et al. 2003, A&A 401, 939

Madore, B.F. 1977, MNRAS 178, 505

Bibliography

Madore, B.F., Freedman, W.L. 1991, PASP 103, 933

Marconi, M., Musella, I. & Fiorentino, G. 2005, ApJ 632, 590

Matteucci, F. 2003, The Chemical Evolution of the Galaxy. By Francesca Matteucci, Department of Astronomy, University of Trieste, Italy. Astrophysics and Space Science Library Volume 253 reprint Kluwer Academic Publishers, Dordrecht

McWilliam, A. 1997, ARA&A 35,503

Munari, U. 2000, Molecules in Space and in the Laboratory, Proceedings of a workshop held 2-5 June 1999 in Carloforte, Cagliari. Edited by I. Porceddu, and S. Aiello. Bologna, Italy, Italian Physical Society, Conference Proceedings, v. 67, 2000., p.179

Nordgren, T.E., Lane, B.F., Hindsley, R.B., Kervella, P. 2002, AJ 123, 3380

Orsatti, A. M., Vega, E.I., Marraco, H.G. 2001, A&A 380, 130

Pagel, B.E.J. 1998, A&G 39, 27

Pardo, I., Poretti, E. 1997, A&A 324, 121

Peacock, J.A. 1999, Cosmological Physics, pp. 704.,Cambridge University Press

Pel, J. W., Lub, J. 1978, IAUS 80, 229

Persson, S.E., Murphy, D.C., Krzeminski, W., Roth, M., Rieke, M. J. 1998, AJ 116, 2475

Persson, S.E., Madore, B.F., Krzeminski, W., et al. 2004, AJ, 128, 2239

Perryman, M. 1999, S&T 97, 40

Pietrinferni, A., Cassisi, S., Salaris, M., Castelli, F. 2004, ApJ 612, 168

Pont, F., Burki, G., Mayor, M. 1994, A&AS 105, 165

Pritchard, J.D. 2004, FEROS-II User Manual, Issue 1.4, LSO-MAN-ESO-22200-0001

Rolleston, W.R.J., Dufton, P.L., Fitzsimmons, A. et al. 1993, A&A 277, 10

Rolleston, W.R.J.,Trundle, C. & Dufton, P.L. 2002, A&A 396, 53

Romaniello, M., Salaris, M., Cassisi, S., Panagia, N. 2000, ApJ 530, 738

Romaniello, M., Primas, F., Mottini, M., Groenewegen, M.A.T., Bono, G. & François, P. 2005, A&A 429, L37 (Paper I)

Russell, S.C. & Bessell, M.S. 1989, ApJS 70, 865

Russell, S.C. & Dopita, M.A. 1992, ApJ 384, 508

Bibliography

Ryabchikova T.A. Piskunov N.E., Stempels H.C., Kupka F., Weiss W.W. 1999, proc. of the 6th International Colloquium on Atomic Spectra and Oscillator Strengths, Victoria BC, Canada, 1998, Physica Scripta T83, 162

Sakai, S., Ferrarese, L., Kennicutt, R.C. & Saha, A. 2004, ApJ 608, 42

Sandage, A., 1958, ApJ 127, 513

Sandage, A., Tammann, G.A. 1969, ApJ 157, 683

Sandage, A. 1999, ApJ 128, 150

Sandage, A., Bell, R.A. & Tripicco, M.J. 1999, ApJ 522, 250

Sasselov, D.D., Beaulieu, J.P., Renault, C., et al. 1997, A&A 324, 471

Schlesinger, B. M. 1977, ApJ 212, 507

Shapley, H. 1914, ApJ 40, 448

Shapley, H. 1918, ApJ 48, 279

Sneden, C. 1973, ApJ 184, 839

Sneden, C. 2004, MmSAI 75, 267

Storm, J., Carney, B.W., Gieren, W.P., Fouqué, P., Latham, D.W. & Fry, A.M. 2004, A&A 415, 531

Szabados, L. 1995, ASPC 83, 357

Szabados, L. 2003, Inf. Bull. Var. Stars, No. 5394

Takeda, Y. 2003, A&A, 402, 343

Tammann, G.A., Sandage, A., Reindl, B. 2003, A&A 404, 423

Tinsley, B.M. 1979, IAUS, 84, 431

Udalski, A., Soszynski, I., Szymanski, M. et al. 1999a, AcA 49, 45

Udalski, A., Soszynski, I., Szymanski, M. et al. 1999b, AcA 49, 1

Udalski, A., Wyrzykowski, L., Pietrynski, G., et al. 2001, Acta Astron. 51, 221

Walker, A.R., Raimondo, G., Di Carlo, E. 2001, ApJ 560, 139

Walker, A.R. 2003, in: Stellar candles for the extragalactic distance scale, Lect. Notes Phys. 635, 265

Westerlund, B.E. 1997, in: The Magellanic Clouds, Cambridge Astrophysics Series 29

Zhevakin, S. A., 1963, ARA&A 1, 367

Acknowledgements

I would like to thank my supervisors Drs. Francesca Primas and Martino Romaniello for their advice, guidance, patience and support during these years of work together. Many thanks goes to Dr. Giuseppe Bono for being an inexaustable mine of suggestions about useful articles and for our long discussions. I would like to thank my official advisor Dr. Achim Weiss for his advice and suggestions that helped to improve this thesis.
Thanks also goes to Dr. Patrick François, for let me use his software to measure the equivalent widths, and to all the people at ESO for making it a very stimulating scientific enviroment.
A very special thanks goes to my friends: Paola Popesso, Mara Salvato, Marcella Brusa, Alessandra Contursi, Lorenza e Piero Rosati, Alessandro Rettura, Fabio Sogni, Vincenzo e Sandra Mainieri, Arne Rau, Silvia Vicente, Stephane Blondin and Vicky Alonso, for sharing the good and the bad moments of these years and for being great company.
Finally I would like to thank my Family, whose love and support made this all possible.